



INAOE

The Gravoturbulent Interplay between Star Cluster Feedback and Sequential Star Formation in NGC 1569-A

by

Jesús Omar Hernández Prado

Thesis submitted in partial fulfillment of the
requirements for the degree of

MASTER OF SCIENCE IN ASTROPHYSICS

at the

**Instituto Nacional de Astrofísica, Óptica y
Electrónica**

July 2023

Tonantzintla, Puebla

Advised by:

PhD. Sergio Martínez González

Tenured Researcher - INAOE

PhD. Yalia Divakara Mayya

Tenured Researcher - INAOE

©INAOE 2023

The author hereby grants to INAOE permission to
reproduce and to distribute publicly paper and
electronic copies of this thesis document in whole or
in part



Abstract

Super star clusters dominate the dynamics and evolution in the central region of the galaxy NGC 1569. Recent studies have determined different ages and complex morphology within the clusters, allowing to create complicated structures of gas related with superbubbles, HII regions and the gas leftover from star formation. Using 3-D hydrodynamic techniques, I have studied the formation of a second star cluster very near to an existing massive star cluster in NGC 1569. The two star clusters are separated by a mere 3 pc in projection and have an age difference of only 3 Myr. This study provides insights into the viability of the second cluster's formation in a challenging environment influenced by the feedback from the first star cluster.

Resumen

La dinámica y la evolución en la región central de la galaxia NGC 1569 está dominada por la presencia de algunos supercúmulos estelares. Estudios recientes han determinado diferentes edades y una morfología compleja dentro de los cúmulos, lo que permite crear estructuras complicadas de gas relacionadas con superburbujas, regiones HII y el gas remanente de la formación estelar. Utilizando técnicas hidrodinámicas en 3-D, he estudiado la formación de un cúmulo estelar muy cerca de un cúmulo estelar masivo existente en NGC 1569. Los dos cúmulos estelares están separados por sólo 3 pc en proyección y tienen una diferencia de edad de sólo 3 millones de años. Este estudio proporciona información sobre las condiciones de viabilidad para la formación del segundo cúmulo estelar en un entorno desafiante influenciado por la retroalimentación del primer cúmulo estelar.

Acknowledgment

First and foremost, I would like to express my gratitude to my thesis advisor, Dr. Sergio, for providing unwavering support, invaluable knowledge, and infinite patience. His guidance has been instrumental, not only in offering a broad spectrum of decision-making within the project but also in maintaining a clear research trajectory. My co-advisor, Dr. Divakara, deserves special acknowledgment for his substantial contributions in enhancing the quality of this work, as well as his steadfast support and insightful guidance.

My heartfelt thanks go to my family, whose contributions to my development, both intellectually and personally, have spanned from my earliest years. To Mariana, your endurance, encouragement, and unwavering love throughout this entire process have been my bedrock.

The authors thankfully acknowledge the computer resources, technical expertise and support provided by the Laboratorio Nacional de Supercómputo del Sureste de México (LNS), CONACYT member of the network of national laboratories.

Dedictory

Dedicated to the enduring memory of my beloved grandparents, María and Zotero, whose wisdom and love continue to inspire me.

This dedication is extended to my beloved family: Ana María, Margarita, Mariana, Raymundo, Lola, and Almendra. Their presence infuses my journey with depth and warmth, illuminating the path forward with shared love and cherished bonds.

Contents

Abstract	i
Resumen	iii
Dedicatory	vii
1 Introduction	1
1.1 Star cluster	3
1.2 Stellar Winds	5
1.2.1 Historical background	5
1.2.2 Description	5
1.2.3 Theory	6
1.3 NGC 1569	12
1.3.1 Super star cluster A	15
2 Theory	19
2.1 Fluid Dynamics	19
2.1.1 Mass conservation	19
2.1.2 Momentum conservation	20
2.1.3 Energy conservation	20
2.1.4 Source Terms and Cooling Mechanisms	21
2.2 Star Cluster Formation	22
2.3 Shock Waves	24
2.3.1 Rankine-Hugoniot Jump Conditions	25

2.4	Collision between Stellar Winds and the Interstellar Medium	26
2.4.1	Structure of Wind-driven Bubbles	27
2.4.2	Star Cluster Driven Wind Theory	29
2.5	Gas expulsion during the early evolution of young star clusters	38
3	FLASH Simulation	49
3.1	CLOUDS Module Setup	50
3.1.1	Turbulence	50
3.2	COOL Module	51
3.3	CINDER Module	51
3.4	WIND Module	53
3.5	SINKS Module	54
3.6	GRAVITY Module	55
4	Simulation analysis	57
4.1	Clouds Setup	57
4.1.1	Clumpy-case	59
4.1.2	Cloud-Cloud case	63
4.2	Evolution of the Clumpy-Case	68
4.3	Evolution of the Cloud-Cloud Case	84
5	Discussion and Conclusions	95
	List of Figures	99
	List of Tables	105
	References	107

Chapter 1

Introduction

A **star cluster** is a cohesive group of stars bound together by mutual gravitational attraction. These clusters typically contain at least a dozen of stars and are located within confined, non-dark matter-dominated regions (Portegies Zwart et al., 2010). By studying star clusters, researchers can gain valuable insights into the processes of star formation and evolution.

The activity and evolution of individual stars within a cluster can have a significant impact on the cluster as a whole and the surrounding interstellar medium. This interaction plays a critical role in the overall structure and composition of the galaxy in which the cluster resides. Figure 1.1 illustrates this phenomenon, showing NGC 346, an open cluster located in the Small Magellanic Cloud, where feedback from hot stars is creating an irregular arch-like structure of gas and dust around the cluster.

The formation and evolution of star clusters in a host galaxy can significantly alter the morphological, dynamical, and chemical properties of the surrounding region, making the study of these objects crucial.



Figure 1.1: Open cluster NGC 346 is captured in this composite image, which combines separate exposures taken by the James Webb Telescope using the NIRCams instrument. The colors in the image result from different filters: red represents the F444W filter, orange represents the F335M filter, cyan represents the F277W filter, and blue represents the F200W filter. Credit: NASA, ESA, CSA, Olivia C. Jones (UK ATC), Guido De Marchi (ESTEC), Margaret Meixner (USRA)

1.1 Star cluster

The formation of a star following the collapse of a molecular cloud is not an isolated event but rather a collective process, giving rise to the formation of star clusters, as discussed in Chapter 2.2.

The collective nature of star formation might lead one to assume that all stars within a given cluster are a single stellar population, having the same age and chemical abundances. However, with the advent of precision instruments such as the *Hubble Space Telescope*, we have gained a deeper understanding of the oldest clusters, i.e. the globular clusters, revealing the complexity of their stellar populations through color-magnitude diagrams, which exhibit chemical anomalies, indicating significant variations in abundances among stars within the clusters, a phenomenon referred to as "multiple populations" (Bastian & Lardo, 2018). The classical classification of star clusters results in two distinct categories based on their mass, size, and age. As mentioned earlier, one category is the globular clusters (see Figure 1.2), characterized by their advanced age ($t > 10^7$ yr), substantial mass ($M \sim 10^4 M_\odot - 10^6 M_\odot$), and compact nature ($r_{hl} \sim 3$ pc, where r_{hl} represents the radius that contains half of the integrated light emitted by the cluster) (Gratton et al., 2019). These clusters exhibit spherical shapes, high density, and represent some of the oldest objects in the Universe (Harris, 1996). The other category comprises the open clusters (see Figure 1.2), which possess contrasting properties compared to globular clusters. Open clusters are relatively young ($t < 10^6$ yr), less massive ($M \sim 10 M_\odot - 10^3 M_\odot$), and more extended ($r_{hl} \sim 10$ pc). They exhibit an asymmetrical structure and lower density, making them more prone to disruption due to gravitational forces exerted by the host galaxy (Kharchenko et al., 2005).

Star clusters provide a unique laboratory for the study of stellar formation and evolution, due to their measurable properties such as metallicity, age, and the presence or absence of multiple stellar populations (Milone & Marino, 2022). Yet, the question remains: how did the oldest clusters evolve to their present stage? Super Star Clusters (SSCs) may hold the answer. With masses ranging from 10^4 to $10^6 M_\odot$, radii of approximately 1 pc, and densities of $10^4 M_\odot \text{ pc}^{-3}$, SSCs are comparable to globular clusters, but contain very young stars, sometimes even as young as a few million

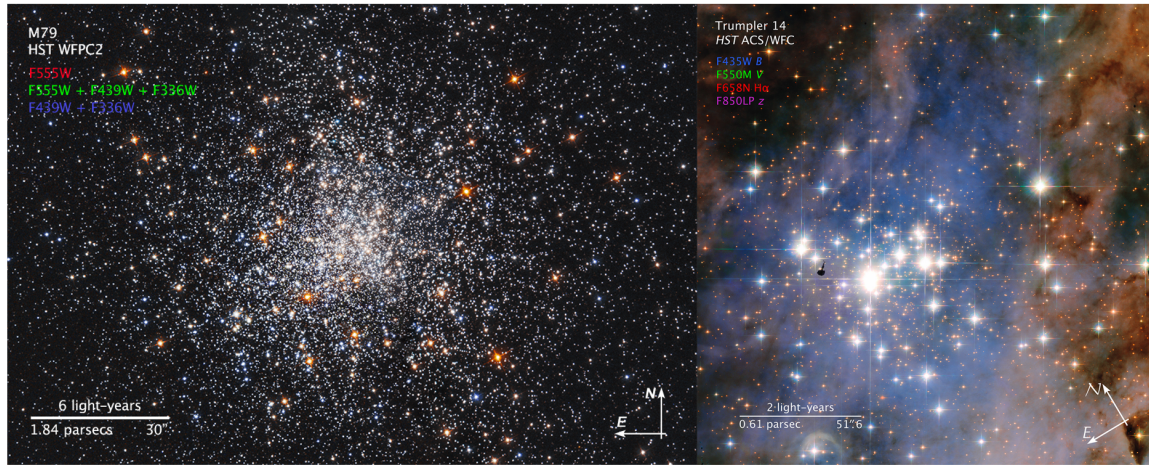


Figure 1.2: On the left side, we have the globular cluster M79 captured in a composite image created from various exposures using the WFPC2 instrument on the Hubble Space Telescope. The colors in the image result from different filters: blue corresponds to the F336 + F439 filters, green corresponds to the F336 + F439 + F555 filters, and red corresponds to the F555 filter. Credit: NASA and ESA. On the right side, we have the open cluster Trumpler 14, captured in a composite image made from multiple exposures using the ACS/WFC instrument on the Hubble Space Telescope. The colors in the image are the result of different filters: blue corresponds to the F435W (B) filter, green corresponds to the F550M (V) filter, red corresponds to the F658N (H_{α} + $[N\ II]$) filter, and purple corresponds to the F850LP (SDSS z) filter. Credit: NASA, ESA, and Z. Levay (STScI).

years. SSCs are typically found in starburst regions or galaxy mergers (Mayya et al., 2008; Melo et al., 2005), making them powerful tools for understanding the processes of stellar formation and evolution.

Inside a star cluster, millions of stars are concentrated within a compact region. The evolution of the cluster is predominantly influenced by the massive stars, which have a short lifespan before undergoing supernova explosions. Additionally, the evolution of the interstellar medium (ISM) in the host galaxy is dependent on various factors such as mass, gas density, injected energy, and the positions of the star cluster. This interaction between the cluster and the ISM gives rise to several distinct structures. Superbubbles are formed within the galactic disk, while ring-like structures known as supershells can also emerge. Furthermore, galactic winds contribute to the formation of filamentary structures extending beyond the boundaries of the galactic disk

(Sánchez-Cruces et al., 2015).

1.2 Stellar Winds

1.2.1 Historical background

Eugene Parker (1958; 1960) was the first to use the terms *solar wind* and *stellar winds*. However, earlier discoveries provided evidence for the existence of stars with broad emission line spectra, such as novae. In 1572, Tycho Brahe discovered a new star, which was later identified as a supernova. In 1600, Blaeu discovered a new star that is now known as *P Cygni*, which is classified as a luminous blue variable star. The P-Cygni profile played an important role in the development of the theory of stellar winds. Later, Wolf & Rayet (1867) discovered a new class of stars with spectral lines similar to those in novae and P-Cygni, but without any outbursts or fading over time. These stars were named **Wolf-Rayet** stars. In 1929, Beals propose a **continuous outflow** happening in the Wolf-Rayet stars, due to the similarity in the profiles with the P-Cygni of novae, five years later Chandrasekhar proposed that the explanation to the P-Cygni is an expanding atmosphere of the star.

1.2.2 Description

Due to the energy released via nuclear reactions, line-driven winds occur when the opacity of the atmosphere allows certain spectral lines to trap and transfer momentum. In such a scenario, the radiation exerts pressure on the gas, propelling it outward in the form of a **stellar wind**.

Stellar winds can vary in strength and velocity depending on the type and age of the progenitor star. For example, young and massive stars produce stronger winds (massive O stars). Additionally, some stars, such as red giants and supergiants, can experience periodic outbursts of mass loss in the form of powerful stellar winds. By the time the progenitor star explodes as a supernova, around half of its initial mass has already been stripped away in the form of a stellar wind (Lamers & Cassinelli, 1999). The massive star's stellar wind compresses the surrounding ambient gas, creating a thin, rapidly cooling, and expanding shell. As a result, the medium around the massive

star forms a structured pattern from the center outwards, consisting of a free-wind region, a shocked-wind region separated from the shell by a contact discontinuity (see section 2.3).

1.2.3 Theory

The two main properties of a stellar wind that are derived from observations are the **mass loss rate** (\dot{M}), which represents the amount of mass that the star loses per unit of time, and the **terminal velocity** v_∞ , which refers to the velocity of the stellar wind at a significant distance from the star.

The stellar wind injects energy into the surrounding medium at a rate $\frac{1}{2}\dot{M}v_\infty^2$. For example, for a star with a spherically symmetric wind, the mass loss rate is defined as:

$$\dot{M} = 4\pi r^2 \rho(r) v(r) \quad (1.2.1)$$

The stellar wind velocity is usually parametrized by:

$$v(r) \simeq v_0 + (v_\infty - v_0) \left(1 - \frac{R_*}{r}\right)^\beta \quad (1.2.2)$$

where R_* is the photosphere radius, v_0 is the central wind velocity and β is the velocity law exponent, which determines how quickly the velocity decreases with distance from the star, in the case of hot stars $\beta = 0.8$ and higher for cooler stars (Lamers & Cassinelli, 1999).

The spectral lines of the wind are distinguishable from photospheric lines due to their significant width or wavelength shift caused by the outflowing motion of gas in the wind. These spectral lines can appear in different forms, such as absorption, emission, or a combination of both, which depends on the efficiency of creating or destroying line photons in the stellar wind.

The theory of radiation-driven winds states that the absorption of radiation in lines occurs when specific photon wavelengths are absorbed by atoms and ions in the star's outer layers. This leads to the transfer of momentum to gas particles, thus driving the stellar wind.

OB stars, which are known for their high temperatures and luminosities, experience powerful radiation pressure that exceeds gravitational forces, resulting in the driving of their winds. In a study by Lamers & Cassinelli (1999), the mass loss rates of O stars in the Large Magellanic Cloud (LMC) and Small Magellanic Cloud (SMC) were compared with those of stars in the Galaxy, finding that the difference in mass loss rates is influenced not only by metallicity but also by the stellar luminosity.

Markova (2004; 2008) estimated mass loss rates and terminal velocities for O-type and B supergiant stars, observing ranges from $10^{-6.5}$ to $10^{-5} M_{\odot} \text{ yr}^{-1}$ and from 1500 to 2500 km s^{-1} , respectively.

Martínez-González et al. (2019a), modeled an isotropic stellar wind using the stellar evolutionary models of Schaller et al. (1992a), and a modified version of a time-dependent wind source by Wünsch et al. (2008b), where the wind mass flux is (see Fig.1.3):

$$\dot{M}(r) = \dot{M}_w r / R_v \quad (1.2.3)$$

where \dot{M}_w is the time-dependent mass loss rate and R_v the radius of the sphere where the wind is injected. Additionally, the mass density and velocity are calculated at each timestep with:

$$\rho(r) = \frac{\dot{M}_w}{4\pi v_{\infty} r^2} \quad \wedge \quad v(r) = \frac{v_{\infty} r}{R_v} \quad (1.2.4)$$

In cool stars, the winds are molecular and dusty, with low outflow velocities $\sim 15 - 30 \text{ km s}^{-1}$ and mass loss rates from $10^{-7} M_{\odot} \text{ yr}^{-1}$ for M giants stars and $\sim 10^{-4} M_{\odot} \text{ yr}^{-1}$ for AGB stars (Draine, 2011).

1.2.3.1 Isothermal winds

Here I consider the case of an isothermal wind where the gas is subject to only two forces: inward gravity and outward-directed pressure gradient of the gas. From the infinite number of solutions to the hydrodynamic equations, only one is known as the critical wind solution, where the flow starts subsonic and ends up supersonic.

In a time-independent stellar wind with a constant mass loss rate, the outflow of gas with velocity $v(r)$ passing through a sphere of radius r and density $\rho(r)$ remains

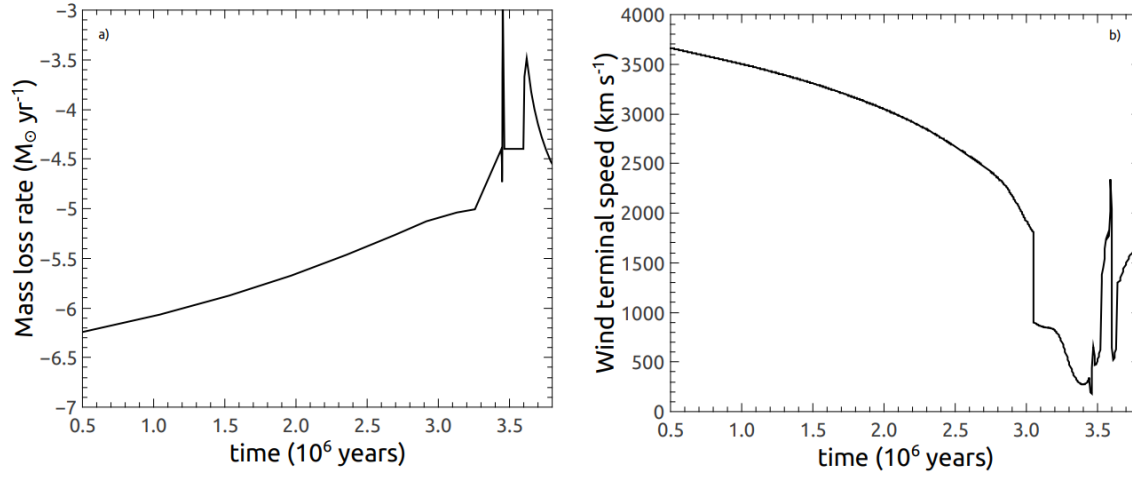


Figure 1.3: Evolution of a $60M_{\odot}$ star, panel (a) shows the mass loss rate with solar metallicity obtained by Schaller et al. (1992b) and panel (b) shows the terminal speed assuming a conversion factor between v_{∞} and v_{esc} introduced by Vink et al. (2001). Adapted from Martínez-González et al. (2019b).

constant. This relationship can be expressed by the equation of mass conservation:

$$\dot{M} = 4\pi r^2 \rho(r) v(r) \quad (1.2.5)$$

While the motion of gas in a stellar wind can be described by $f = \rho \frac{dv}{dt}$, when considering a stationary scenario and only accounting for the previously mentioned forces, the motion is instead governed by the equation:

$$\underbrace{v \frac{dv}{dr}}_{\text{acceleration}} + \underbrace{\frac{1}{\rho} \frac{dp}{dr}}_{\text{pressure gradient}} + \underbrace{\frac{GM_*}{r^2}}_{\text{gravity}} = 0 \quad (1.2.6)$$

where G is the gravitational constant and M_* the star mass.

Assuming that the wind temperature is kept at a constant value and that the gas behaves as an ideal gas, the thermal pressure is defined as:

$$p = \frac{\rho k_B T}{\mu} \quad (1.2.7)$$

where, k_B is the Boltzmann constant and μ the mean atomic weight of the particles.

The force due to the pressure gradient for an isothermal wind:

$$\frac{1}{\rho} \frac{dp}{dr} = k_B \mu \frac{dT}{dr} + \frac{k_B T}{\mu \rho} \frac{d\rho}{dr} = \left(\frac{k_B T}{\mu} \right) \frac{1}{\rho} \frac{d\rho}{dr} \quad (1.2.8)$$

The density gradient can be expressed in a velocity gradient by:

$$\frac{1}{\rho} \frac{d\rho}{dr} = -\frac{1}{v} \frac{dv}{dr} - \frac{2}{r} \quad (1.2.9)$$

$$\frac{1}{v} \frac{dv}{dr} = \frac{\frac{2a^2}{r} - \frac{GM_*}{r^2}}{v^2 - a^2}, \text{ with } a = \sqrt{\frac{k_B T}{\mu}} = \text{constant} \quad (1.2.10)$$

As can be observed, equation 1.2.10 contains two singularities, the terms r^{-1} and r^{-2} . This occurs when the distance r is equal to the critical distance r_c , defined as:

$$r = r_c \equiv \frac{GM_*}{2a^2} \quad (1.2.11)$$

The critical distance is also known as the distance of the **critical point**. For the isothermal wind solution to be valid, it must satisfy the condition $r_c > r_0$, where r_0 is the photospheric radius. If $r_c < r_0$, the solution would not be within the isothermal region. The only solution that passes through the critical point and maintains a positive velocity gradient at all distances is referred to as the **critical solution** for which:

$$v(r_c) = a = \frac{v_{\text{esc}}(r_c)}{2} \quad (1.2.12)$$

where $v_{\text{esc}} = \sqrt{\frac{2GM_*}{r_c}}$ is the escape velocity at the critical point, and the point where $v(r) = a$ is the **sonic point** and $v(r_c) = v_{\text{esc}}(r)$ is the **escape point**.

One of the important features of the isothermal wind model is the existence of a critical point, where the velocity of the gas reaches the sound speed. The critical point is the point at which the gas transitions from subsonic to supersonic flow. The critical point plays an important role in the dynamics of the wind, and it determines the mass loss rate of the star.

The critical solution occurs for the value of velocity at the lower boundary, denoted as $v_0(\text{crit})$. This implies that a given density ρ_0 at the bottom can only generate a transonic wind if the equation

$$\dot{M} = 4\pi r_0^2 \rho_0 v_0(\text{crit}) \quad (1.2.13)$$

holds, leading to a specific value of the mass loss rate with given lower boundaries of density, temperature, and gravity.

Consider the total energy as:

$$E(r) = \underbrace{\frac{v^2}{2}}_{\text{kinetic energy}} - \underbrace{\frac{GM_*}{r}}_{\text{potential energy}} + \underbrace{\frac{5}{2} \frac{k_B T}{\mu}}_{\text{enthalpy}} \quad (1.2.14)$$

where the enthalpy term is the sum of the internal energy $\frac{3}{2} \frac{k_B T}{\mu}$ and the work required for adiabatic expansion $\frac{k_B T}{\mu}$.

Take into account that in the **critical point** the total energy is equal to zero. Rearranging the equation of energy as:

$$E(r) = E(r_0) + \frac{v^2 - v_0^2}{2} + \frac{GM_*}{r_0} \left(1 - \frac{r_0}{r}\right) \quad (1.2.15)$$

It can be shown that the energy of an isothermal wind is not constant, and in winds where the primary heating and cooling mechanisms are radiative processes, the wind can closely approach an isothermal state.

To derive the velocity law of the wind, consider the momentum equation 1.2.10 and its analytical solution with the constant fixed with the condition $v(r_c) = a$ at the critical point:

$$v \exp\left(-\frac{v^2}{2a^2}\right) = a \left(\frac{r_c}{r}\right)^2 \exp\left(-\frac{2r_c}{r} + \frac{3}{2}\right) \quad (1.2.16)$$

The initial velocity can be found by applying the previous equation at the lower boundary of the isothermal region r_0 where $v_0 \ll a < v_{\text{esc}}$:

$$v_0 = a \left(\frac{v_{\text{esc}}(r_0)}{2a} \right)^2 \exp \left(-\frac{v_{\text{esc}}^2(r_0)}{2a^2} + \frac{3}{2} \right) \quad (1.2.17)$$

An isothermal wind driven by gas pressure can become supersonic with a specified value at the initial velocity. At larger distances $r \gg r_0$, the velocity laws follows:

$$v(r \rightarrow \infty) \simeq 2a \sqrt{\ln \left(\frac{r}{r_0} \right)} \quad (1.2.18)$$

increasing to infinity.

The density structure is derived by the mass continuity equation as:

$$\frac{\rho}{\rho_0} \exp \left(\frac{1}{2} \left(\frac{v_0 \rho_0 r_0^2}{a \rho r^2} \right)^2 \right) = \exp \left(-\frac{GM_*}{a^2} \left(\frac{1}{r_0} - \frac{1}{r} \right) \right) \quad (1.2.19)$$

The mass loss rate for a isothermal wind at the critical point is:

$$\dot{M} = 4\pi \rho_0 a r_0^2 \left(\frac{v_{\text{esc}}(r_0)}{2a} \right)^2 \exp \left(-\frac{v_{\text{esc}}^2(r_0)}{2a^2} + \frac{3}{2} \right) \quad (1.2.20)$$

The velocity together with the density ρ_0 at r_0 sets the mass loss rate of the star.

There are various solutions to the equation that govern the velocity of isothermal winds depending on the initial conditions at the wind's base. However, there is a unique critical solution in which the velocity of the wind changes from subsonic to supersonic. The total energy in the isothermal wind increases from negative at its base to positive in the supersonic region, which means that energy needs to be supplied to maintain the flow's isothermal nature. This energy is transformed into the kinetic energy of the wind via gas pressure.

Overall, the isothermal wind model provides a useful framework for studying the dynamics of stellar winds, particularly for hot, massive stars where the assumption of constant temperature is more likely to be valid.

On the other hand, non-isothermal winds refer to the outflows of gas or plasma where

the temperature of the wind varies significantly. In contrast to isothermal winds, where the temperature remains relatively constant throughout the flow. In non-isothermal winds, the temperature of the ejected material can change due to various factors, such as heating or cooling processes along the wind's path. These temperature variations can be influenced by factors like radiative cooling, shock heating, or energy injection from the central source. As a result, the wind's thermal energy content can vary at different spatial locations.

The presence of temperature variations in non-isothermal winds has significant implications for the overall structure, mass-loss rates, and energy budget of the outflows. These variations can affect the wind's velocity profile, density distribution, and overall energetics. Additionally, the thermal properties of non-isothermal winds can impact their interaction with the surrounding medium, leading to the formation of shocks, the creation of hot bubbles, or the triggering of further star formation episodes.

As we delve further, we will discover the paramount significance of the critical solution and, consequently, the **sonic point**, which carries various implications for the modeling of collective winds.

1.3 NGC 1569

NGC 1569 (see Fig. 1.4) is an irregular dwarf galaxy, Magellanic-type, located at a distance of 3.06 ± 0.18 Mpc (Grocholski et al., 2012). It is a member of the IC 342/Maffei group of galaxies in the constellation of Camelopardalis.

This galaxy contains at least 47 identified clusters that can be resolved, with a range of ages from 2 – 3 Myrs to 1 Gyr (Hunter et al., 2000). The most prominent ones are NGC 1569-A and NGC 1569-B (see Fig. 1.5), both of which are **super star clusters**. Starburst phase has happened 10-20 Myr ago (Hunter et al., 2000), since then, the formation of star clusters and their own evolution tracers such as supernovae explosions have taken place (Anders et al., 2004), the latter has injected energy into the ISM driving a bipolar superwind detected in emission of H α and X-ray (Heckman et al., 1995).

Sánchez-Cruces et al. (2015) detected and confirmed 12 superbubbles, 4 supershells

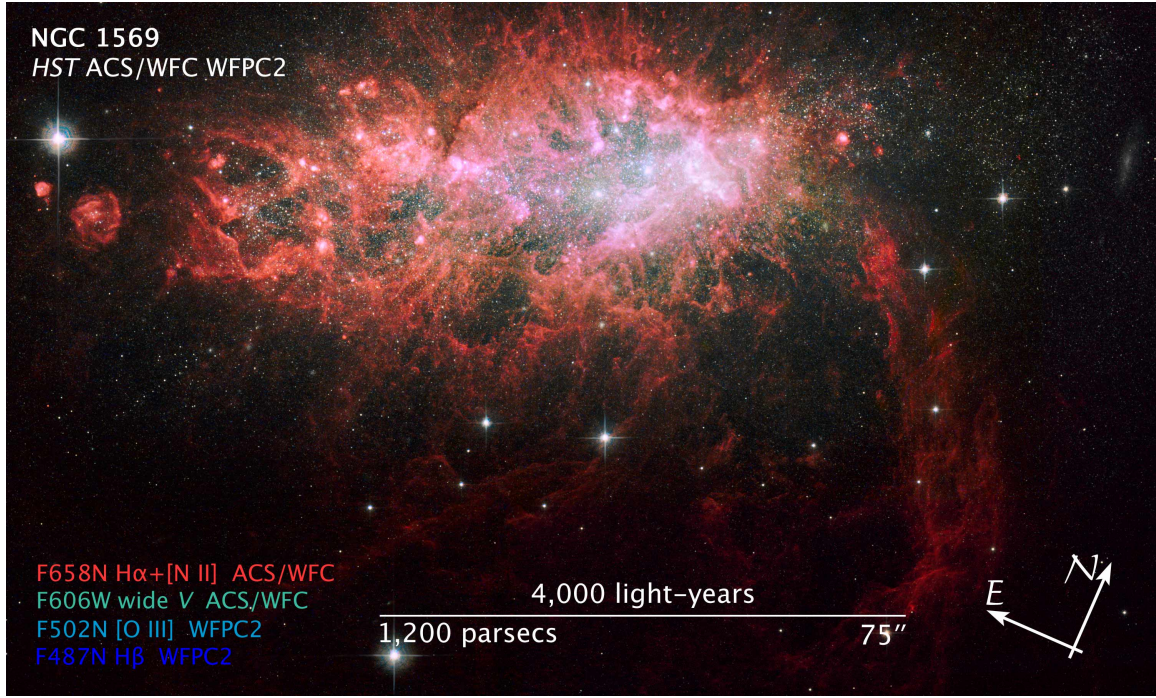


Figure 1.4: The galaxy NGC 1569 is captured in a composite image created from multiple exposures using the ACS and WFPC2 instruments on the Hubble Space Telescope. The image is produced using different filters: red corresponds to the F658N filter, which captures the $H_{\alpha} + [\text{N II}]$ emission; green/cyan corresponds to the F606W filter, representing the wide V band; cyan corresponds to the F502N filter, capturing the $[\text{O III}]$ emission; and blue corresponds to the F487 filter, capturing the H_{β} emission. In the image, we can observe the core of NGC 1569, which contains three giant star clusters. These clusters are situated within a central cavity that has been shaped by the feedback from massive young stars, resulting in distinct gaseous structures. Credits for the image go to NASA, ESA, and Z. Levay (STScI) for the illustration, and to NASA, ESA, the Hubble Heritage Team (STScI/AURA), and A. Aloisi (STScI/ESA) for the scientific data

and 15 filaments in NGC 1569. The expansion velocity of the superbubbles are from 23 km s^{-1} to 48 km s^{-1} and comparing with the escape velocity of the galaxy $V_{\text{exp}} < 70 \text{ km s}^{-1}$, the gas is gravitationally bound, nevertheless, it is not possible to know whether any supershell is bound or not, since their range of expansion velocity is from 70 km s^{-1} to 105 km s^{-1} . The dynamical ages of the superbubbles are from 0.5 to 1.8 Myr, their temperature is intermediate between a hot component such as superwind and a cold component, some of them having X-ray emission in their interior, though

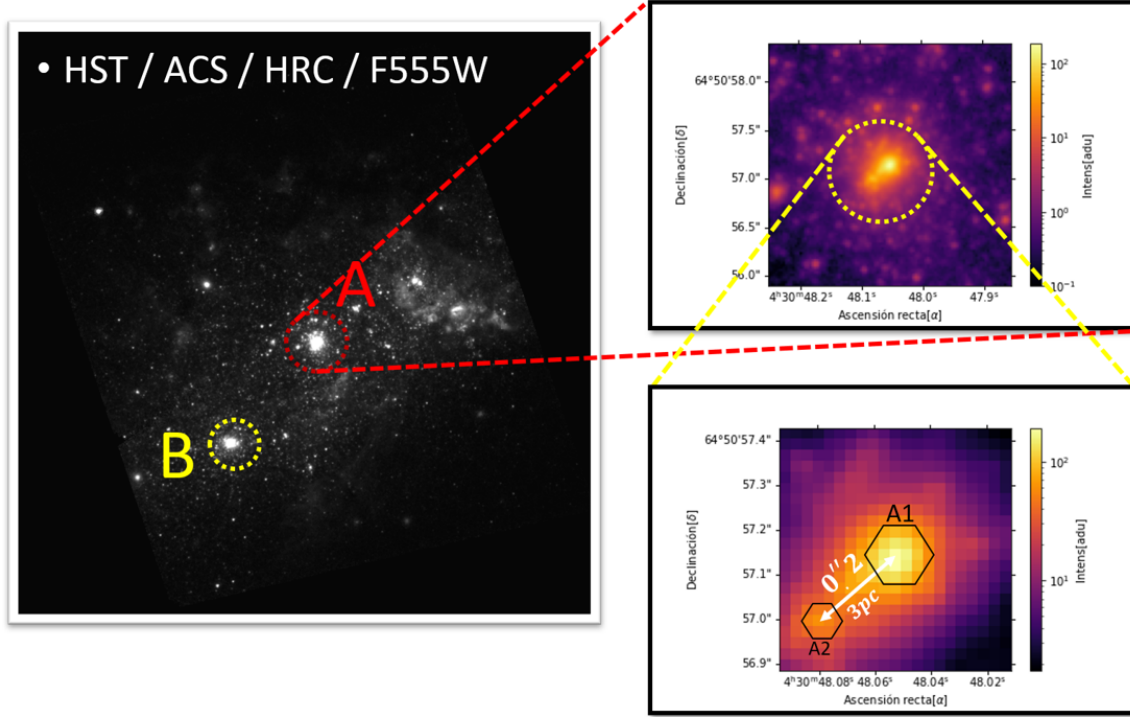


Figure 1.5: NGC 1569 (HST), both circles correspond to the super star clusters A and B (left). Close up for the SSC-A (right). Adapted from Hernández Prado (2022).

it is minimal and probably produced by contaminated superwind. In fact, it is unclear if the super galactic wind of NGC 1569 is extreme due to the coexisting superbubbles and galactic winds.

X-ray emission from within superbubbles sb 2, sb 3, and sb 4 (see Fig. 1.6) is minimal and likely caused due to contamination from superwind. By comparing the emission spectra of the superbubbles and two regions corresponding to the superwind, it can be fitted with a hot and cold component, $kT_1 = 0.71$ keV and $kT_2 = 0.17$ keV, respectively, indicating that the hot component is related to the emission of the superwind and the cold component to the halo. Meanwhile, the X-ray emission in the interior of sb 3 is attributed to processes within the superbubble itself (Sánchez-Cruces et al., 2015).

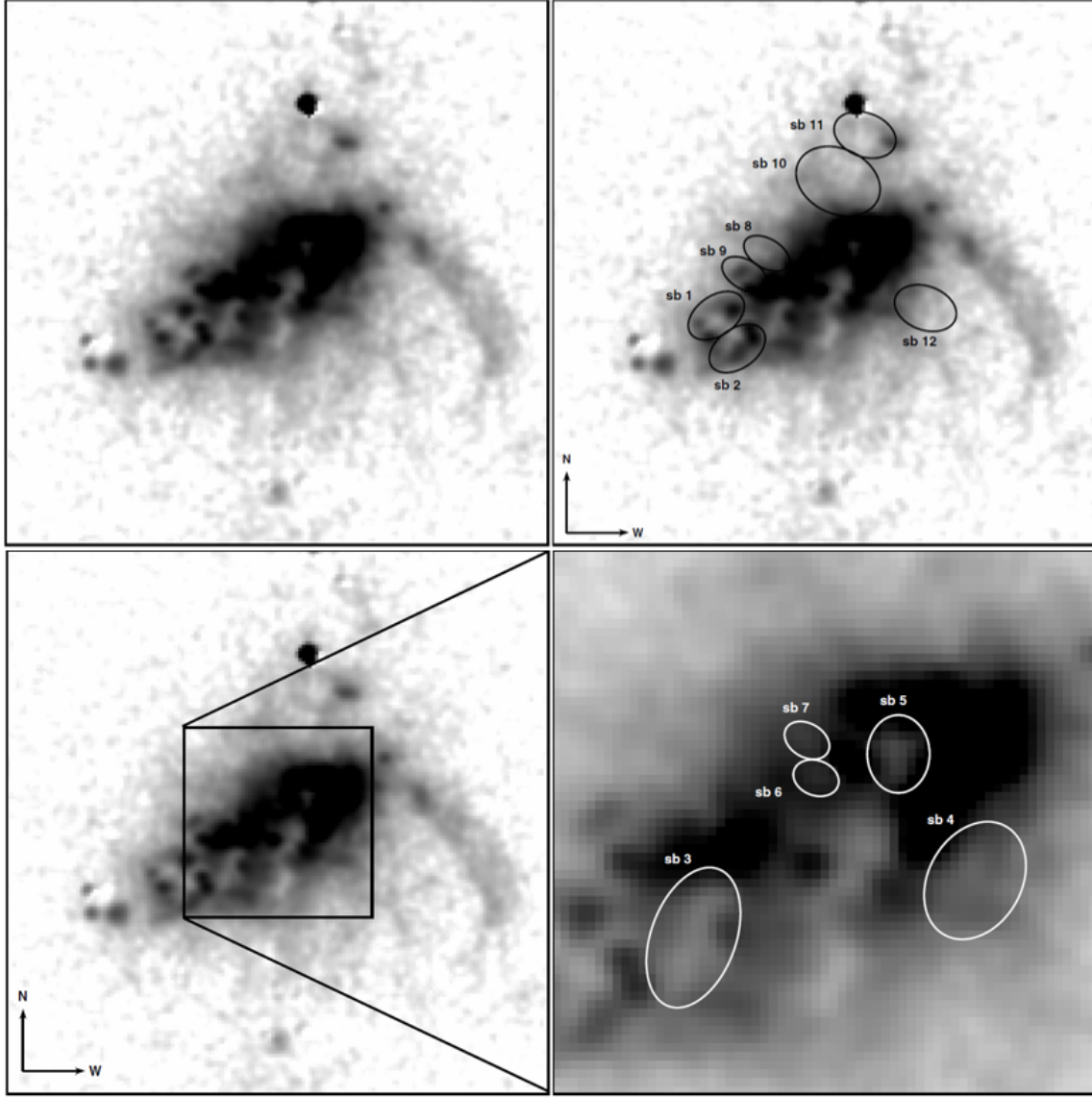


Figure 1.6: Velocity map in $H\alpha$ showing the superbubbles from the work of Sánchez-Cruces et al. (2015).

1.3.1 Super star cluster A

One of the crucial characteristics of this **starburst** galaxy is the **multiple populations** of stars within the SSCs. Populations of Wolf-Rayet stars (124 ± 11 reported (Mayya et al., 2020)) and red super giants have been proposed for the SSC-A, for

which their ages are 3 Myr and 9 Myr, respectively (González Delgado et al., 1997), and a mass of $5.5 \times 10^5 M_{\odot}$ (Mayya et al., 2020).

The thesis conducted by Álvarez Cruz (2022) demonstrates a remarkable agreement with the previous age determinations. The study involved a spectroscopic analysis utilizing MEGARA data, which is an instrument installed on the Gran Telescopio Canarias. Their analysis involved fitting a simple stellar population (SSP) model to the observed data, allowing for variation in age. This analysis revealed the presence of two populations with ages of 7 Myr and 4 Myr in the LR-B band.

Using photometry and spectroscopy studies, there is also an evidence of O-type stars besides the red super giants and Wolf-Rayet. The older population is dominated by a clear evidence for at least two populations, the younger one dominated by the O+WR stars and the older one traced by the RSGs (Origlia et al., 2001).

In the case of the SSC-A, De Marchi et al. (1997) showed that the morphology inside the cluster it is composed by a relatively fainter object located at $\sim 0.2''$ from the center of the SSC-A (see Fig. 1.5), called A1 and A2, according to the above, it is reported that the distance between the two objects, the center and the attached object is of 2.2 pc. Nevertheless, with a better estimation of the distance to NGC 1569 proposed by Grocholski et al. (2012), leads to improve this measurement. Recent studies show that this distance is 3 pc and the tidal radius for each structure prove that this system it is in gravitational interaction (Hernández Prado, 2022). Also it is important to place the populations in each component: the younger within A2 and the older in A1 (Origlia et al., 2001).

As the cluster relaxation process has not yet occurred naturally (Hernández Prado, 2022), surface brightness profile models generated with nProfit (Cuevas-Otahola et al., 2022) indicate that in order to accurately reproduce the profile of SSC-A using a Moffat-EFF model (Elson et al., 1987), three substructures are required. This finding confirms the superposition of two objects previously identified by De Marchi et al. (1997), along with the addition of a third substructure positioned between A1 and A2, named A3 (see Fig. 1.7). The main properties of these substructures are in Table 1.2.

SSC-A		
Properties	Value	Reference
Mass	$5.5 \times 10^5 M_\odot$	Mayya et al. (2020)
Half-light radii	2.2 pc	Hunter et al. (2000)
Populations	Wolf-Rayet, red super giants and type O	González Delgado et al. (1997) and Origlia et al. (2001)
Young age (A2)	4 Myr	Mayya et al. (2020), Álvarez Cruz (2022), Hunter et al. (2000), and Origlia et al.
Old Age (A1)	7 Myr	(2001)
Component's distance	$d_{sep} = 3$ pc	Hernández Prado (2022)

Table 1.1: Properties of the Super Star Cluster A in NGC 1569.

Cluster ID	r_d [pc]	r_c [pc]	r_t [pc]	$L_t[L_\odot]$	$M_t[M_\odot]$	$\rho_0[M_\odot/\text{pc}^3]$	σ [km/s]
A1	1.2339	0.7140	12.0143	2.9×10^6	9.4×10^4	1.8×10^4	9.0124
A2	0.4450	0.4420	11.0044	1.8×10^7	5.4×10^5	9.9×10^3	2.3258
A3	0.5876	0.3400	13.6079	2.8×10^5	8.5×10^3	1.5×10^4	2.8754

Table 1.2: Structural parameters for a simulation of the composition of SSC-A using nProfit (Hernández Prado, 2022).

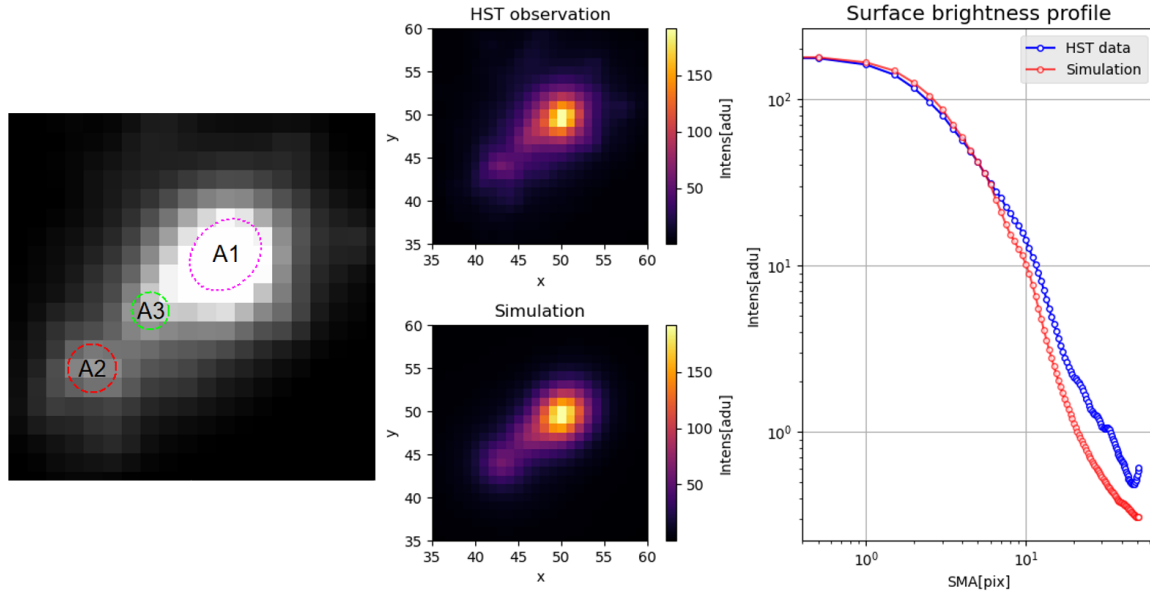


Figure 1.7: Observations from HST data show the structures that comprise SSC-A (left). A comparison is made between the HST observation and the simulation, with the upper and bottom panels representing each, respectively (middle). The surface brightness profile from the HST data and the simulation is also shown, with blue and red lines plotted, respectively (right). Adapted from Hernández Prado (2022).

Chapter 2

Theory

2.1 Fluid Dynamics

Gravity and electromagnetic forces, as well as pressure gradients, shape the dynamics of a fluid like the interstellar medium which is a highly complex one. The FLASH code, in conjunction with the Piecewise Parabolic Method (PPM), is utilized to address a particular challenge: the formation of a second star cluster in close proximity to an existing massive star cluster within the central region of NGC 1569. The two clusters are separated by a mere 3 pc in projection and have an age difference of only 3 Myr (Hernández Prado, 2022; Álvarez Cruz, 2022). This poses a perplexing question regarding how the second cluster could have formed given the potentially strong feedback from the first cluster, which would likely expel or deplete the surrounding gas, leaving insufficient material for the formation of the second cluster.

To tackle this problem, the hydrodynamical equations are solved using the FLASH code, accurately capturing shocks and discontinuities in the fluid, which is crucial for understanding the dynamics involved. The following principles govern the simulation:

2.1.1 Mass conservation

The continuity equation for mass conservation, represented by:

$$\boxed{\frac{\partial \rho}{\partial t} + \nabla \cdot (\rho \mathbf{u}) = S}, \quad (2.1.1)$$

ensures that the rate of mass change within a region is balanced by the net flow within that same region. Where ρ is the density, \mathbf{u} the fluid velocity, ∇ the nabla operator, and the term S represents the net rate of mass injection or depletion within the fluid, accounting for sources and sinks.

2.1.2 Momentum conservation

The momentum conservation equation, given as:

$$\boxed{\rho \frac{D\mathbf{u}}{Dt} = -\nabla p + \rho \mathbf{g}}, \quad (2.1.2)$$

describes how fluid element momentum is affected by pressure gradients and gravitational forces. Where p represents the pressure and \mathbf{g} the gravitational force.

2.1.3 Energy conservation

The energy conservation equation incorporates internal energy changes, work from expansion or compression, and heat transfer. It can be expressed as:

$$\boxed{\frac{\partial \varepsilon}{\partial t} + \nabla \cdot [(\varepsilon + p)\mathbf{u}] - \rho \frac{\partial \Psi}{\partial t} = -\rho \dot{Q}} \quad (2.1.3)$$

The equation presented tracks the evolution of the total energy per unit mass, taking into account various energy contributions and heating processes. The specific total energy, denoted by ε , is defined as $\varepsilon = \rho(\frac{1}{2}\mathbf{u}^2 + \Psi + U)$, where the terms on the right-hand side represent the specific kinetic energy, potential energy, and internal energy, respectively. Additionally, the term \dot{Q} represents the cooling rate.

In this equation, ρ represents the density, \mathbf{u} is the velocity vector, Ψ denotes the gravitational potential energy, and U represents the internal energy of the gas. The specific kinetic energy term, $\frac{1}{2}\mathbf{u}^2$, accounts for the energy associated with the motion

of gas particles. The potential energy term, Ψ , takes into account the gravitational interactions between gas particles and any mass (e.g., a star or galaxy), or even the self-gravity of the gas. The internal energy term, U , represents the energy due to the random motion and interactions of gas molecules.

The term \dot{Q} represents the cooling rate, which quantifies the amount of energy lost per unit of time due to cooling mechanisms. These mechanisms include radiative cooling, adiabatic cooling, and other processes that remove thermal energy from the system.

2.1.4 Source Terms and Cooling Mechanisms

As it was originally assumed by Chevalier & Clegg (1985), the mechanical energy deposited by massive stars and supernova explosions is thermalized in random collisions of nearby stellar winds and supernovae. The mass and energy deposition rates per unit volume, denoted as q_m and q_e , respectively, are assumed to follow the generalized Schuster stellar density distribution (Ninkovic, 1998; Palouš et al., 2013):

$$\rho_\star(r) = \frac{\rho_{\star 0}}{[1 + (r/R_c)^2]^\beta}, \quad (2.1.4)$$

The energy deposition rate per unit volume, $q_e(r)$, can be described as:

$$q_e(r) = q_{e0} \left[1 + \left(\frac{r}{R_c} \right)^2 \right]^{-\beta} \quad (2.1.5)$$

where q_{e0} is a constant and R_c is the star cluster core radius. The exponent β determines the radial dependence of the energy deposition. Similarly, the mass deposition rate per unit volume, $q_m(r)$, follows a similar expression:

$$q_m(r) = q_{m0} \left[1 + \left(\frac{r}{R_c} \right)^2 \right]^{-\beta} \quad (2.1.6)$$

where q_{m0} is a constant. These equations capture the radial distribution of mass and energy deposition from the stellar processes. The parameter \dot{M} represents the mass

injection rate, and L_{SC} denotes the mechanical luminosity of the star cluster.

The constants q_{e0} and q_{m0} are given by:

$$q_{e0} = \frac{3L_{SC}}{4\pi R_{SC}^3 F_{\beta}(R_{SC})} \quad (2.1.7)$$

$$q_{m0} = \frac{3\dot{M}}{4\pi R_{SC}^3 F_{\beta}(R_{SC})} \quad (2.1.8)$$

where R_{SC} represents the star cluster radius, and $F_{\beta}(R_{SC})$ is the Gauss hypergeometric function, ${}_2F_1(3/2, \beta, 5/2, -r^2/R_c^2)$.

These equations, derived from Palouš et al. (2013), incorporate the spatial distribution of mass and energy deposition from the massive stars and supernovae.

Additionally, the cooling mechanisms, such as the Schure et al. (2009) cooling function and gas-grain collisions at high temperatures, play a crucial role in regulating the temperature of the gas. These cooling mechanisms, along with the source terms, contribute to the comprehensive understanding of the formation and evolution of star clusters in the central region of NGC 1569.

2.2 Star Cluster Formation

Molecular clouds are cold, dense regions of gas having extremely complex hierarchical morphologies that possess the necessary properties to form stars through gravitational collapse, a process that is classically understood via the Jeans instability (Draine, 2011). They range in mass from $10^3 M_{\odot}$ for the smallest clouds, all the way up to $10^7 M_{\odot}$ for giant molecular clouds (GMCs). Examples of these include the Taurus star-forming region of low-mass stars (Galli, P. A. B. et al., 2019) and the Orion GMC, which hosts both high-mass and low-mass stars (Bally, 2008).

In order to form stars, the molecular cloud has to collapse driven by the gravitational force overcoming the outward-directed pressure. Considering an idealized unmagnetized and non-rotating cloud, a steady-state solution can be established:

$$\frac{\partial \rho}{\partial t} + \nabla \cdot (\rho \mathbf{u}) = 0 \quad (2.2.1)$$

$$\frac{\partial \mathbf{u}}{\partial t} + \mathbf{u} \cdot \nabla \mathbf{u} = -\frac{1}{\rho} \nabla p - \nabla \Psi \quad (2.2.2)$$

where ρ is the density, t the time, \mathbf{u} the velocity, p the pressure, ∇ the nabla operator, and Ψ the gravitational potential. Considering plane-wave perturbations and the isothermal case the equations 2.2.1 and 2.2.2 become:

$$\frac{\partial \Delta \rho}{\partial t} + \rho_0 \frac{\partial \Delta \mathbf{u}}{\partial x} = 0 \quad (2.2.3)$$

$$\rho_0 \frac{\partial \Delta \mathbf{u}}{\partial t} = -c_s^2 \frac{\partial \Delta \rho}{\partial x} - \rho_0 \frac{\partial \Delta \Psi}{\partial x} \quad (2.2.4)$$

where c_s is the sound speed and Δ represents the change in the property by the perturbation. And with the Poisson equation also becoming:

$$\frac{\partial^2 \Delta \Psi}{\partial x^2} = 4\pi G \Delta \rho \quad (2.2.5)$$

Applying the divergence to the equation 2.2.3 and 2.2.4 and combining them, it follows:

$$\frac{\partial^2 \Delta \rho}{\partial t^2} = c_s^2 \nabla^2 \Delta \rho + (4\pi G \rho_0) \Delta \rho \quad (2.2.6)$$

as previously stated the use of plane-wave density perturbations leads to the dispersion relation:

$$\omega^2 = k^2 c_s^2 - 4\pi G \rho_0 \quad (2.2.7)$$

where ω is the perturbation growth rate as a function of the wavenumber k . In this case, if $\omega^2 < 0$ (imaginary number) we have an exponential growth and an unstable behaviour.

Defining k_J^2 as:

$$k_J^2 = \frac{4\pi G \rho_0}{c_s^2} \quad (2.2.8)$$

and considering $k < k_J$, the Jeans instability will happen as $\lambda > \lambda_J$. Where λ_J is

defined as:

$$\lambda_J = \frac{2\pi}{k_J} = \left(\frac{\pi c_s^2}{G\rho_0} \right)^{1/2} \quad (2.2.9)$$

leading to define the mass contained within a spherical structure of length L_J , capable of collapse, named as **Jeans mass**:

$$M_J = \frac{1}{8\sqrt{\rho_0}} \left(\frac{\pi kT}{G\mu} \right)^{3/2} \quad (2.2.10)$$

It is important to remark that the assumptions made are considering an idealized case. The dominant mechanism supporting the clouds is the turbulence of the gas subsequently causing the gravoturbulent scenario. In other words, the pressure of the supersonic turbulence dominates globally, while locally, the process of collision plays the main role creating density fluctuations forming clumps and filaments which under the Jeans criterion, will collapse and form stars. Nevertheless, all of the above statements bring the conclusion that the process of forming stars takes place in groups, creating **star clusters** (see Figure 2.1).

The remaining gas is evacuated through stellar feedback and the radiative heating associated with young and massive stars.

2.3 Shock Waves

A shock wave is a type of propagating disturbance that travels through a medium at a speed greater than the speed of sound in that medium (Landau & Lifshitz, 1987). Shock waves are characterized by an abrupt and nearly discontinuous change in pressure, temperature, and density of the medium, which occurs over a very small distance called the shock thickness or jump.

There are several scenarios that can lead to the formation of interstellar shocks. For example, stellar winds and supernova explosions generate shock waves as they decelerate upon interaction with the surrounding material. In addition, expanding H II regions can also drive shock waves into neutral gas.

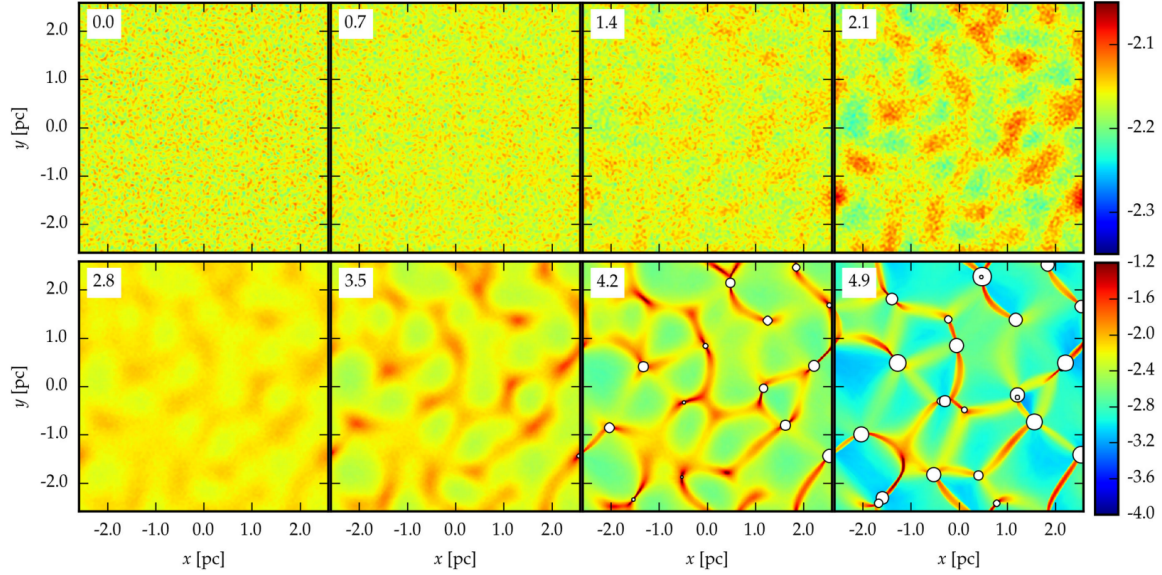


Figure 2.1: Evolution of density of self-gravitational models. The numbers in the top left corresponds to the time in Myr. Sink particles are plotted with circles (Dinnbier et al., 2017).

2.3.1 Rankine-Hugoniot Jump Conditions

For convenience, it is considered a frame of reference that is moving with the shock, and in this frame, the structure appears stationary ($\frac{\partial}{\partial t} = 0$). Hence, it is useful to approximate the shock front as plane-parallel ($\frac{\partial}{\partial y} = \frac{\partial}{\partial z} = 0$). From the equation of mass conservation:

$$\frac{\partial \rho}{\partial t} = -\nabla \cdot (\rho \mathbf{u}) \rightarrow 0 = \frac{\partial}{\partial x}(\rho u_x) \quad (2.3.1)$$

integrating from x_1 to x_2 :

$$\boxed{(\rho u_x)_1 = (\rho u_x)_2} \quad (2.3.2)$$

this is the condition for the equation of mass conservation between the two frames, where u_x is the fluid velocity in the x direction, as well for the following derivations.

From the equation of conservation of momentum:

$$\frac{\partial}{\partial x}(\rho \mathbf{u}_x^2 + p) = -\rho \frac{\partial \Psi}{\partial x} \quad (2.3.3)$$

integrating from x_1 to x_2 :

$$\boxed{(\rho \mathbf{u}_x^2 + p)_1 = (\rho \mathbf{u}_x^2 + p)_2} \quad (2.3.4)$$

To determine the total mechanical work performed on a fluid element i , it is helpful to analyze the surface where the pressure force is applied. This is because the pressure force acts across the surface. To calculate the work done per unit time by the force at each point, one can compute the dot product of the force vector with the velocity at that specific point.

The rate of the work done on the fluid element by external forces is given by:

$$\left(\frac{dE}{dt} \right)_{\text{mech}} = - \int \mathbf{u}_i p dS_i - \int \rho \mathbf{u}_i \frac{\partial \Psi}{\partial x_i} dV \quad (2.3.5)$$

Adding the net heating rate per volume $(\Gamma - \Lambda)$ and heat conduction across the surface $(\kappa \nabla T)$, and by the Gauss Theorem, to convert the surface integrals to volume integrals:

$$\frac{\partial}{\partial x} \left[\frac{1}{2} \rho \mathbf{u}_x \mathbf{u}^2 + \mathcal{U} \mathbf{u}_x + p \mathbf{u}_x - \kappa \frac{dT}{dx} + \rho \mathbf{u}_x \Psi \right] = \Gamma - \Lambda \quad (2.3.6)$$

integrating from x_1 to x_2 and considering that the internal energy per unit volume is:

$$\mathcal{U} = \frac{p}{(\gamma - 1)} \quad (2.3.7)$$

$$\boxed{\left[\left(\frac{\rho \mathbf{u}^2}{2} + \frac{\gamma p}{(\gamma - 1)} \right) \mathbf{u}_x - \kappa \frac{dT}{dx} \right]_1 = \left[\left(\frac{\rho \mathbf{u}^2}{2} + \frac{\gamma p}{(\gamma - 1)} \right) \mathbf{u}_x - \kappa \frac{dT}{dx} \right]_2} \quad (2.3.8)$$

2.4 Collision between Stellar Winds and the Interstellar Medium

As mentioned in the introduction to stellar winds, the evolution of a star can have a significant impact on its surroundings. This occurs through the emission of radiation, as well as the ejection of mass, momentum, and energy in the form of stellar winds.

These winds carry away the mass lost by the star, and as a result of nuclear reactions occurring within the star, the material expelled by these winds becomes chemically enriched. one main example is the production of dust grains which plays a major role in the next generation for the star formation in the region. Also, the kinetic energy released during a supernova event from a massive star is approximately 10^{51} erg, regardless of the initial mass of the star.

The collision between a wind and the interstellar medium produces a **wind-driven bubble** (Weaver et al., 1977). In the case for a collective of massive stars that form within a cluster, the combined effect of the individual winds give rise to **super bubbles**.

This collision, resulting from the interaction between the stellar wind and the interstellar medium, triggers the formation of shocks. These shocks induce heating in both the shocked stellar wind and the swept-up material, creating a hot layer consisting of the shocked wind and ISM. This layer forms between the moving wind and the undisturbed ISM, wanting to expand into the ISM but also backwards into the wind, producing two shocks.

Within the interaction region, the kinetic energy of the wind in the form of mechanical luminosity (L_{mech}):

$$L_{\text{mech}} = \frac{1}{2} \dot{M} v_{\infty}^2 \quad (2.4.1)$$

transforms into heat, where \dot{M} is the mass loss rate and v_{∞} the terminal velocity. The wind temperature can reach temperatures ranging from several times 10^7 K down to 10^4 K, influenced by radiative cooling and adiabatic expansion. Consequently, a wide range of ionization and excitation conditions are observed.

2.4.1 Structure of Wind-driven Bubbles

Shocks are generated through the interaction between the stellar wind and the interstellar medium (ISM), causing heating effects on both the wind and the swept-up material. Specifically, when the wind encounters the ISM, it gives rise to a region of intense heat known as a hot layer, which forms between the advancing wind and the undisturbed ISM.

Due to the high temperature and density of this hot layer, a larger pressure builds up. As a result, the hot layer strives to expand in all directions, irrespective of its original direction of movement. This expansion leads to the formation of two distinct shocks: one on the inner side and another on the outer side of the hot layer.

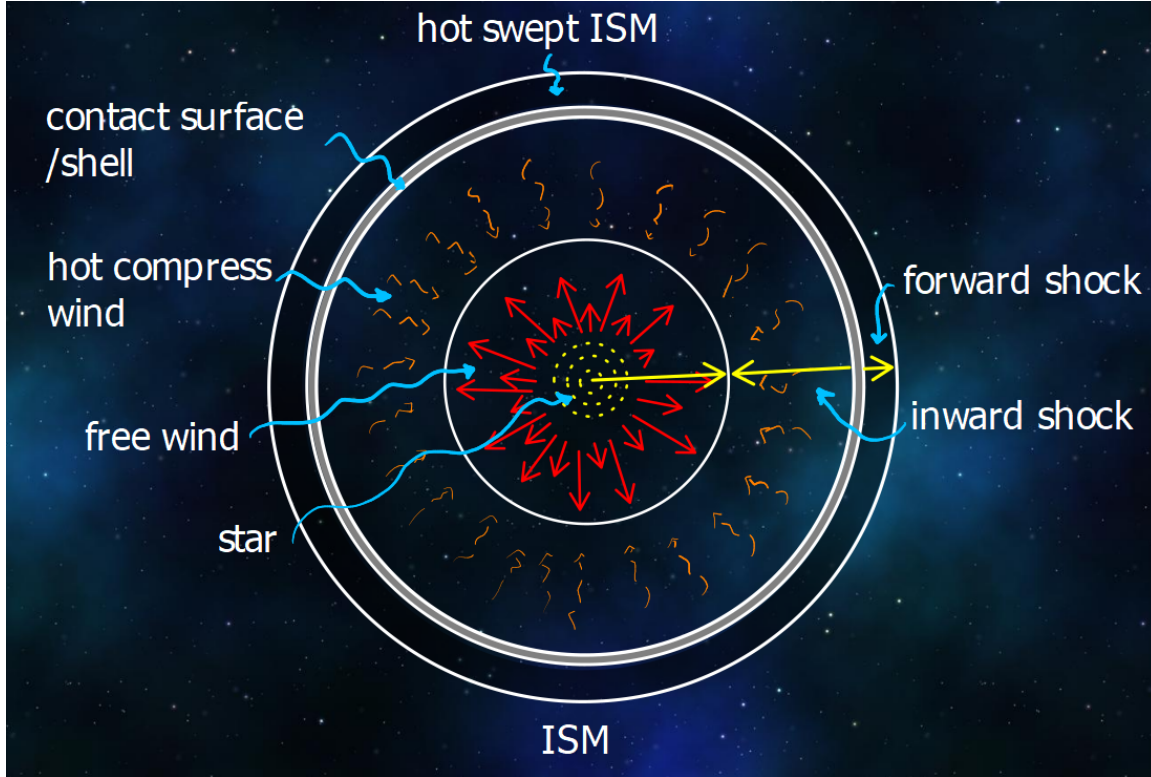


Figure 2.2: Basic structure of a stellar wind interacting with the ISM, consisting in several regions including an emitting star or in the case of a star cluster, the collective wind of all their stars, the interaction region and finally the undisturbed ISM.

Figure 2.2 depicts the fundamental structure of the interaction between a stellar wind and the interstellar medium (ISM). Using the analogy of an "onion-skin", we can visualize the different regions within this structure. The central sphere represents the emitting star, or in the case of a star cluster, the collective wind generated by the cluster. Moving from the innermost region to the outermost region:

The first zone corresponds to the freely flowing supersonic stellar wind. This region consists of the wind gas that is emitted directly from the star or the cluster.

Following the first zone, we encounter a region where the wind gas has been heated as it passes through an inward facing shock. This shock causes the gas to thermalize, and it is identifiable by the temperature structure. When material enters a shock front, it gets heated, with the temperature gradient being from the hotter side to the cooler side.

The third zone represents a dense shell of material that has been swept up by the wind at the outer shock. This shell undergoes radiative cooling, leading to a decrease in temperature.

Moving outward, we reach the fourth zone, which consists of the interstellar material that has been swept up, compressed, and heated by the interaction with the stellar wind.

Finally, the outermost zone represents the undisturbed interstellar medium, unaffected by the interaction with the wind.

By understanding the distinct zones within this structure, we can gain insights into the complex dynamics and thermodynamics of the interaction between stellar winds and the interstellar medium.

2.4.2 Star Cluster Driven Wind Theory

The trigger for a subsequent episode of star formation can potentially arise from the interaction between the interstellar medium and enriched material generated by the evolutionary processes of massive stars within the star cluster, primarily through their stellar winds.

It is essential to note that the formation of stellar winds in star clusters differs from the mechanisms driving winds in individual stars. The latter are predominantly caused by radiation pressure exerted by the outer layers of stars. For instance, Wolf-Rayet stars shed their hydrogen envelopes, resulting in strong winds. However, in the case of star clusters, the cluster wind emerges through the thermalization of kinetic energy due to random collisions among gas ejected by stellar winds and supernovae. This process creates a central overpressure that propels the ejected material, expelling it from the star formation region at supersonic speeds.

The initial model proposed by Chevalier & Clegg (1985) for star cluster winds assumed an adiabatic, stationary, spherically symmetric outflow, neglecting gravitational forces. However, subsequent models incorporated radiative effects into their frameworks, leading to the development of a self-consistent radiative model for stationary winds driven by massive stellar clusters proposed by Silich et al. (2004), by considering the impact of radiative cooling, ensuring that the energy balance and cooling effects were appropriately accounted for the system.

For the adiabatic model, there are three parameters that define the hydrodynamical properties of the wind: total energy (\dot{E}_{sc}) and mass (\dot{M}_{sc}) deposition rates and the radius of the size enclosing the volume of the cluster (R_{sc}), consequently the adiabatic wind terminal velocity is defined as:

$$V_{\infty A} = \sqrt{\frac{2\dot{E}_{sc}}{\dot{M}_{sc}}} \quad (2.4.2)$$

Resulting in an analytic solution for the wind density, pressure and temperature (Chevalier & Clegg, 1985):

$$\rho_c = \frac{\dot{M}_{sc}}{4\pi B R_{sc}^2 V_{\infty A}} \quad (2.4.3)$$

$$P_c = \frac{\gamma - 1}{2\gamma} \frac{\dot{M}_{sc} V_{\infty A}}{4\pi B R_{sc}^2} \quad (2.4.4)$$

$$T_c = \frac{\gamma - 1}{\gamma} \frac{\mu}{k} \frac{q_e}{q_m} \quad (2.4.5)$$

where $B = \left(\frac{\gamma-1}{\gamma+1}\right)^{1/2} \left(\frac{\gamma+1}{6\gamma+2}\right)^{\frac{3\gamma+1}{5\gamma+1}}$, q_e and q_m the deposition rates of energy and mass per unit volume, respectively, γ the ratio of specific heats, μ the mean mass per particle and k the Boltzmann constant, resulting in an expansion velocity that grows from zero at the center of the cluster to the sound speed at the star cluster surface (R_{sc}) producing that within the cluster, the density, pressure and temperature of the wind remains almost uniform, nevertheless, outside the surface of the cluster ($r \gg R_{sc}$), the properties mentioned above approach their asymptotic values such as $\rho_w \sim r^{-1/2}$, $T_w \sim r^{-4/3}$ and $u_w \sim V_{\infty A}$.

In the case of the radiative model proposed by Silich et al. (2004), the presence of a cooling function complicates the attainment of an analytical solution, unlike the adiabatic case. Moreover, the parameters of the star cluster (\dot{E}_{sc} , \dot{M}_{sc} , and R_{sc}) no longer directly determine the properties of the wind. Instead, numerical integration becomes necessary to obtain the solution.

Three types of integral curves arise depending on the position of the sonic point (R_{sonic}) relative to the surface of the star cluster (R_{sc}). The first type is the **stationary wind solution** where the sonic point coincides with the cluster surface ($R_{sonic} = R_{sc}$). Within the cluster, the flow remains subsonic, while it becomes supersonic outside the cluster.

The second type is the **breeze solution** where the sonic point is located outside the cluster ($R_{sonic} > R_{sc}$). In this case, the central temperature is lower compared to the stationary solution, and the velocity reaches its maximum value outside the star cluster. Consequently, the flow remains subsonic throughout the entire region.

The third type is the **unphysical double value solution** where the sonic point is inside the cluster ($R_{sonic} < R_{sc}$). In this scenario, the central temperature exceeds that of the stationary case.

The types of integral curves are shown in Fig.2.3 adapted from Silich, Bisnovatyi-Kogan, Tenorio-Tagle & Martínez-González (2011), note that the solutions correspond as: the breeze solution named the N-type at R_N , the unphysical double value solution named the D-type at R_D , and the stationary wind solution at R_{sc} .

These integral curves demonstrate that a stationary wind solution exists only if the outflow crosses the star cluster surface at the local sound speed. This observation holds true for both the adiabatic and radiative solutions, indicating that the concept of a stationary wind is valid under these conditions.

To obtain the stationary wind solution, it is necessary to find the wind central density and temperature that establishes the sonic point at the star cluster surface, this parameters (n_c and T_c) are dependent from each other in the radiative case and they are related by:

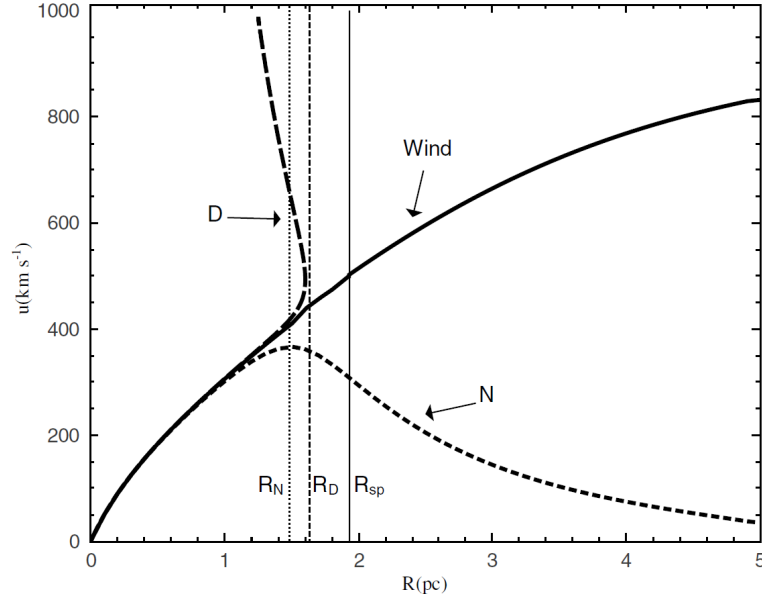


Figure 2.3: Integral curves depict different scenarios based on the central temperature of the wind. When the central temperature exceeds the stationary case, the integral curve extends to the sonic point located inside the cluster at R_D , where the velocity becomes supersonic, this solution, known as the "unphysical double value solution". On the other hand, if the central temperature is lower than the stationary case, the integral curve reaches its maximum velocity at R_N , after which the velocity gradually decreases. In this case, the wind remains subsonic throughout, this solution is referred to as the "breeze solution." The unique wind solution corresponds to the scenario where the integral curve passes through the sonic point at R_{sc} and the flow becomes supersonic for larger radii. This figure is adapted from Silich et al. (2011).

$$n_c = \sqrt{\frac{q_e - \frac{q_m}{\gamma-1} c_c^2}{\Lambda(T_c)}} = q_m^{1/2} \sqrt{\frac{\frac{V_{\infty A}^2}{2} - \frac{c_c^2}{\gamma-1}}{\Lambda(T_c)}} \quad (2.4.6)$$

where $\Lambda(T)$ is the cooling function, c_c the sound speed in the center and the adiabatic terminal velocity wind is related with the deposition rates as $V_{\infty A} = \sqrt{\frac{2q_e}{q_m}}$.

Silich et al. (2004) also revealed the existence of a critical threshold for the energy input, where the impact of radiative cooling becomes significant. As the central temperature reaches its maximum value, the central density and central pressure tend to decrease, eventually approaching zero. However, it is important to note that the

central pressure initially increases up to a certain point as the central temperature decreases. This increase is limited by the radiative cooling of the gas.

As the central temperature decreases further, there is no compensation for the decrease in pressure. Consequently, for certain star cluster parameters, the sonic point for compact clusters shifts inward the surface, moving inside the star cluster itself. This implies a significant change, as the stationary wind solution, which was present when the sonic point coincided with the star cluster surface, vanishes under these circumstances.

The interaction between neighboring cold supersonic winds leads to the rapid formation of oblique reverse shocks. These shocks serve to collimate the outflow, creating a network of narrow, dense, and cold filaments. These filaments become embedded within a hot surrounding medium.

For super star clusters with super-critical energy input rates, radiative cooling leads to a catastrophic cooling regime where the stationary wind solution is inhibited.

It is important to emphasize that the model proposed by Silich et al. (2004) is designed for homogeneous clusters, meaning that the stellar density within the cluster is assumed to be uniform. However, this does not reflect the actual composition of real clusters. Rodríguez-González et al. (2007) discovered an analytical non-radiative solution specifically for power-law stellar density distributions. This finding suggests that in cases where the stellar density distribution is steep, radiative cooling can play a crucial role, particularly in the central regions of the cluster.

Additionally, in the Rodríguez-González et al. (2007) solution, where the stellar density eventually reaches zero at a certain distance from the center of the star cluster, known as the cutoff radius, the transition between the subsonic and supersonic regimes occurs precisely at this point.

In their subsequent work Silich et al. (2011) a steady-state semi-analytical hydrodynamical solution was presented. This solution was specifically developed to account for stellar clusters with an exponential stellar density distribution while incorporating radiative cooling effects.

They considered a young star cluster with constant energy and mass disposition rates,

L_{sc} and \dot{M}_{sc} , and an exponential stellar density distribution:

$$\rho_*(r) = \rho_{*0} \exp\left(-\frac{r}{R_c}\right) \quad (2.4.7)$$

where ρ_{*0} is the central stellar density and R_c the core radius of the cluster. The total mass of the cluster is obtained by:

$$M_{sc} = 4\pi \int_0^\infty \rho_{*0} r^2 \exp\left(-\frac{r}{R_c}\right) dr = 8\pi \rho_{*0} R_c^3 \quad (2.4.8)$$

where the half-mass radius of the cluster is $R_{hm} = 2.67R_c$ for the exponential distribution. The energy and mass deposition rates per unit volume, q_e and q_m are:

$$q_e(r) = q_{e0} \exp\left(-\frac{r}{R_c}\right) \quad \wedge \quad q_m(r) = q_{m0} \exp\left(-\frac{r}{R_c}\right) \quad (2.4.9)$$

where q_{e0} and q_{m0} are related as:

$$q_{e0} = \frac{L_{sc}}{8\pi R_c^3} \quad \wedge \quad q_{m0} = \frac{\dot{M}_{sc}}{8\pi R_c^3} \quad (2.4.10)$$

The hydrodynamic equations for a stationary, spherically symmetric flow driven by stellar winds and supernovae explosions are:

$$\frac{1}{r^2} \frac{d}{dr} (\rho u r^2) = q_m \quad (2.4.11)$$

$$\rho u \frac{du}{dr} = -\frac{dP}{dr} - q_m u \quad (2.4.12)$$

$$\frac{1}{r^2} \frac{d}{dr} \left[\rho u r^2 \left(\frac{u^2}{2} + \frac{\gamma}{\gamma-1} \frac{P}{\rho} \right) \right] = q_e - Q \quad (2.4.13)$$

where u , P , ρ and γ are the outflow velocity, thermal pressure, density and ratio of the specific heats, respectively, also, $Q = n_e n_i \Lambda(T, Z)$ is the cooling rate and $\Lambda(T, Z)$ the cooling function which depends on the temperature and metallicity.

By the integration of the equation of mass conservation 2.4.11 assuming that the velocity and density of the flow are finite in the center of the star cluster and equating

it with the derivation of equation 2.4.12, gives:

$$\frac{du}{dr} = \frac{(\gamma - 1)(q_e - Q) + \frac{(\gamma+1)q_m u^2}{2} - \frac{2\rho u c^2}{r}}{\rho(c^2 - u^2)} \quad (2.4.14)$$

where c is the local speed of sound $c^2 = \gamma P/\rho$. Its crucial to know that when the radiative cooling is taken into consideration, the central gas density ρ_c and the central temperature T_c are related by (Silich et al., 2004; Sarazin & White, 1987)

$$\rho_c = q_{m0}^{1/2} \left[\frac{\frac{V_{\infty A}^2}{2} - \frac{c_0^2}{\gamma-1}}{\Lambda(Z, T_c)} \right]^{1/2} \quad (2.4.15)$$

where c_0 is the sound speed in the star cluster center. If the central temperature is known, the thermal pressure is defined as:

$$P_c = k n_c T_c \equiv \frac{k_B \rho_c T_c}{\mu_a} \quad (2.4.16)$$

where n_c is the numerical density in the center, T_c the central temperature, ρ_0 the central gas density, k_B the Boltzmann constant and μ_a the mean mass per particle. The value of the central temperature determines the unique solution which passes the singular point, where in equation 2.4.14, vanishes itself and the subsonic flow in the inner zone ($r < R_{sp}$) becomes supersonic out the star cluster surface, thus, electing the central temperature value leads to the wind solution defining the singular point position.

Silich et al. (2011) present their key findings by varying three parameters: mechanical luminosity (L_{sc}), terminal wind velocity ($V_{\infty A}$), and core radius (R_c).

In the first parameter case (L_{sc}), the flow velocity near the center exhibits an almost linear increase with radius. It passes through a singular point and gradually approaches the terminal speed value. The influence of strong radiative cooling becomes evident in the most energetic clusters. In such cases, the terminal wind velocity is smaller due to the reduction in thermal energy at the center caused by radiative cooling. Although the temperature deviates from the quasi-adiabatic profile, it does not significantly affect the density distribution.

Moving on to the second parameter ($V_{\infty A}$), the calculated wind terminal speed closely resembles the adiabatic value when $V_{\infty A}$ is large. However, noticeable differences arise at lower values of $V_{\infty A}$. This discrepancy is a consequence of the higher density of the wind when the adiabatic wind terminal speed is smaller. The increased density leads to more pronounced radiative cooling, which removes a fraction of the deposited energy and subsequently decreases the flux of mechanical energy and the wind terminal speed.

Lastly, in the third parameter case (R_c), the strength of radiative cooling intensifies when R_c is small. In other words, the wind speed experiences faster growth when the cluster is more compact. This compactness also impacts the central density, which increases for smaller core radii.

In summary, the density within the wind increases with the mechanical luminosity. In other words, if the cluster is more massive, the density of the wind grows accordingly. Additionally, the density also increases if the wind is mass-loaded or if the cluster exhibits a more compact configuration.

The turnoff point in the temperature distribution undergoes a shift towards the center of the star cluster. As a result, the temperature rapidly decreases to around 10^4 K. At this point, assuming that the outflow is ionized, the wind becomes isothermal. This specific regime is known as the "catastrophic cooling regime." In this regime, the singular point detaches from its quasi-adiabatic position and moves closer to the center of the cluster.

Subsequently, Palouš et al. (2013) developed a model to describe the winds driven by stellar clusters using a generalized Schuster stellar density distribution. Elson et al. (1987) discovered that the generalized Schuster model, specifically with a value of $\beta = 1.75$, offers a highly accurate fit to the stellar densities observed in young stellar clusters within the Large Magellanic Cloud (LMC).

Moreover, Mengel et al. (2002) conducted Hubble Space Telescope (HST) observations of young stellar clusters in the Antennae galaxies. Their findings indicated that a 2-D King model, corresponding to a projected generalized 3-D Schuster model, provides the best agreement with the observed stellar surface densities in those clusters.

Palouš et al. (2013) examined a young, compact, and spherical cluster characterized by constant total mass and energy deposition rates, denoted as \dot{M}_{sc} and L_{sc} respectively. The stellar mass density distribution within the cluster was described by a generalized Schuster model, given by the equation:

$$\rho_*(r) = \frac{\rho_{*0}}{\left[1 + \left(\frac{r}{R_c}\right)^2\right]^\beta} \quad (2.4.17)$$

here, ρ_{*0} represents the central density, R_c corresponds to the core radius, and β the steepness of the stellar distribution.

The mass of the cluster, denoted as $M_{sc}(r)$, can be expressed as an integral:

$$M_{sc}(r) = \int_0^r \frac{4\pi\rho_{*0}x^2dx}{\left[1 + \left(\frac{x}{R_c}\right)^2\right]^\beta} = \frac{4\pi}{3}\rho_{*0}r^3 {}_2F_1\left(\frac{3}{2}, \beta, \frac{5}{2}, -\frac{r^2}{R_c^2}\right) \quad (2.4.18)$$

The expression involving the Gauss hypergeometric function ${}_2F_1$ is defined as a power law, and it can be abbreviated as $F_\beta(r)$ for brevity.

Note that if $\beta \leq \frac{3}{2}$ and $r \rightarrow \infty$, the mass of the cluster is infinite, on the other hand if $\beta \geq \frac{3}{2}$, the cumulative mass is finite, nevertheless, to keep the cluster mass finite at $\beta \leq \frac{3}{2}$, the stellar density distribution is truncated at R_{sc} .

The sources of mass and energy are:

$$q_e(r) = q_{e0} \left[1 + \left(\frac{r}{R_c}\right)^2\right]^{-\beta} \quad \wedge \quad q_m(r) = q_{m0} \left[1 + \left(\frac{r}{R_c}\right)^2\right]^{-\beta} \quad (2.4.19)$$

where q_{e0} and q_{m0} are:

$$q_{e0} = \frac{3L_{sc}}{r\pi R_c^3 F_\beta(R_{sc})} \quad \wedge \quad q_{m0} = \frac{3\dot{M}_{sc}}{r\pi R_c^3 F_\beta(R_{sc})} \quad (2.4.20)$$

Following a similar approach to Silich et al. (2011), Palouš et al. (2013) undertook the same procedure by considering the hydrodynamic equations governing steady-state

spherically symmetric flows driven by star clusters (as depicted in equations 2.4.11, 2.4.12, and 2.4.14). They integrate and equate these equations to derive the main equations in a suitable form for numerical integration. Moreover, they introduce a truncation radius, denoted as R_{sc} , where these main equations undergo changes.

Palouš et al. (2013) employ a combination of 1D numerical calculations, semi-analytical approaches, and full numerical simulations. The latter simulations are performed using the finite-difference Eulerian hydrodynamic code called **FLASH** (Fryxell et al., 2000). These diverse methods enable them to comprehensively explore and analyze the dynamics of the system under investigation.

Based on Palouš et al. (2013) models employing a Schuster stellar density distribution, it has been observed that in typical young star clusters with masses around $10^6 M_\odot$, the significance of radiative cooling is relatively minor. Consequently, the behavior of the model is predominantly quasi-adiabatic.

When the transition to the supersonic regime occurs at the surface of the star cluster, there is an abrupt jump in velocity from subsonic to supersonic. At the cluster's edge, this jump leads to a sharp decrease in density, temperature, and pressure. Conversely, when the sonic point is located inside the cluster, the transitions are much more gradual and smooth, with a more gradual change in these properties.

The influence of radiative cooling on the flow becomes more pronounced as the wind density increases. Cooling is directly proportional to the square of the density, which, in turn, is linearly related to the total mass of the cluster. Hence, as the cluster's mass increases, the impact of radiative cooling becomes more significant.

2.5 Gas expulsion during the early evolution of young star clusters

As mentioned earlier in Chapter 1.1, it has been confirmed that globular clusters exhibit distinct stellar subpopulations. It is proposed that the first generation of stars, referred to as 1G, is formed from pristine matter. Subsequent generations, such as the second generation (2G) and any subsequent generations if they exist, are believed

to originate from either the remaining gas or accreted primordial matter that has undergone enrichment (see Silich et al., 2020; Jiménez et al., 2021, and references therein).

There are several models that propose different mechanisms for the pollution of pristine gas in globular clusters. The "slow" scenario suggests that stellar winds generated by massive stars and supernova explosions expel the residual gas from the cluster, leading to the pollution of the surrounding environment. On the other hand, the "fast" scenario suggests alternative mechanisms for the formation of second-generation (2G) stars. These mechanisms include the contribution of fast-rotating massive stars (Prantzos, N. & Charbonnel, C., 2006) or interacting binary systems (de Mink et al., 2009).

In the work by Wünsch et al. (2017), a model is presented that explores the concept of rapidly cooling star cluster winds. According to this model, dense clumps of enriched matter are formed within the central regions of thermally unstable winds. These clumps act as protective shields against ionizing photons and effectively accumulate matter within these regions. This accumulation process triggers the creation of the second generation of stars even before the occurrence of supernova explosions from massive stars.

The work by Silich & Tenorio-Tagle (2018) highlights a significant concern present in the above models, namely the expulsion or retention of gas and the impact of stellar feedback on this residual gas. There is a commonly held belief that **negative feedback**, which limits the star-forming efficiency through radiative and mechanical feedback from massive stars, leads to the rapid clearing of residual gas from star-forming regions. This idea seems intuitive and effective, especially in denser and more compact clusters. However, recent findings challenge this common assumption, revealing that the situation is not as straightforward as previously thought.

In the study by Silich & Tenorio-Tagle (2017), it is demonstrated that in massive and compact clusters, the wind-driven shells surrounding individual massive stars do not merge, thereby suppressing the formation of a global star cluster wind. This finding sheds light on the unique evolution of clusters formed under extreme conditions, where the interplay between turbulent pressure and strong radiative cooling plays a crucial

role in the expulsion of gas from the clusters. This provides a distinct perspective for understanding the evolution of such clusters.

Despite the inability of wind-driven shells to merge, as mentioned earlier, Silich & Tenorio-Tagle (2018) reveals that the hot shocked gas surrounding individual massive stars continues to grow in the subsonic regime until it merges with the hot bubbles created by neighboring massive stars. This merging process leads to the formation of a global star cluster wind, which effectively expels the residual gas. However, if catastrophic cooling occurs and the shocked gas becomes thermally unstable, the negative stellar feedback is significantly suppressed. Consequently, the hot shock zones do not merge, and the collective wind fails to emerge.

In order to understand the limitations imposed by strong radiative cooling and stellar mass segregation on the expulsion of gas from dense star-forming clouds, it is essential to examine the properties of shocked wind bubbles within a high-pressure intra-cloud medium. This investigation is facilitated by the work conducted by Silich & Tenorio-Tagle (2018) and Silich et al. (2020). As discussed in subsection 2.4.1, massive stars generate fast stellar winds, which are subsequently thermalized by reverse shocks and drive the leading shock into the interstellar medium (ISM). There exists a critical density, where the wind-driven shells fail to merge, at which the pressure in the hot shocked wind equals that of the turbulent ambient medium. Even though the hot shocked wind zone continues to expand due to the continuous deposition of mass and energy by the central star, it either merges with neighboring hot shocked winds or undergoes catastrophic cooling upon reaching its cooling radii R_{cool} (defined as the radius at which the temperature drops to 10^4 K).

Numerical results from Silich & Tenorio-Tagle (2018) study are presented in Figure 2.4, illustrating a $3 \times 10^5 M_\odot$ cluster that is 1 million years old and has a radius of the mass-segregation zone of $R_{sg} = a$. The cluster is formed within a $10^6 M_\odot$ cloud with a metallicity of $Z = 0.02 Z_\odot$. In the figure, the dashed, solid, and dotted lines represent the distribution of hydrodynamic variables in the subsonic shocked wind surrounding an individual star located at the center of the cluster, with different core radii: $r_c = 2$ pc, $r_c = 3$ pc, and $r_c = 4$ pc, respectively. The vertical lines indicate the half-distance to the nearest massive star X , in each case.

These results have several implications. Firstly, as the gas velocity decreases rapidly due to the thermal pressure gradient within the shocked wind zone (see panel a), the gas reaches a state of negligible velocity, where the thermal pressure balances with the ambient gas pressure, where remains homogeneous throughout the shocked wind zone (see panel b). In the case of more extended clusters, radiative cooling is negligible, and both the density and temperature remain unchanged. Consequently, the shocked wind remains hot as it merges with neighboring shocked wind bubbles, leading to the expulsion of intra-cluster gas.

The situation described above gives rise to a highly intricate scenario. In compact or massive clusters, radiative cooling becomes a dominant factor as seen in Palouš et al. (2013) (subsection 2.4.2), the gas velocity drops rapidly reaching a balance in pressure. However, the region occupied by the shocked star cluster wind behaves adiabatically in a narrow zone behind the inward shock, and cools catastrophically at large distances. As the thermal instability sets in, a multi-phase intra-cluster medium is produced: hot small bubbles, partially photoionized gas and dense clumps.

From the analysis of Figure 2.4, it is clear that even though the shocked winds may cool before merging in the central zone, they eventually merge at the periphery of the mass segregation zone. This observation highlights the significant influence of mass segregation on the merging process. In cases where the mass segregation radius exceeds the cluster core radius, i.e., $R_{sg} > r_c$, the ambient gas pressure at the edge of the cluster is lower compared to clusters with $R_{sg} = r_c$. Consequently, the reverse shocks are situated further away from their respective stars, and for the shocked winds to cool before merging, the clouds need to have a compact structure. Failure to meet this criterion increases the likelihood of merging. On the other hand, when $R_{sg} \leq r_c$, the intra-cloud gas pressure grows towards the center, resulting in higher densities and faster gas cooling, which inhibits the expansion of the shocked winds (Silich & Tenorio-Tagle, 2018).

Jiménez Villarraga (2022) also examined the structure of single wind-driven bubbles to investigate the possibility of shocked wind gas merging. In Figure 2.5, the structure of two individual wind-driven bubbles is depicted, one located at the center of the cloud and the other at a larger distance of $r = 2.2$ pc in a cloud with total mass

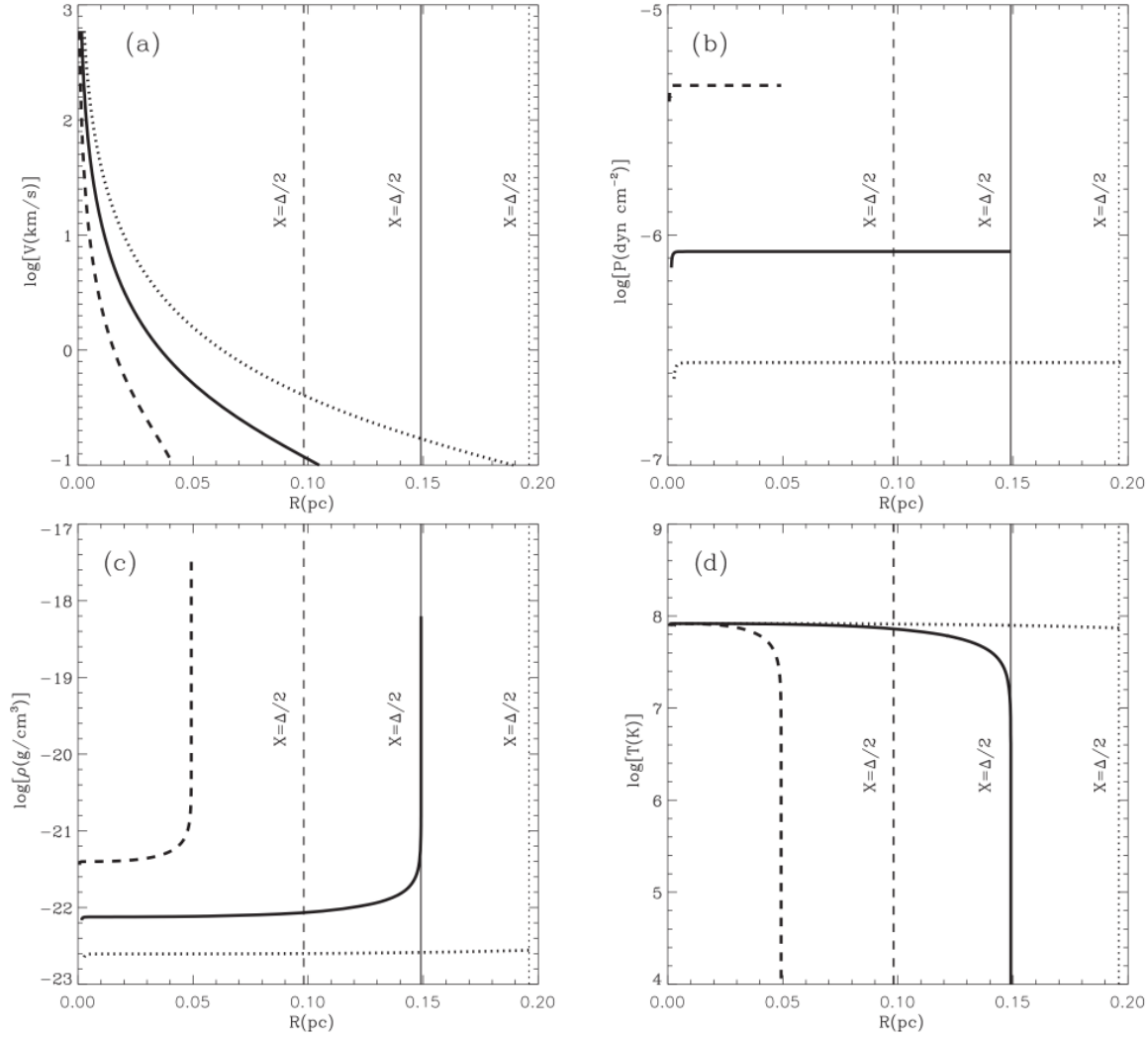


Figure 2.4: The velocity distribution (panel a), pressure distribution (panel b), density distribution (panel c), and temperature distribution (panel d) of the shocked wind zone around individual stars located at the center of a star-forming cloud are depicted. In the figure, dashed, solid, and dotted lines represent the distributions of these variables in clouds with different core radii: 2 pc, 3 pc, and 4 pc, respectively. Additionally, vertical dashed, solid, and dotted lines indicate the average half distance between neighboring massive stars in each respective case. The figure has been adopted from Silich & Tenorio-Tagle (2018).

$M_t = 7.14 \times 10^5 M_\odot$, an efficiency parameter of $\varepsilon = 0.1$, core radius $r_c = 0.87$ pc, and metallicity $Z = 10^{-2} Z_\odot$. It can be observed that the half distance between

stars is smaller in the central zone of the cloud compared to the outskirts. However, the higher densities and pressures in the central region cause the wind bubbles to stall before merging, while at larger distances, merging does occur. These findings support the conclusions of Silich & Tenorio-Tagle (2018) and the importance of **mass segregation**.

In Figure 2.6, the cooling radius R_{cool} and the average separation between neighboring massive stars are plotted as a function of distance from the center of the cloud. The plot illustrates that as the distance increases from the cloud center, there is a notable decrease in the catastrophic cooling of shocked gas, resulting in higher residual pressures and densities. This phenomenon inhibits the efficient expulsion of leftover gas from the central zones. However, the gas expulsion is less inhibited in the outskirts of the cloud. At a specific radius where R_{cool} equals a certain value X , referred to as the super-wind radius R_{SW} (Jiménez Villarraga, 2022).

Silich et al. (2020) conducted a dedicated study on an embedded cluster located in NGC 5253, in conjunction with the parent cloud D1. The investigation included the presence of a significant turbulent pressure in the central zones of the cloud. This high pressure environment can potentially lead to individual wind-blown bubbles experiencing pressure confinement before encountering neighboring bubbles.

In their analysis, Silich et al. (2020) focused on the central zone of the D1 cloud with a radius of $r = 2.8$ pc. The gas and stars in this region contribute approximately 35% and 65%, respectively, to the virial mass. Specifically, the gas mass (M_{gas}) is estimated to be $8.75 \times 10^4 M_{\odot}$, while the stellar mass (M_{*}) is estimated to be $1.625 \times 10^5 M_{\odot}$.

Comparing these findings with the model predictions from Silich & Tenorio-Tagle (2018), it was expected that the hot shocked winds around individual stars would merge and form a global wind within a timescale of less than 10^5 years. However, observations from the Atacama Large Millimeter Array (ALMA) showed that the molecular gas in the parent cloud D1 remained mostly undisturbed. This discrepancy prompted a re-examination of several processes that were not previously considered, such as the mass loading from pre-main-sequence stars (PMS). The presence of PMS stars could potentially suppress or delay the formation of a global star cluster wind and impede the expulsion of residual gas from the system.

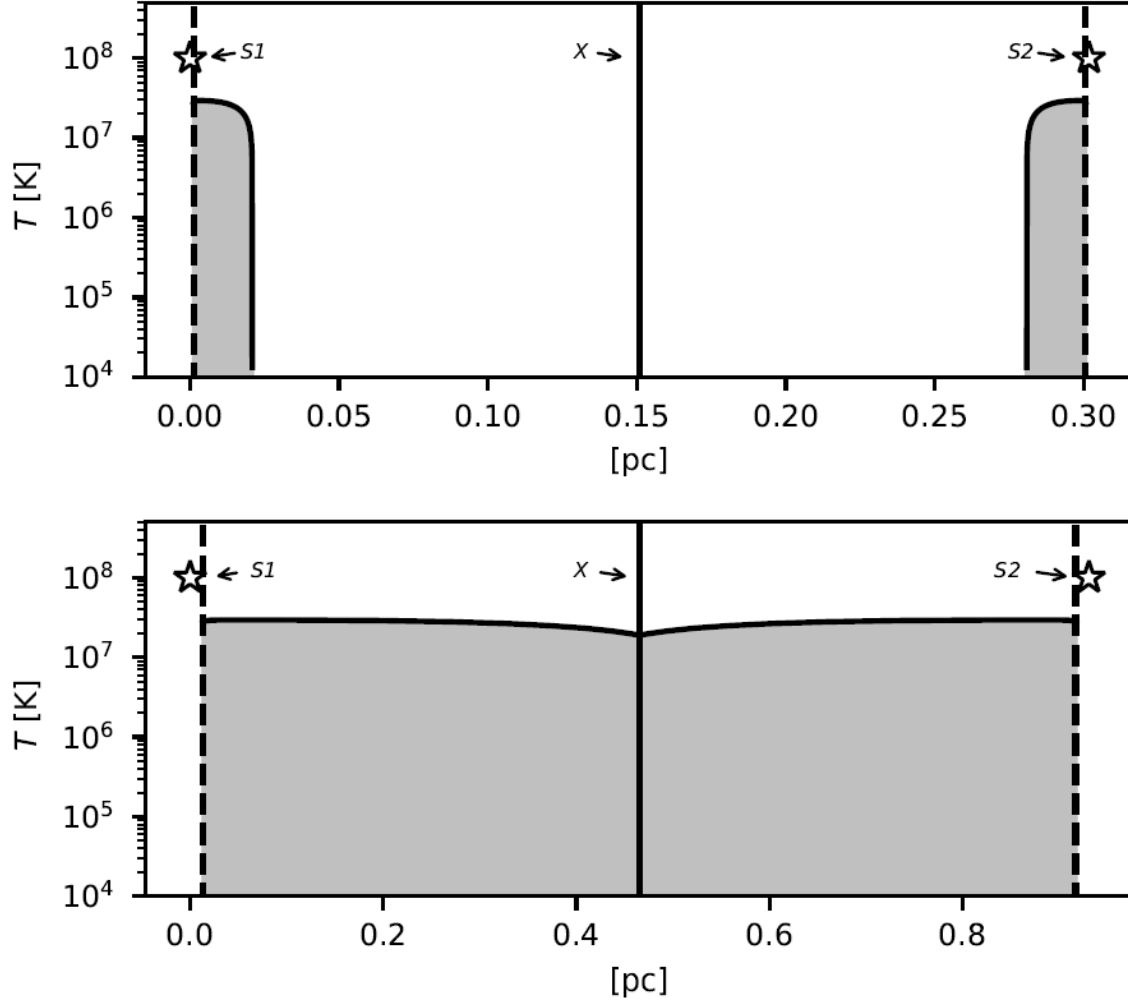


Figure 2.5: The temperature distribution is shown in the top and bottom panels for two neighboring wind-driven bubbles located within a cloud. The cloud has a total mass of $M_t = 7.14 \times 10^5 M_\odot$, an efficiency parameter of $\varepsilon = 0.1$, a core radius of $r_c = 0.87$ pc, and a metallicity of $Z = 10^{-2} Z_\odot$. In the top panel, the neighboring bubbles are located at the center of the cloud, while in the bottom panel, they are positioned at a distance of $r = 2.2$ pc. The x-axis represents the distance between the stars, denoted as S1 and S2. The dashed lines indicate the positions of the reverse shocks for each star, and the vertical solid lines represent the half distance between the stars. The shaded regions illustrate the shocked wind zones. Adapted from Jiménez Villarraga (2022)

The distribution of massive stars ($M > 8M_\odot$) scales with the cluster mass as $N_{mass} \approx$

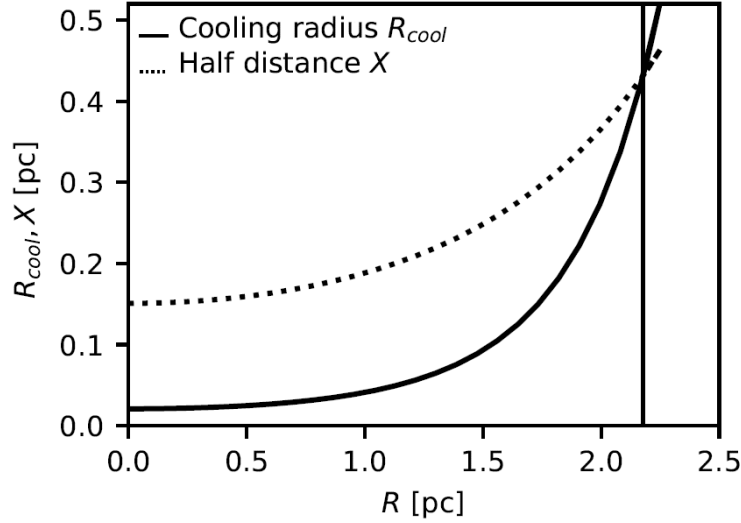


Figure 2.6: Cooling radius (solid line) and the half distance X (dotted line) as a function of the position within the gas cloud R for the same case as Figure 2.5, the vertical solid line shows where $R_{\text{cool}}/X = 1$. Adapted from Jiménez Villarraga (2022)

$10^4(M_*/10^6 M_\odot)$ where the half distance X between neighbouring massive stars at different distances from the center of the cluster is:

$$X(r) = b \left[3 \left(\frac{\pi}{2} \right)^{1/2} \exp \left[\frac{1}{2} \left(\frac{r}{b} \right)^2 \right] \right]^{1/3} N_{\text{mass}}^{-1/3} \quad (2.5.1)$$

here, b represents the core radius of the stellar mass distribution. This equation describes how the half distance between massive stars varies with distance from the cluster center.

Additionally, the number of low-mass pre-main-sequence (PMS) stars (with masses lower than $3M_\odot$) scales with the star cluster mass according to $N_{\text{PMS}} \approx 1.5 \times 10^6(M_*/10^6 M_\odot)$. This implies that in young stellar clusters, there can be over 100 low-mass PMS stars located within a region with a radius $r \leq X$ around each massive star. These low-mass stars possess protostellar discs, which continuously lose mass due to various processes. However, the dominant process influencing these protostellar discs is photoevaporation caused by the UV radiation emitted by massive stars.

The impact of mass loading is presented in Figure 2.7, which illustrates the changing ratio of R_{cool}/X as a function of distance for a 1 Myr cluster. The figure compares different models with varying mass loading rates, $\dot{M}_{PMS} = 8 \times 10^{-9} M_{\odot} \text{ yr}$ and $\dot{M}_{PMS} = 5 \times 10^{-8} M_{\odot} \text{ yr}$.

In the case of the lower mass loading rate, the hot shocked winds rapidly merge, leading to the formation of a global star cluster wind almost instantaneously. However, in the scenario with the higher mass loading rate, the hot shocked wind bubbles cool before they can merge.

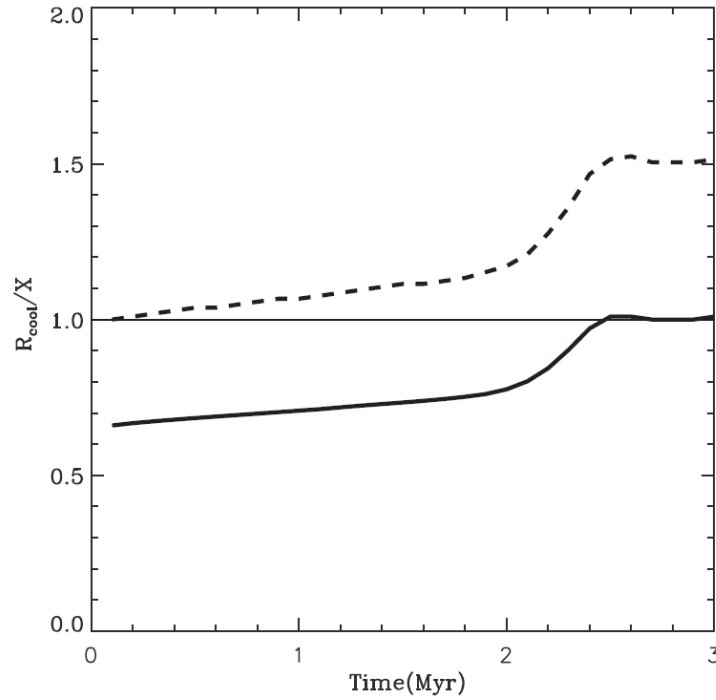


Figure 2.7: The cooling radius, denoted as R_{cool} , is normalized to a half-distance X between neighboring massive stars in the center of the star cluster. In the plot, the dashed and solid lines correspond to models with mass loss rates of $\dot{M}_{PMS} = 8 \times 10^{-9} M_{\odot} \text{ yr}$ and $\dot{M}_{PMS} = 5 \times 10^{-8} M_{\odot} \text{ yr}$, respectively. Figure adapted from Silich et al. (2020)

In the specific case of cloud D1, the presence of mass loading impedes the expulsion of the residual gas for several million years. During this time, the majority of protostellar discs dissipate, resulting in a reduction of the mass loading rate. This phenomenon

helps to explain why the CO gas within the NGC 5253 embedded cluster remains mostly undisturbed, as detailed in the work by Silich et al. (2020).

A hot gas volume filling factor f_X can be obtained by the cooling radii R_{cool} at different distances from the star cluster center:

$$f_X = \frac{4\pi}{R^3} \int_0^R n_{mass}(r) R_{cool}^3(r) r^2 dr \quad (2.5.2)$$

where $n_{mass}(r)$ is the massive star number density at different distances from the star cluster center and R is the radius of the star cluster volume.

The calculation of the filling factor f_X is shown in Figure 2.8, where is used the assumption of $\dot{M}_{PMS} = 5 \times 10^{-8} M_\odot \text{ yr}$ and $R = 1 \text{ pc}$. The filling factor f_X grows slowly from ~ 0.3 to ~ 0.5 in 2 Myr, then, increases rapidly until approach unity at $\sim 2.4 \text{ Myr}$, due the increase of stellar wind power, occupying most of the star cluster central zone, even when the global cluster is still suppressed.

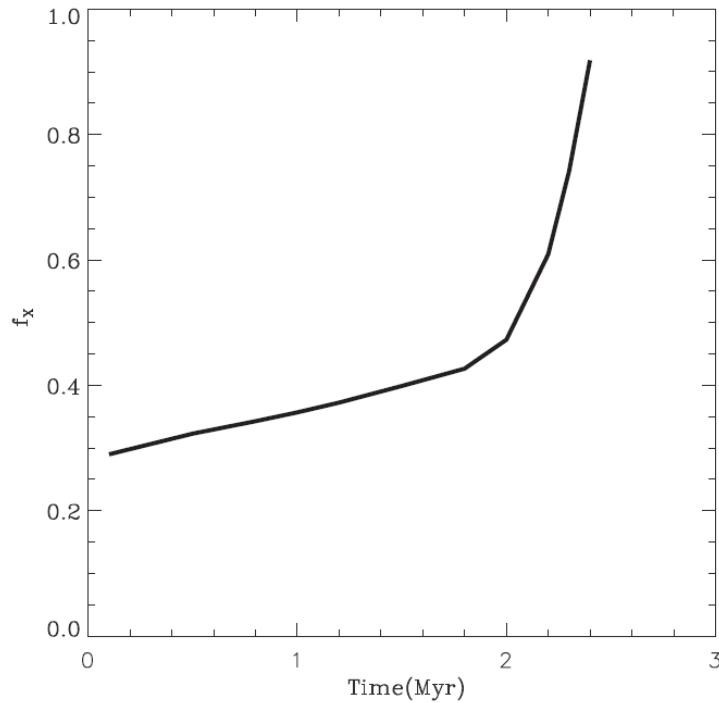


Figure 2.8: The hot gas filling factor f_X in the central zone of the cluster as a function of time. Figure adapted from Silich et al. (2020)

Chapter 3

FLASH Simulation

This chapter presents an overview of the modules utilized in a set of 3-D hydrodynamic simulations conducted with the Adaptive Mesh Refinement (AMR) code FLASH (Fryxell et al., 2000). The block-cell structure is a fundamental feature of the AMR FLASH code. In this structure, the computational domain is divided into a hierarchy of rectangular blocks. Each block is further subdivided into a collection of smaller cells that hold the numerical data used in the simulations. The block-cell structure allows for adaptive mesh refinement, where different regions of the simulation can have different levels of resolution based on the physical properties and phenomena being studied.

The FLASH code (version 4.6) is used to investigate the mechanical feedback of a young massive stellar cluster surrounded by a complex molecular environment. By accurately capturing the interactions between the stellar cluster and its environment, including the effects of gravity, radiative cooling, and turbulence, FLASH offers valuable insights into the possibility of sequential star cluster formation within an environment significantly influenced by the feedback from the presence of a massive star cluster.

To perform these simulations, various modules within the FLASH code are utilized and/or modified to accurately capture the relevant physical processes. A detailed description of each module is provided below.

3.1 Clouds Module Setup

The CLOUDS setup, originally developed by Šimon Blaha and Richard Wünsch (private communication), creates an ambient medium with known physical conditions such as density, temperature, velocity components, and pressure. On top of that, the code adds an arbitrary number of clouds/clumps with a Plummer density profile (Plummer, 1911) and user-defined physical conditions. Furthermore, each individual cloud is characterized by the presence of turbulent motions (see subsection 3.1.1). Additionally, we have modified the CLOUDS setup to include a much larger number of clouds, and to set a dust-to-gas mass ratio in the ambient and clumpy media, so that it works in tandem with the CINDER module (see Section 3.3 below).

3.1.1 Turbulence

Turbulence is an essential component of the CLOUDS module. Turbulence refers to the chaotic, random motions of gas within these clouds/clumps. The presence of turbulence helps to regulate the rate of mass accretion onto forming stars, preventing excessive accretion (see Section 3.5 below). Additionally, turbulence heavily influences the morphology and density structure of the clouds/clumps, affecting the distribution of gas and dust and shaping the subsequent star formation process.

Turbulent motions are generated for each clump by creating a 3D array of random amplitudes scaled down to the radius of the respective clump, R_{cl} :

$$v_x = v_x + A_{sin,x} \sin\left(\frac{\pi k_x}{R_{cl}}\right) + A_{cos,x} \cos\left(\frac{\pi k_x}{R_{cl}}\right) \quad (3.1.1)$$

$$v_y = v_y + A_{sin,y} \sin\left(\frac{\pi k_x}{R_{cl}}\right) + A_{cos,y} \cos\left(\frac{\pi k_x}{R_{cl}}\right) \quad (3.1.2)$$

$$v_z = v_z + A_{sin,z} \sin\left(\frac{\pi k_x}{R_{cl}}\right) + A_{cos,z} \cos\left(\frac{\pi k_x}{R_{cl}}\right), \quad (3.1.3)$$

where k_x is the total wave number with components m , n , and o in the x , y , and z directions, respectively. $A_{sin,x}$, $A_{sin,y}$, and $A_{sin,z}$ terms are the amplitudes of the sine

components in the x , y , and z directions, respectively. The $A_{\cos,x}$, $A_{\cos,y}$, and $A_{\cos,z}$ terms are the amplitudes of the cosine components in the x , y , and z directions, respectively. Finally, v_x , v_y , and v_z refer to the turbulent velocities in the x , y , and z directions, respectively, and can be scaled arbitrarily by multiplying to v_{turb} :

$$v_x = v_x \times v_{turb} \quad (3.1.4)$$

$$v_y = v_y \times v_{turb} \quad (3.1.5)$$

$$v_z = v_z \times v_{turb}. \quad (3.1.6)$$

The wave numbers are limited by the maximum value of N_{Turb} . The kinetic energy spectra is taken in the form $E(k_x) \propto k_x x^\alpha$, with wave numbers k_x between $2 \times 2\pi/R_{cl}$ and $32 \times 2\pi/R_{cl}$, and $\alpha = -5/3$.

3.2 Cool Module

The cooling function developed by Schure et al. (2009) has been incorporated into the FLASH code by Richard Wünsch (Wünsch et al., 2017). This function incorporates various mechanisms, such as collisional excitation, recombination, and line emission, to determine the rate at which the gas cools down.

To accurately model the cooling processes, a subcycling implementation is employed (Wünsch et al., 2008a), which involves checking the cooling rate at each iteration and adjusting the internal energy with smaller timesteps when the hydrodynamical timestep is insufficient to capture the cooling time. This approach allows for precise calculations of the cooling rate, ensuring that the thermodynamical evolution of the system is accurately captured in the simulations.

3.3 Cinder Module

The CINDER module (Cooling INduced by Dust and Erosion Rates), created by Martínez-González et al. (2018, 2019a, 2022), was compiled in to perform the FLASH

simulations. With the incorporation of CINDER, the precise tracking of the local dust-to-gas mass ratio in complex, multi-dimensional hydrodynamical simulations can be achieved. The stochastic injection of dust grains by supernovae, as well as the intricate effects of ionic collisions and electronic collisions, is accurately captured. These processes, namely thermal sputtering, dust grain growth, and dust-induced radiative cooling, have a profound impact on the abundance and size distribution of the grains.

To initialize the grain sizes, a log-normal grain size distribution was implemented, spanning from a minimum size of 1 nm to a maximum size of $0.5 \mu\text{m}$. Each bin is characterized by a representative value, determined using the lower and upper limits of the respective size bin, which are computed based on the overall range of grain sizes.

CINDER considers the size-dependent decrease in grain mass by ionic collisions that may remove individual atoms from the grains' surfaces, and the decrease in grain mass by sticking collisions with neutral atoms and molecules. Therefore, the local dust-to-gas mass ratio of each size bin is updated accordingly. Additionally, the total dust mass is evenly divided between silicate and graphite grains, with respective grain densities of 3.3 g cm^{-3} and 2.26 g cm^{-3} , to accurately account for their distinct properties in the simulations.

Furthermore, the dust-induced radiative cooling is accounted for by summing up the contributions from individual grain size bins. This is done by calculating the cooling rate resulting from gas-grain collisions, taking into consideration the densities of gas and dust, gas temperature, and the heating efficiencies associated with impinging electrons and nuclei. CINDER is able to perform these operations “on-the-fly” in multi-dimensional hydrodynamical simulations.

CINDER has been extensively tested through 3D hydrodynamical simulations that were conducted to investigate the interaction between supernova remnants and the shocked winds of neighboring massive stars within young massive stellar clusters. These simulations, carried out by Martínez-González et al. (2018, 2019a, 2022), provide valuable insights into the survival and behavior of supernova-condensed dust grains, and have a large impact on the gas thermodynamics.

3.4 Wind Module

Utilizing the WIND Module (Wünsch et al., 2017), the collective wind generated by a coeval young massive stellar cluster located at the simulation center can be incorporated based on the mass and energy deposition rates per unit volume described in Equation 2.1.6 and Equation 2.1.5. The distribution of star cluster mass follows a Schuster stellar density profile (see equation 2.1.4), where the core radius is R_c and the star cluster surface radius is R_{sc} (Silich et al., 2004) are chosen as 0.5 pc and 1 pc, respectively, with an index of $\beta=1.5$ (Palouš et al., 2013; Martínez-González et al., 2016, 2017).

To track the evolution of various properties of the star cluster wind, such as its mechanical output, mass-loss rate, and terminal speed, the BOOST stellar model grids and the SYNSTARS stellar population synthesis code are employed (Szécsi et al., 2020; Franeck et al., 2021). Specifically, a Kroupa initial stellar mass function (IMF) is assumed within the mass interval of $[0.01-120] M_\odot$, and a stellar grid with a metallicity of 0.4, Z_\odot (Szécsi et al., 2015).

As a summary, the WIND Module performs time-dependent source smoothing by interpolating time-dependent parameters. These parameters are read from a dafile generated from the SYNSTARS output. These parameters control the stellar density profile, the wind properties, and energy deposition over time. Next, the code determines the duration for which energy and mass are inserted, adjusting the duration if a split time-step is used. The WIND Module then iterates over each cell and keeps track of the total mass and energy insertion rates for the entire simulation. Finally, the code calculates the new density, modifies the velocity components to conserve momentum, updates the internal energy to conserve total energy, and calculates the new total energy, so the three conservation laws, described in Equation 2.1.1 - Equation 2.1.3, are ensured.

The WIND Module can also insert an arbitrary number of supernova explosions given their ejecta density ($\rho_{ej,SN}$) and velocity (v) distributions as functions of radius (r), their coordinates, as well as the value of the ejecta-condensed dust mass. The ejecta density is determined by the mass ($M_{ej,SN}$) and follows (Tenorio-Tagle & Boden-

heimer, 1988; Tang & Chevalier, 2017):

$$\rho_{\text{ej,SN}}(r) = \frac{M_{\text{ej,SN}}}{R_{\text{ej,SN}}^3} \left(\frac{r}{R_{\text{ej,SN}}} \right)^{-n}, \quad (3.4.1)$$

where n is the power-law index characterizing the density profile. The velocity has two parts: a linear expansion within the insertion radius ($R_{\text{ej,SN}}$) and zero beyond that. The maximum expansion velocity ($v_{\text{ej,SN}}$) is related to the power-law index (n) and the ratio of core to ejecta radius ($w_{\text{core,SN}}$) as:

$$v_{\text{ej,SN}} = \left[2w_{\text{core,SN}}^{-2} \left(\frac{5-n}{3-n} \right) \left(\frac{w_{\text{core,SN}}^{n-3} - n/3}{w_{\text{core,SN}}^{n-5} - n/5} \right) \frac{E_{\text{k,SN}}}{M_{\text{ej,SN}}} \right]^{1/2}. \quad (3.4.2)$$

The input parameters $E_{\text{k,SN}}$, $v_{\text{ej,SN}}$, and $M_{\text{ej,SN}}$ are related through:

$$E_{\text{k,SN}} = \frac{1}{2} M_{\text{ej,SN}} v_{\text{ej,SN}}^2. \quad (3.4.3)$$

The insertion radius is constrained by the simulation resolution. To minimize its impact, one has to ensure that the region overwritten by each supernova is as small as possible, yet large enough to preserve the spherical shape. In general terms, the supernova should be inserted encompassing at least four grid cells.

3.5 Sinks Module

When the mass of cold gas exceeds the Jeans mass, it can collapse under its own gravity. To address this, we employ the sink particles module of FLASH (Federrath et al., 2010). Sink particles are generated when the gas density surpasses a threshold (ρ_{sink}) within a given grid cell, and specific conditions are met within the accretion radius (r_{acc}). These conditions require the cells to be located at the highest refinement level and represent local minima of the gravitational potential, obtained from the solution of the Poisson equation. Moreover, the mass within these cells must exceed the Jeans mass, the gas flow should converge towards the cell, and the gas should be gravitationally bound. Additionally, the region occupied by the cell should not overlap

with any existing sink particle in the simulation. Gas that fulfills these conditions is incorporated into the sink particle. Commonly employed values for ρ_{sink} and r_{acc} are $10^{-17} \text{ g cm}^{-3}$ and 0.05 pc, respectively. Sink particles represent clusters of secondary stellar generations rather than individual stars. They interact with surrounding gas through gravity and accretion, and their properties, such as mass and position, are tracked throughout the simulation. The number of sink particles varies with simulation resolution, while the total mass in sink particles remains independent of the resolution (Wünsch et al., 2017).

3.6 Gravity Module

The GRAVITY Module is a component of the tree-solver algorithm that specializes in calculating gravitational potential and accelerations of an arbitrary mass distribution. In the GRAVITY Module, the tree-solver algorithm (Wünsch et al., 2018) is employed to efficiently perform these calculations. The tree-solver allows for the construction of a comprehensive (hierarchical) tree structure, facilitates communication between processors, and enables the accurate computation of gravitational forces. It employs a tree-walk algorithm to traverse the tree. Therefore, it is ideal in the present approach to account for the potentials of the clouds/clumps, the star cluster and sink particles, while keeping a relatively fast computation.

Simulation analysis

The objective is devoted to identify the necessary conditions within an active star-forming region that would facilitate a secondary phase of star cluster formation in NGC 1569-A. This region is composed of two objects, namely A1 and A2 (De Marchi et al., 1997), with ages of 7 Myr and 4 Myr, respectively (Álvarez Cruz, 2022).

The implemented simulations aim to create an environment where the super-wind generated by a primary massive star cluster (particularly the population of Red Supergiants in the A1 region), does not expel the gas necessary to induce the formation of a secondary massive star cluster (currently characterized by a population of W-R (Wolf-Rayet) and O-type stars of 4 Myr in the A2 region). One important constraint is that these two objects are separated by a distance of approximately ~ 3 pc (Hernández Prado, 2022), as illustrated in Figure 4.1.

In order to achieve this, we need to carefully examine the interplay between the super-wind from the primary star cluster and the surrounding gas allowing to proceed with a secondary phase of star formation in a violent environment.

4.1 Clouds Setup

As mentioned in section 3.1, it is possible to create an environment consisting of an arbitrary number of clouds, each possessing distinct characteristics such as density, temperature, radius, position, angular velocity, translation velocity, and dust-to-gas mass ratio.

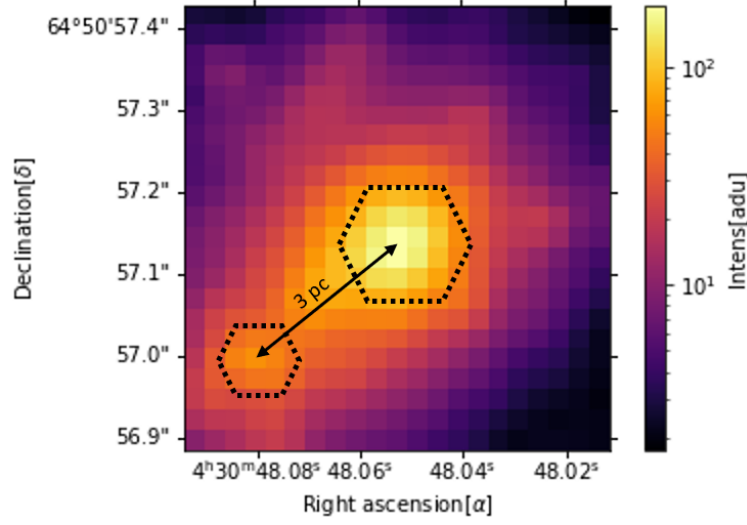


Figure 4.1: NGC 1569-A. The marked zones correspond to the A1 and A2 clusters, with the first in the center and the second in the outer region. Figure adopted from Hernández Prado (2022).

The density of each cloud follows a Plummer-Schuster profile:

$$\rho = \frac{\rho_{cl}}{\left(1 + \left(\frac{r}{r_p}\right)^2\right)^\beta} \quad (4.1.1)$$

where

$$r_p = 0.9 * R_{cl} \quad (4.1.2)$$

where R_{cl} and ρ_{cl} is the radii and central density from each cloud, β is the steepness in the distribution, and r_p the characteristic radii for the distribution.

Furthermore, in all cases, the ambient medium is characterized by constant density, temperature, and dust-to-gas mass ratio. These values are as follows: $\rho_{amb} = 10^{-24} \text{ g cm}^{-3}$, $T_{amb} = 10^4 \text{ K}$, and $Z_d = 10^{-2}$.

To establish the appropriate model, multiple iterations were conducted to determine a viable arrangement of clouds and their respective parameters, also the overall number of clouds required.

After conducting over fifty iterations, two main scenarios emerged as the most promi-

nent: the clumpy case and the cloud-cloud interaction scenario.

4.1.1 Clumpy-case

The modeling process began with a minimal number of clouds, initially consisting of only two clouds representing A1 and A2. This configuration is referred to as the "two-clouds" model. The initial characteristics of the assumed clouds are listed in Table 4.1, while the simulation parameters are provided in Table 4.2.

Initial Cloud Parameters		
	Cloud 1 (A1)	Cloud 2 (A2)
T_{cl}	2.73 K	2.73 K
R_{cl}	2 pc	3 pc
n_{cl}	$1.8 \times 10^4 \text{ cm}^{-3}$	$1.8 \times 10^5 \text{ cm}^{-3}$
M_{cl}	$9.2 \times 10^3 M_{\odot}$	$3.1 \times 10^5 M_{\odot}$

Table 4.1: Initial Cloud Parameters for the "two-clouds" case.

Simulation parameters	
Box side	16 pc
Refinement level	5
Resolution	0.125 pc

Table 4.2: Simulation parameters for the "two-clouds" case.

Figure 4.2 to Figure 4.5 depict the hydrodynamical evolution of properties such as column density, temperature, and radial velocity in the 'two-clouds' model. In the initial stages, we observe the progression of the star cluster wind within the simulation box, which eventually reaches the outer boundaries of the secondary cloud after approximately 26 kyr.

The powerful star cluster wind crushes and mass-loads the stripped cloud material, and sweeping it away. Around $t = 60$ kyr into the simulation, the hot gas from the wind is nearly filling the entire box, except for a remaining fraction of secondary cloud. However, disruption and sweeping of the secondary cloud is completed after only ~ 130 kyr.

The rapid disruption of the secondary cloud due the powerful super-wind marks the way to the **clumpy-case**, where multiple clouds within the region are introduced.

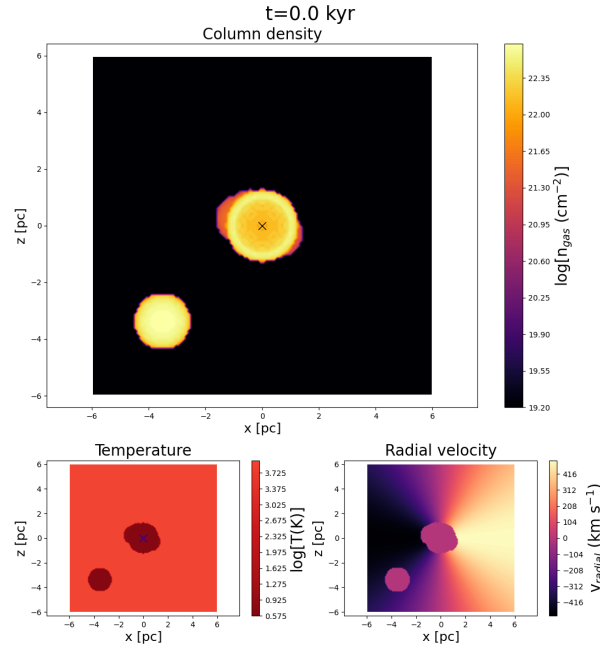


Figure 4.2: Column density, temperature and radial velocity panels are shown at $t = 0.0$ kyr for the "two-cloud" model.

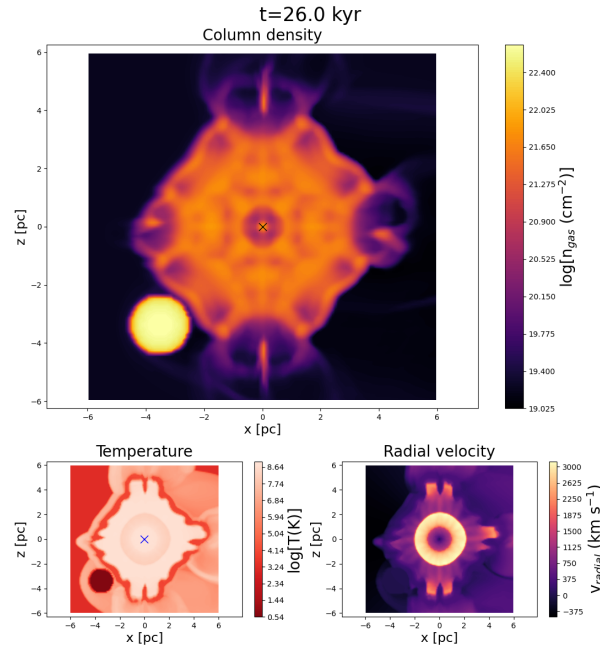


Figure 4.3: Column density, temperature and radial velocity panels are shown at $t = 26$ kyr for the "two-cloud" model.

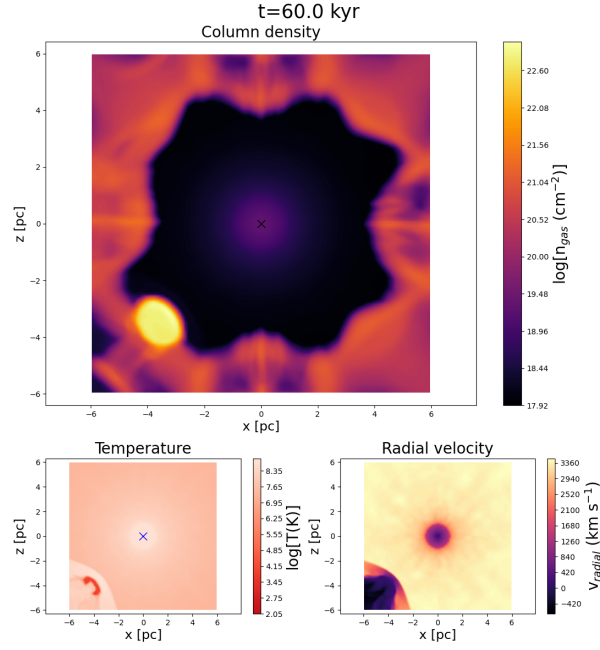


Figure 4.4: Column density, temperature and radial velocity panels are shown at $t = 60$ kyr for the "two-cloud" model.

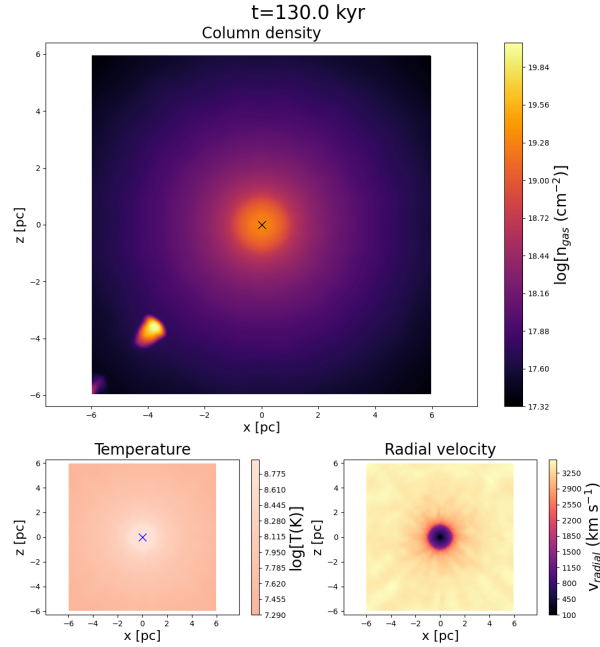


Figure 4.5: Column density, temperature and radial velocity panels are shown at $t = 130$ kyr for the "two-cloud" model.

This model is inspired by the the presence of multiple groups of stars in the extended region around the SSC-A region, as observed in the HST data (refer to Figure 4.6).

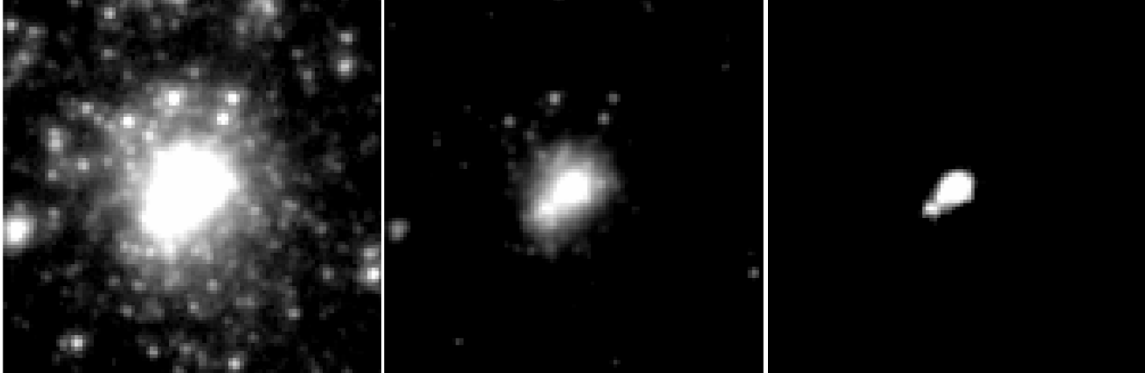


Figure 4.6: Contrast sequence from HST data, figure adapted from Hernández Prado (2022).

The key features of the **clumpy-case** are characterized by two distinct overdensities. The first one is located at the center of the simulation, while the second one is approximately 4 pc away from the center, both in the $y=0$ and $z=0$ planes. The location of each cloud are modeled using a normal distribution in all planes, with a specific dispersion in their respective planes, simulating the presence of multiple gas and stellar overdensities in this region.

The parameters are also subject to specific distributions, and to mitigate global collapse in each cloud, turbulence is introduced (see Table 4.3). The simulation parameters are the same as in the "two-clouds" case (see Table 4.2).

Initial Cloud Parameters		
Parameter	Mean	Deviation
T_{cl}	10 K	15 K
R_{cl}	0.6 pc	0.2 pc
n_{cl}	$5 \times 10^5 \text{ cm}^{-3}$	$5 \times 10^5 \text{ cm}^{-3}$
$v_{x,y,z}$	1 km s^{-1}	10 km s^{-1}
v_{turb}	3 km s^{-1}	

Table 4.3: Initial Cloud Parameters for the clumpy case.

In Figure 4.7, the distribution of density, temperature, radius, and mass values for

each cloud is displayed in their respective locations, specifically in the x-y plane with $z = 0$.

It is important to note that there is a central cloud located at the center of the box, representing the primary cloud. This cloud stands out for its larger size and mass compared to the other clouds. Additionally, it features a hole in its structure, imposed to represent that the gas in the cloud's central region has been converted into the primary star cluster. It is from this central cloud/cluster that the super-wind is launched.

The number of clouds, totaling 180, is determined based on the total mass requirement to achieve an initial condition of approximately $10^6 M_\odot$. This includes the primary cloud as well. This is necessary because the reported mass is $5.5 \times 10^5 M_\odot$, and the remaining mass is intended to be added to the super-wind as it expands and sweeps through the surrounding medium. A histogram of the distribution of mass for each cloud is presented in Figure 4.8.

4.1.2 Cloud-Cloud case

Habe & Ohta (1992) conducted 2-D simulations to study the impact of a head-on collision between different-sized clouds now referred to as the "Habe-Ohta model". They found that the larger cloud was disrupted by the resulting bow shock, which compressed the smaller cloud. This compression caused the gas within the smaller cloud to become gravitationally unstable. Similarly, Takahira et al. (2014) performed 3-D simulations using the Enzo hydrodynamical code. Their simulations involved two clouds with distinct masses separated by a distance of 1.2 pc. As the cooling processes have commenced, the cloud became unstable and prone to collapse without additional support. To prevent premature collapse due to cooling, turbulence support was introduced (see Figure 4.9).

The collision between the clouds resulted in the formation of a shocked gas region at the interface of their surfaces. Due to the size difference between the clouds, the shock front became oblique. In the absence of turbulence, the smaller cloud would experience compression driven by its own gravity. However, the introduction of turbulence caused the shock front to consist of filaments, triggering the development of thin shell

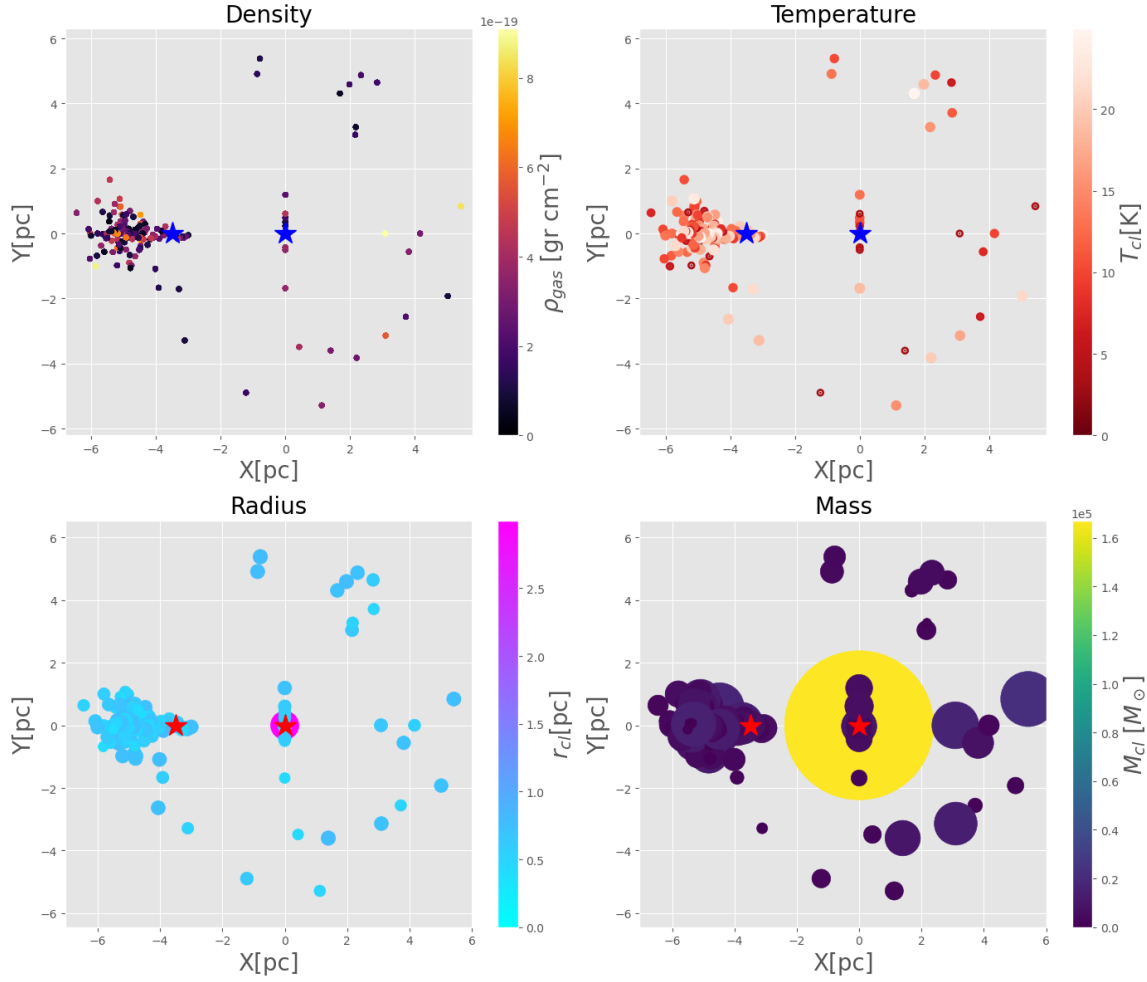


Figure 4.7: The density (top-left panel), temperature (top-right panel), radius (bottom-left panel), and mass (bottom-right panel) plots are presented for the clumpy case. Each cloud is shown in its respective location in the x-y plane with $z = 0$, along with its corresponding parameter values. The two star symbols indicate the location of A1 and A2 in each panel.

instabilities. These instabilities led to the formation of ripples that fragmented into cores. Higher collision velocities resulted in faster and more numerous core formation.

Massive star cluster formation triggered by cloud-cloud collisions is a well-known phenomenon observed in nearby interacting galaxies, which are often characterized by high-mass star-forming regions. Fukui et al. (2020) provides a comprehensive review of the progress made in understanding cloud-cloud collisions and their role in triggering

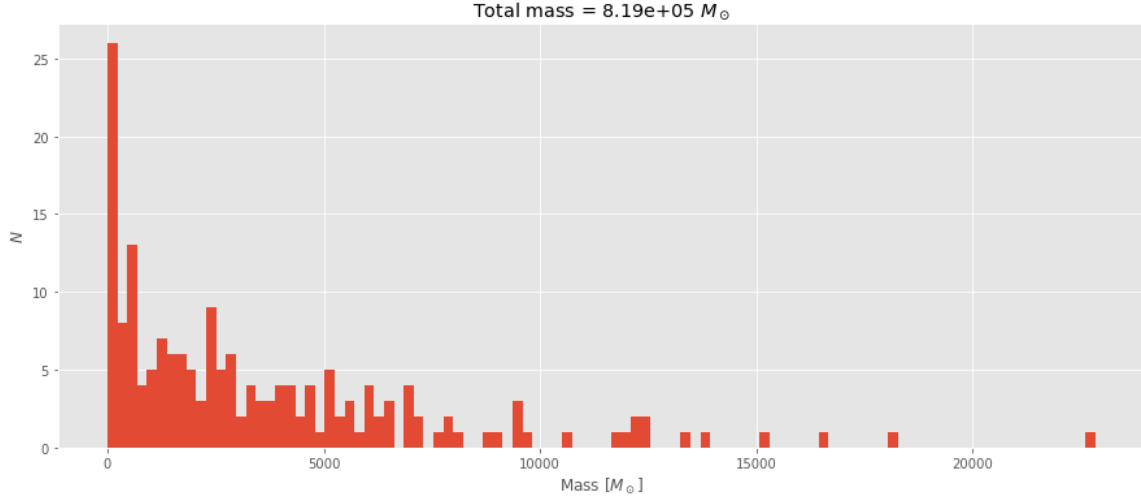


Figure 4.8: Histogram of the distribution of mass for each cloud in the clumpy case.

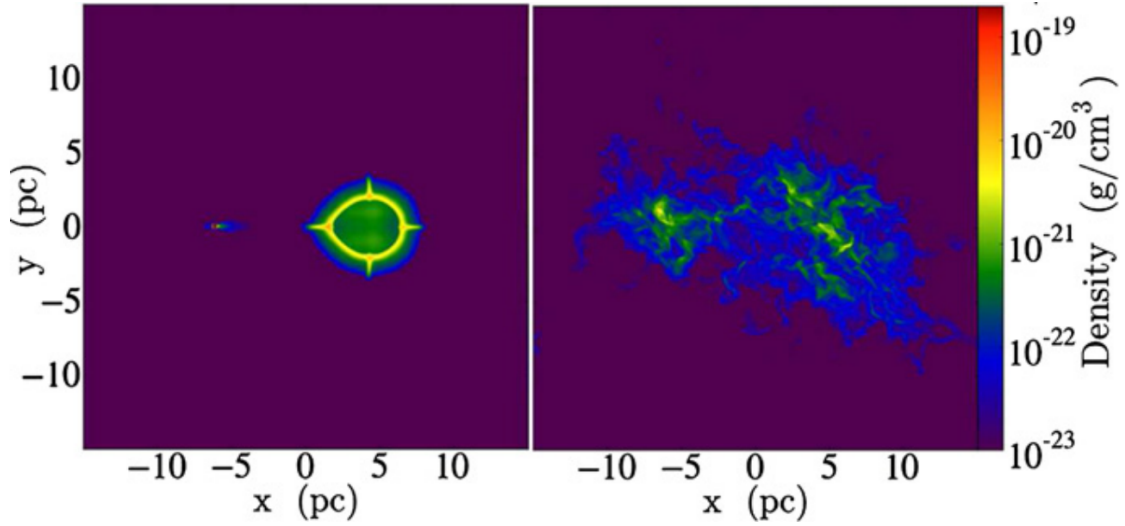


Figure 4.9: Density slice of two clouds after 5.31 Myr, for static simulations. The left panel shows the clouds with no initial turbulence while the right panel shows the outcome of adding an initial turbulent spectrum to both clouds. Figure adapted from Takahira et al. (2014)

star cluster formation.

The Habe-Ohta model, presented in Figure 4.10, illustrates the different stages of cloud-cloud collisions. In phase 1, a small cloud and a large cloud approach each

other. Upon collision, a compressed layer forms between the two clouds, resulting in the creation of a U-shaped cavity within the larger cloud (phase 2). As the collision progresses, the gas from both clouds flows into the compressed layer, leading to the complete merging of the smaller cloud into the compressed region (phase 3). Within the U-shaped cavity, the compressed layer exhibits high gas column density, which can give rise to the formation of dense cores and stars through gravitational instabilities.

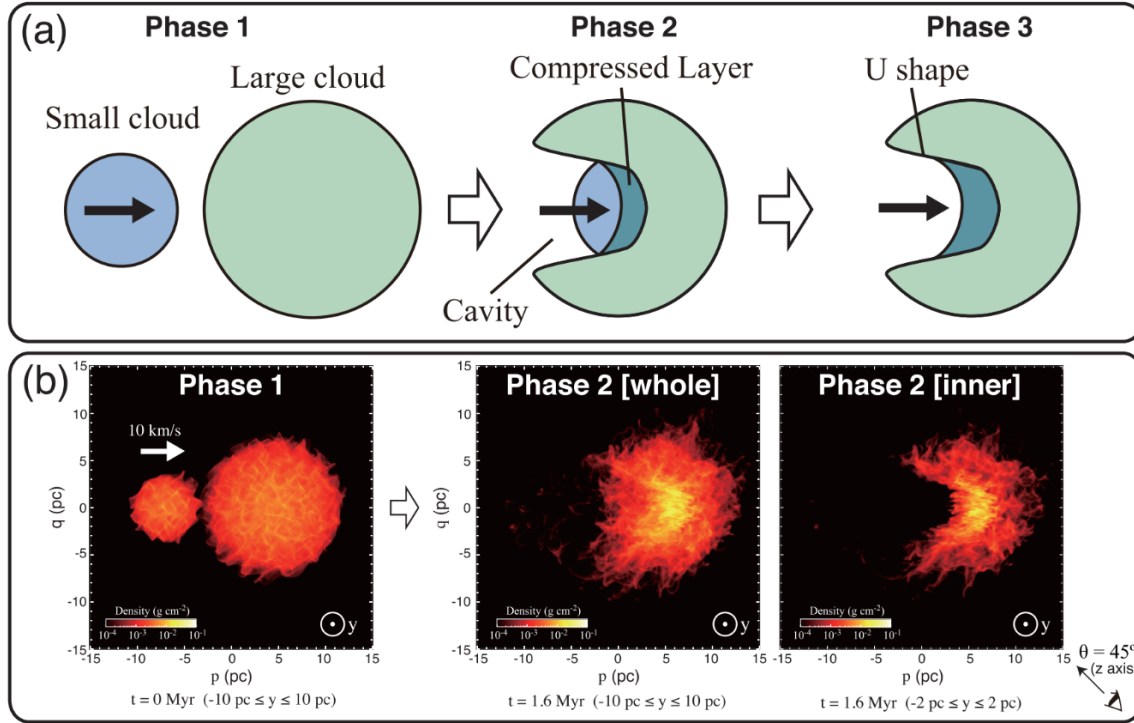


Figure 4.10: Top panel: schematic picture of three evolutionary epochs of the Habe-Ohta model of a cloud-cloud collision between two spherical clouds with different sizes. As the small cloud drives into the larger, a U-shaped cavity is created in the large cloud and the small streams into the compressed layer formed in the collision interface. Bottom panel: Surface density plots of a 10 km s^{-1} collision. Figure adapted from Fukui et al. (2020).

Observations have revealed that cloud-cloud collisions occur at highly supersonic speeds, typically around $v_{\text{col}} \simeq 10 \text{ km s}^{-1}$. This high velocity leads to strong shock compression, and due to the efficient radiative cooling in molecular clouds, a shock-compression ratio of approximately $r \simeq M_s^2$ is achieved. Here, M_s represents the Mach number, and for a collision velocity of around 10 km s^{-1} , the Mach number

is approximately ~ 50 . As a result, the density within the shock layer increases to $n = n_0 M_s^2 \sim 10^6 \text{ cm}^{-3}$, assuming an initial density of $n_0 = 10^3 \text{ cm}^{-3}$. However, it is important to note that the presence of a magnetic field can significantly influence the physical state of the shocked cloud (Fukui et al., 2020).

As the shock compression progresses, it gives rise to a dense gas sheet that is conducive to gravitational instabilities and subsequent star formation. Whitworth et al. (1994) estimated the timescale for gravitational instabilities to manifest and promote star growth as follows:

$$t_{\text{gi}} \simeq \left(\frac{c_s}{G \rho_1 v_{\text{col}}} \right)^{1/2} \quad (4.1.3)$$

here, c_s represents the sound speed, G is the gravitational constant, ρ_1 is the density of the pre-shocked gas, and v_{col} denotes the collision velocity.

If the line mass of a formed filament exceeds a critical value, it undergoes collapse and fragmentation, thereby triggering star formation within the region of contact.

This gives rise to the emergence of the **cloud-cloud case**, in which the primary cloud also exhibits a cavity at its center, representing the cluster that has already formed and consumed a significant amount of gas. The secondary cloud, on the other hand, is situated approximately 10 pc away from the center.

The parameters for the **cloud-cloud case** are provided in Table 4.4 and Table 4.5 for the input cloud parameters and simulation parameters, respectively. The input cloud parameters are illustrated in Figure 4.11.

In this particular scenario, the outer boundaries of each cloud are in close proximity to each other, almost touching. The secondary cloud exhibits a translational velocity of 30 km s^{-1} directed towards the central cloud, setting the stage for a cloud-cloud collision.

Initial Cloud Parameters		
	Cloud 1 (A1)	Cloud 2 (A2)
n_{cl}	$3.72 \times 10^5 \text{ cm}^{-3}$	$3.72 \times 10^5 \text{ cm}^{-3}$
r_{cl}	5 pc	5 pc
T_{cl}	2.73 K	2.73 K
v_{col}	0	30 km s^{-1}
v_{turb}	3 km s^{-1}	

Table 4.4: Initial Cloud Parameters for the cloud-cloud case.

Simulation parameters	
Box side (x - plane)	23 pc
Box side (y - plane)	16 pc
Box side (z - plane)	16 pc
Maximum refinement level	6
Minimum refinement level	5
Maximum resolution (x - plane)	0.08 pc
Minimum resolution (x - plane)	0.17 pc
Maximum resolution (y,z - plane)	0.06 pc
Minimum resolution (y,z - plane)	0.125 pc

Table 4.5: Simulation parameters for the cloud-cloud case.

4.2 Evolution of the Clumpy-Case

The initial conditions of the properties such as gas column density, surface density profile, thermal pressure, gas temperature, radial gas velocity and dust surface density at $t = 0$ are in Figure 4.12.

At $t = 0$, the initial condition is that the first star cluster is positioned at the center of its parent molecular cloud. Within the cloud's central region, marked by a cross symbol, there exists a cavity of lower gas density with the size of the star cluster. This cavity is intended to show the conversion of gas into stars during the first generation of star formation. By incorporating this initial condition, overcooling during the formation of the star cluster wind is inhibited. This cavity can be easily recognized in the thermal pressure panel. In the column density panel, the formation of sink particles, occurring in regions of high density (see section 3.5) is highlighted, displating their respective mass on the colorbar. The surface density profile is dis-

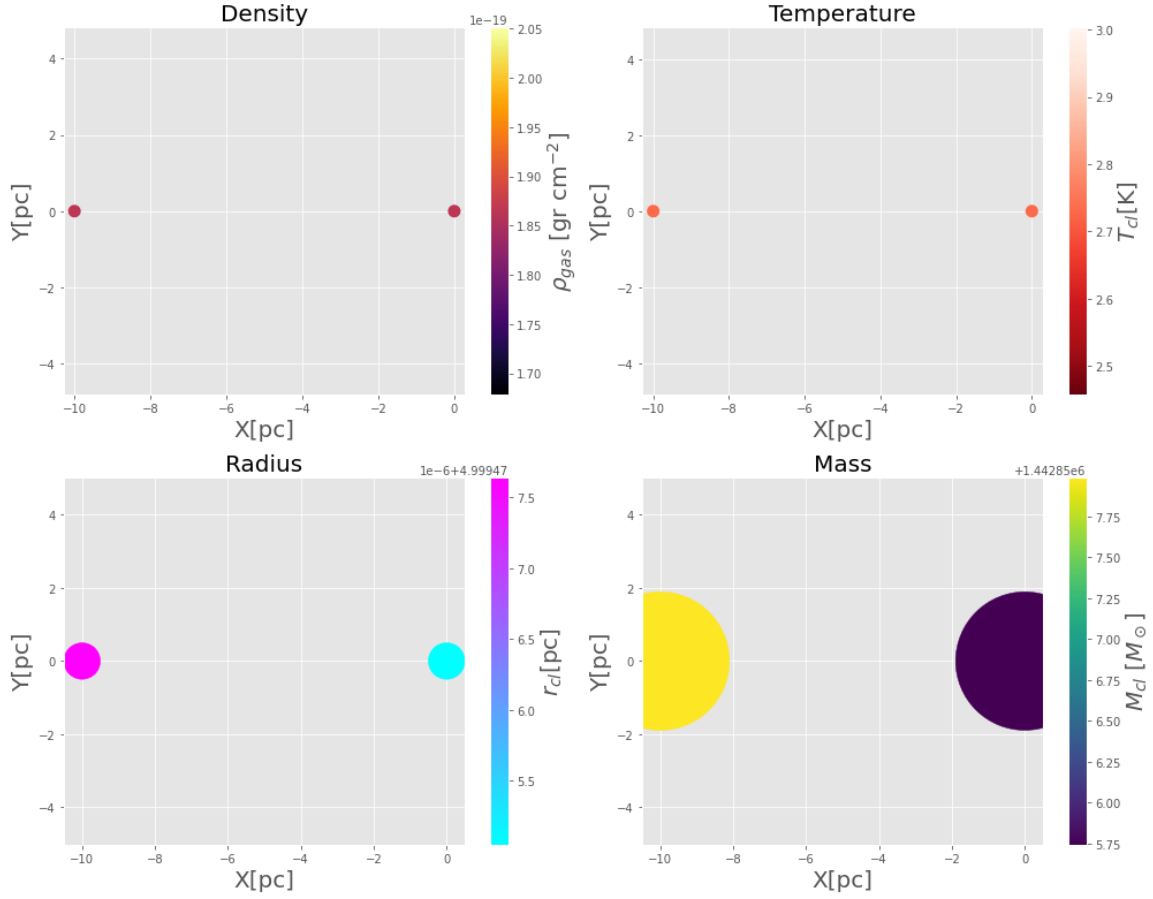


Figure 4.11: The density (top-left panel), temperature (top-right panel), radius (bottom-left panel), and mass (bottom-right panel) plots are presented for the cloud-cloud case. Each cloud is shown in its respective location in the x-y plane with $z = 0$, along with its corresponding parameter values. The two star symbols indicate the location of A1 and A2 in each panel.

played using the *task ellipse* method from **IRAF** (Jedrzejewski, 1987), which employs fixed concentric elliptical isophotes to integrate the density along the radial axis, in the profile it is recognizable that the density is distributed almost homogeneously until an over-density is reached at ~ 5 pc, causing a notorious bump in this profile. The temperature of the clouds is uniform and significantly lower than the ambient value of $T_{\text{amb}} = 10^4$ K, creating a strong contrast. The radial velocity panel displays a velocity field with a left-to-right direction and a scalar velocity of $v_{\text{amb}} = 500 \text{ km s}^{-1}$, representing from the influence of the SSC-B super-wind. Within the clouds, turbu-

lence is observed, countering self-collapse and promoting filament formation. Finally, similar to the column density, the dust surface density also reveals the presence of dusty molecular clouds.

For this simulation, the initial stages of evolution are crucial. Within the first thousand years displayed in Figure 4.13, the effect of the hot gas arising from the thermalization of kinetic energy from random collisions of stellar winds from single massive stars, forming a collective wind called super-wind, becomes evident in the temperature panel, reaching temperatures of approximately $\sim 10^9$ K. The influence of the super-wind from the SSC-B is felt throughout the entire simulation box, causing the surface of the clouds to heat up via ram pressure. However, at this point, the heating is not sufficient to initiate a swept-up process. Instead, the turbulence in the system has led to significant changes in pressure, especially noticeable in the smaller clouds, as seen in the pressure panel.

Approximately at 22 kyr, as displayed in Figure 4.14, turbulence has caused noticeable changes in the column density, leading to an increase in the concentration of gas and dust. At this stage, the hot gas from the super-wind is rapidly expanding, searching for an escape route, while the outer regions of the clouds are being heated and disturbed.

By ~ 53 kyr, as seen in Figure 4.15, the super-wind is nearly out from the central region, and the reverse shock has already formed, beginning to thermalize the free-wind region. This can be easily observed in the velocity panel, though it may be more difficult to see in the temperature panel.

At approximately 61 kyr, the hot gas from the super-wind has finally found a low-density region where it can escape. This is evident in the velocity panel, which shows the high velocity of the super-wind, as well as the presence of the reverse shock (see Figure 4.16).

By ~ 71 kyr, the hot gas has found at least three low-density zones through which it can escape from the center of the simulation. The velocity panels clearly show the main escape route. The formation of filaments is still occurring but, at this stage, no sink particles have been created (see Figure 4.17).

At approximately 85 kyr, the first sink particle is created (see Figure 4.18) near the

simulation center. However, the hot gas from the super-wind has nearly filled the entire simulation box at this stage, exerting its negative feedback on the star-forming region.

The second sink particle is created at ~ 97 kyr (see Figure 4.19), followed by the third one at 111 kyr (see Figure 4.20). As the simulation progresses, the hot gas from the super-wind continues to exert its influence, but despite this, a total of 6 sinks particles have been created by 155 kyr (see Figure 4.21).

At approximately 190.01 kyr (see Figure 4.22), the column density reveals two main over-dense regions located close to the center. These regions seem to be potential sites for the formation of a second generation of stars.

Throughout the simulation, the total mass of sinks particles does not reach $10^4 M_\odot$, as shown in Figure 4.23. Note that at a time ~ 160 kyr, a decrease in the total mass is seen, as one sink particles has moved out of the simulation box.

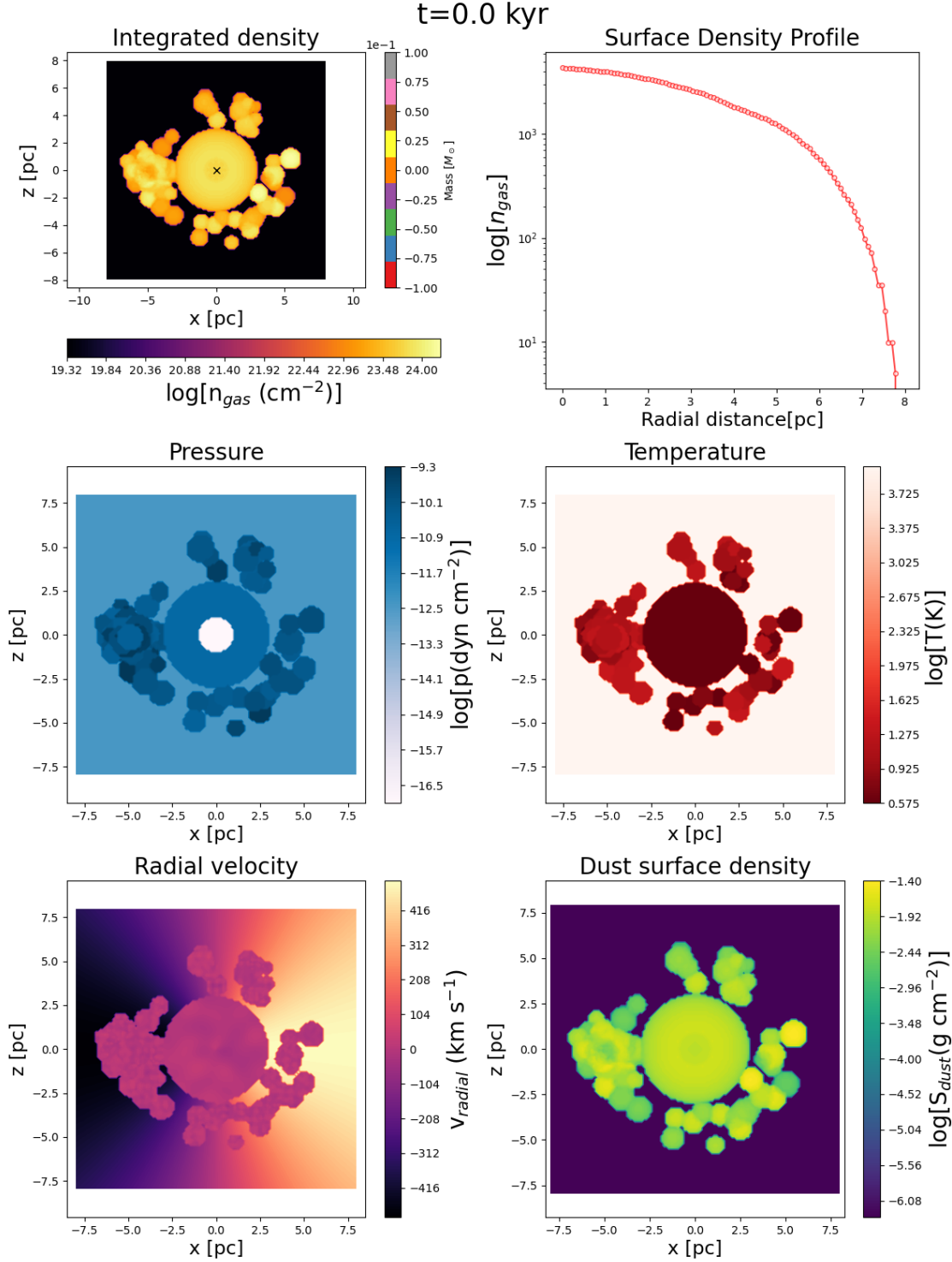
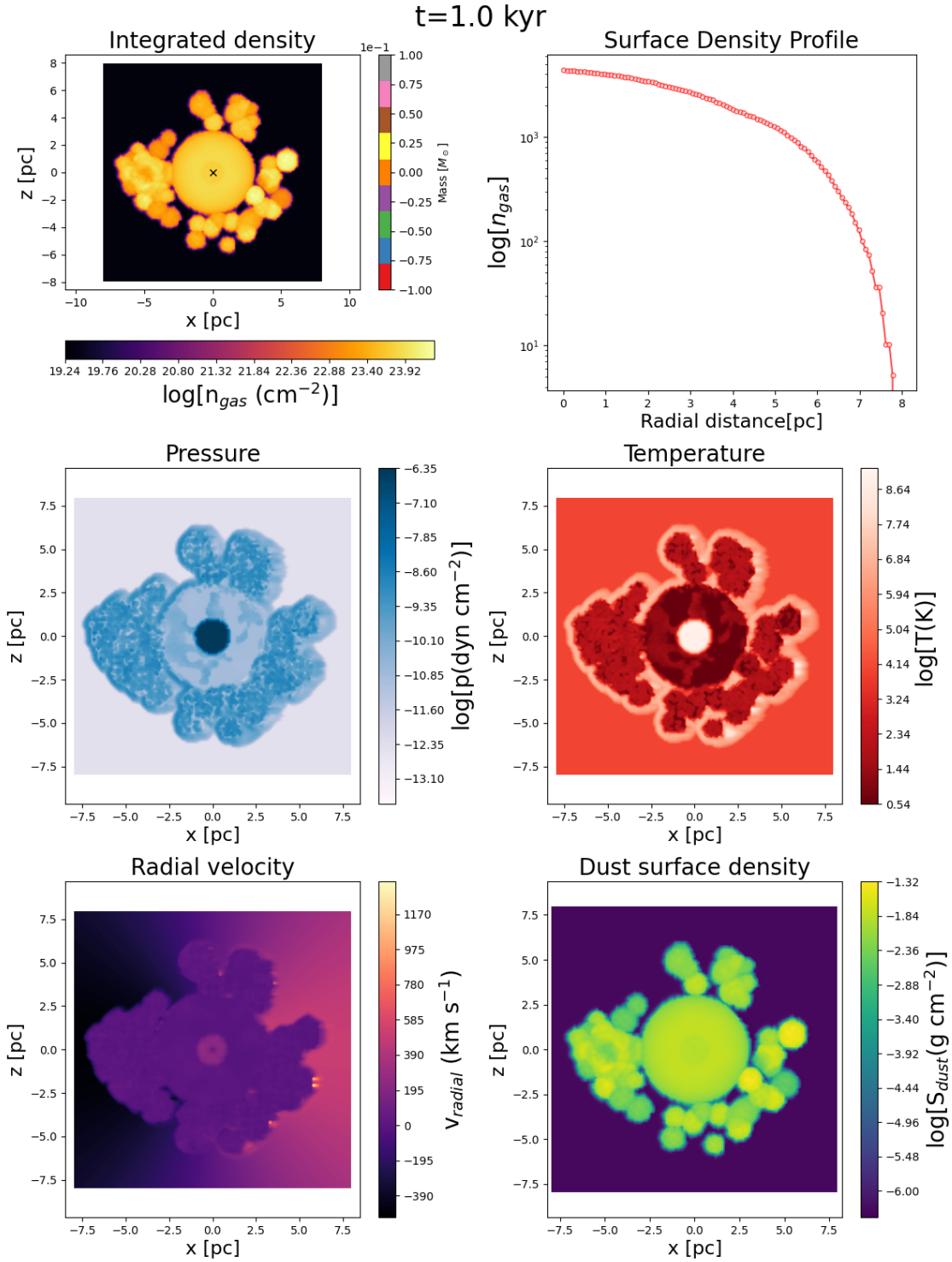


Figure 4.12: The plots display the column density (top-left), surface density profile (top-right), pressure (middle-left), temperature (middle-right), radial velocity (bottom-left), and dust surface density (bottom-right) at $t = 0$ kyr. Additionally, the center of the box, corresponding to the region of A1, is marked with a 'cross' symbol. The color of the dot symbols corresponds to the mass of the sink particle, which is indicated by the vertical qualitative colorbar.

Figure 4.13: Same as Figure 4.12, but at time $t = 1$ kyr.

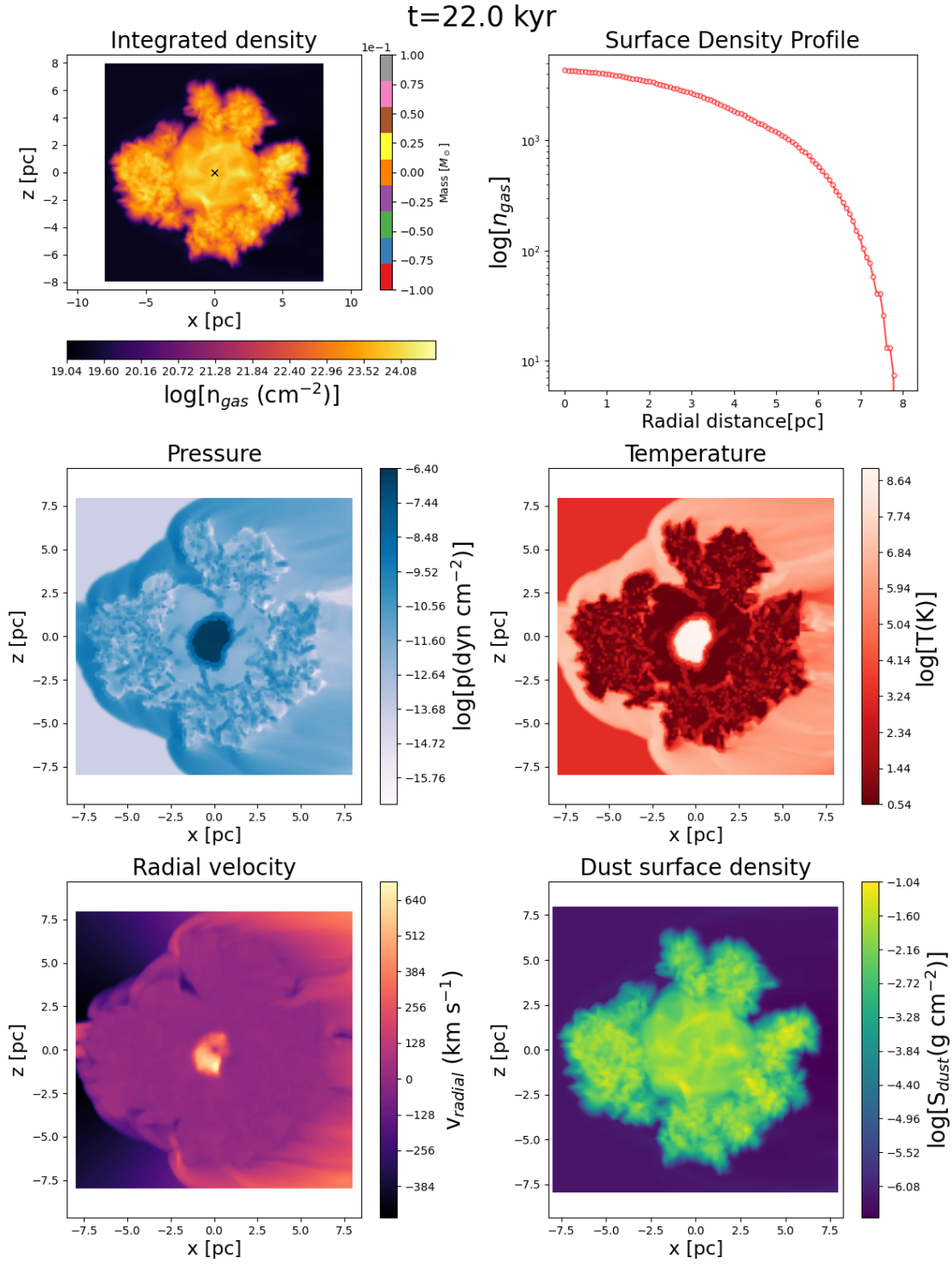
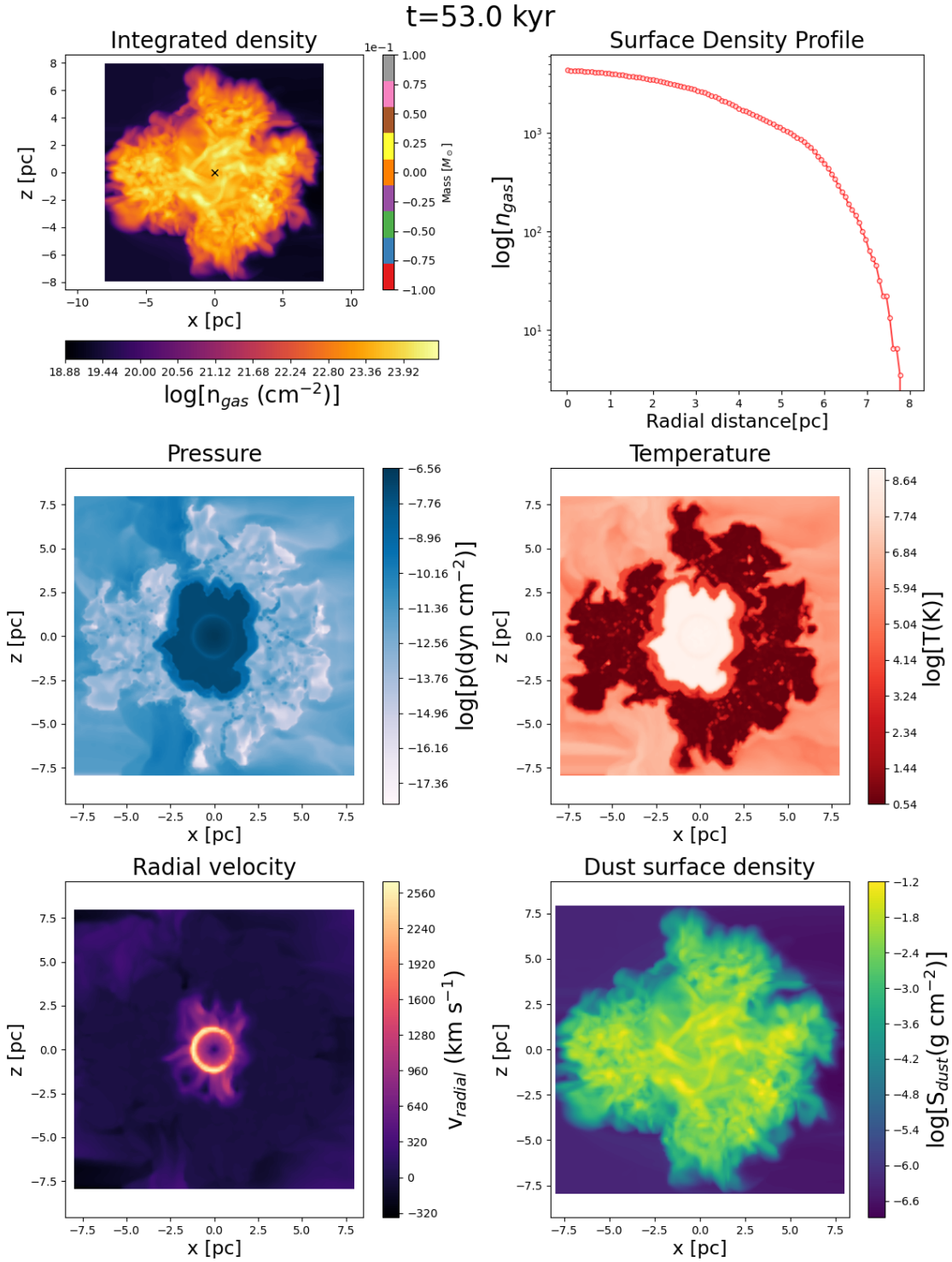


Figure 4.14: Same as Figure 4.12, but at time $t = 22$ kyr.

Figure 4.15: Same as Figure 4.12, but at time $t = 53$ kyr.

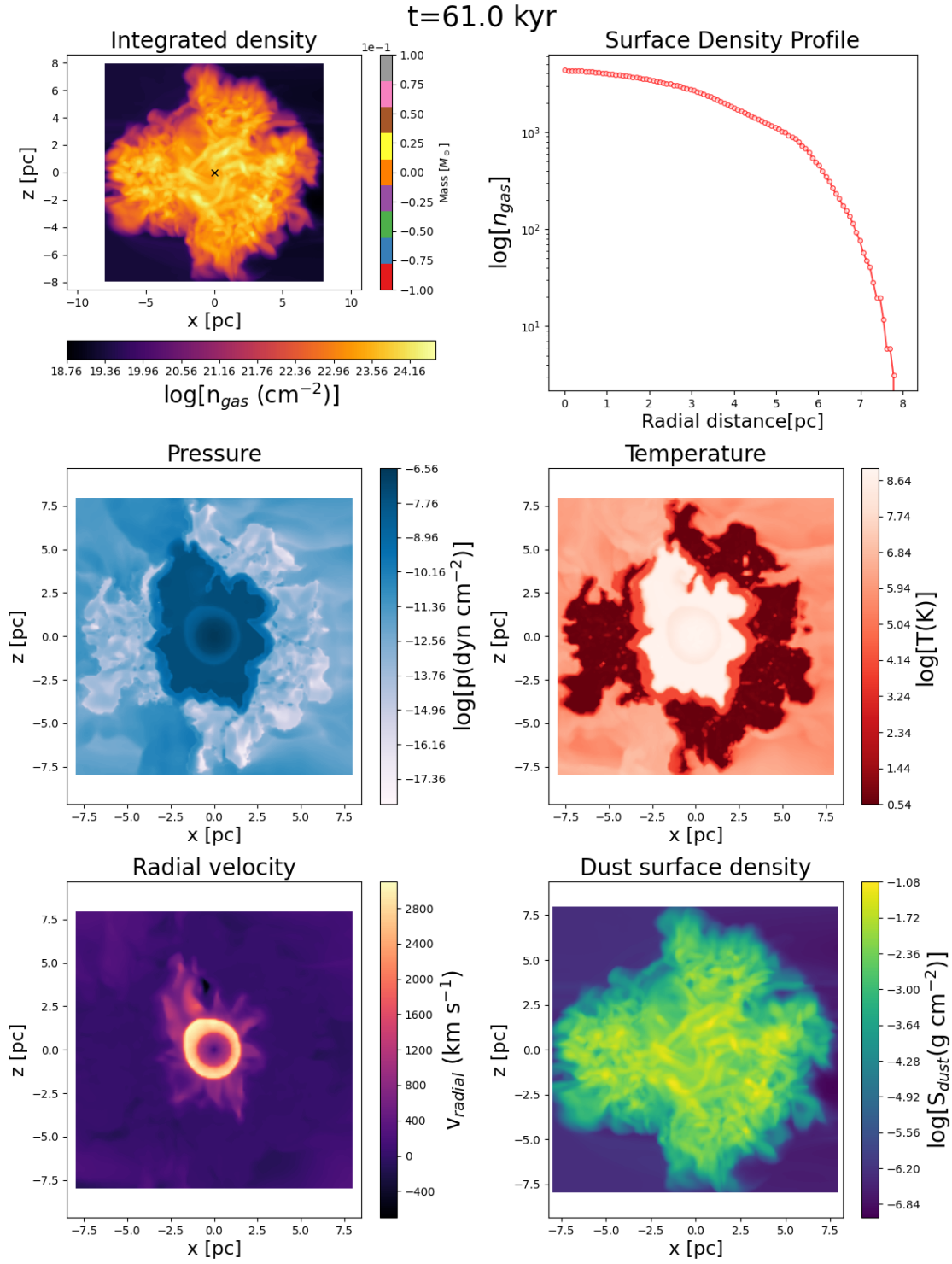
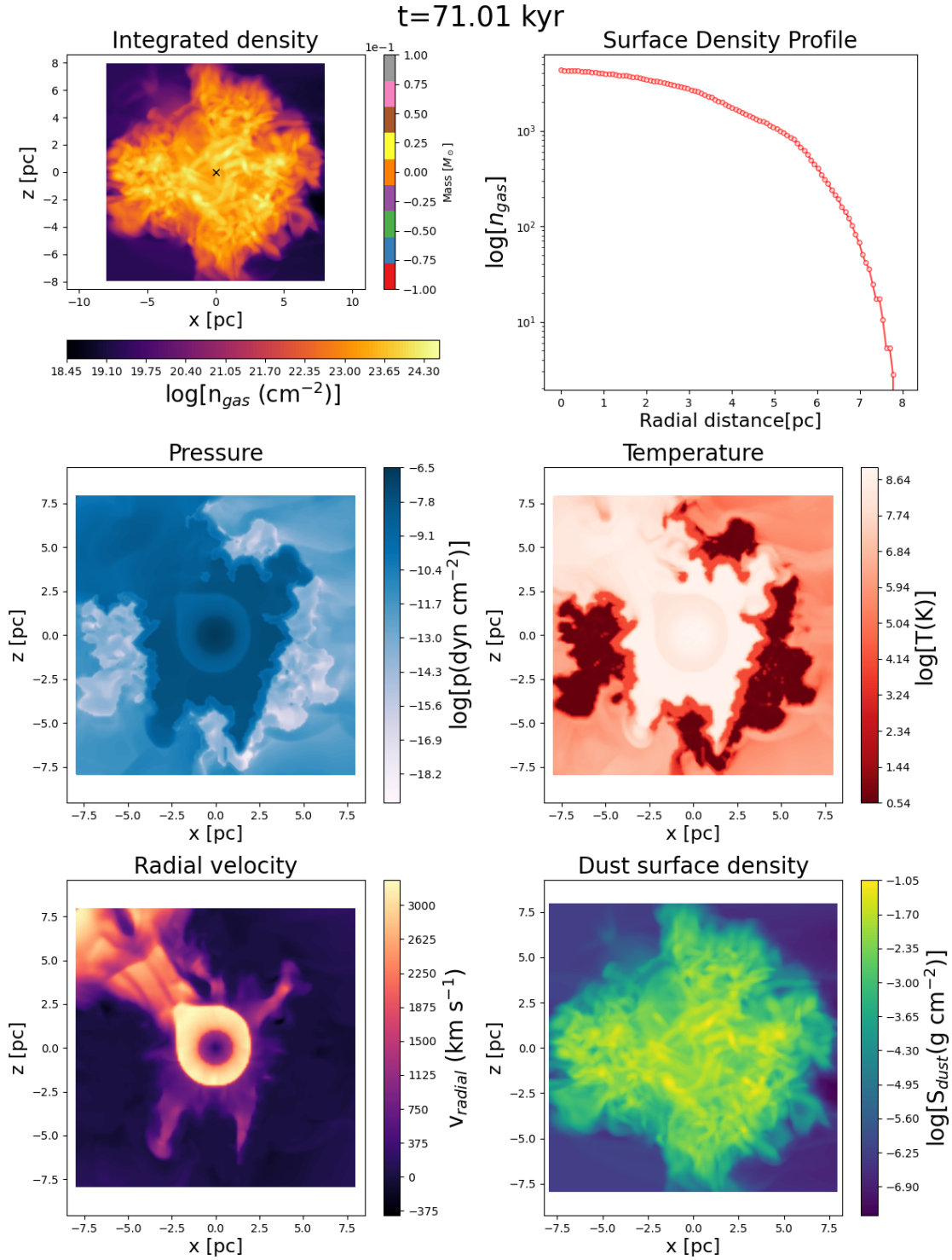


Figure 4.16: Same as Figure 4.12, but at time $t = 61$ kyr.

Figure 4.17: Same as Figure 4.12, but at time $t = 71 \text{ kyr}$.

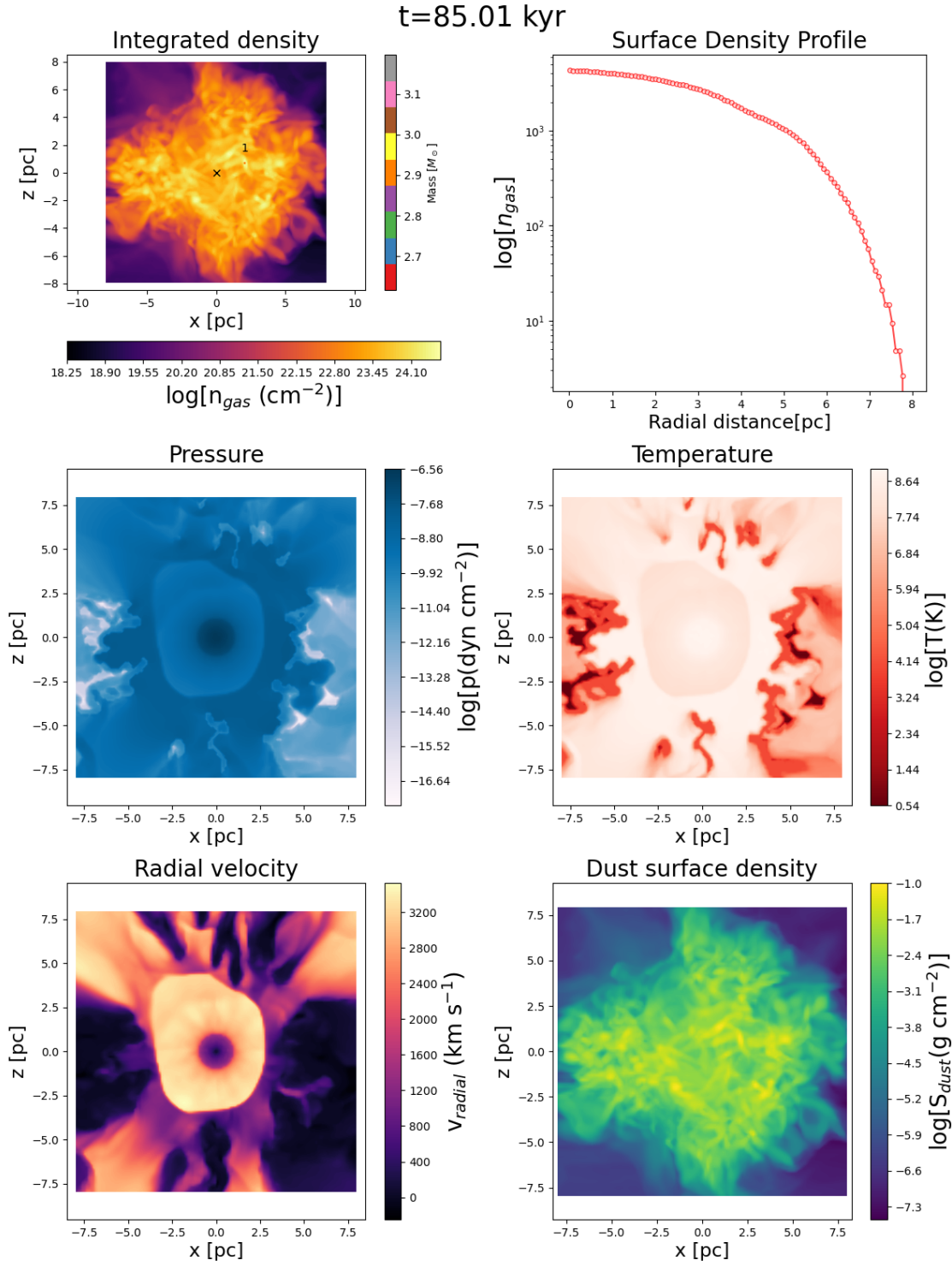
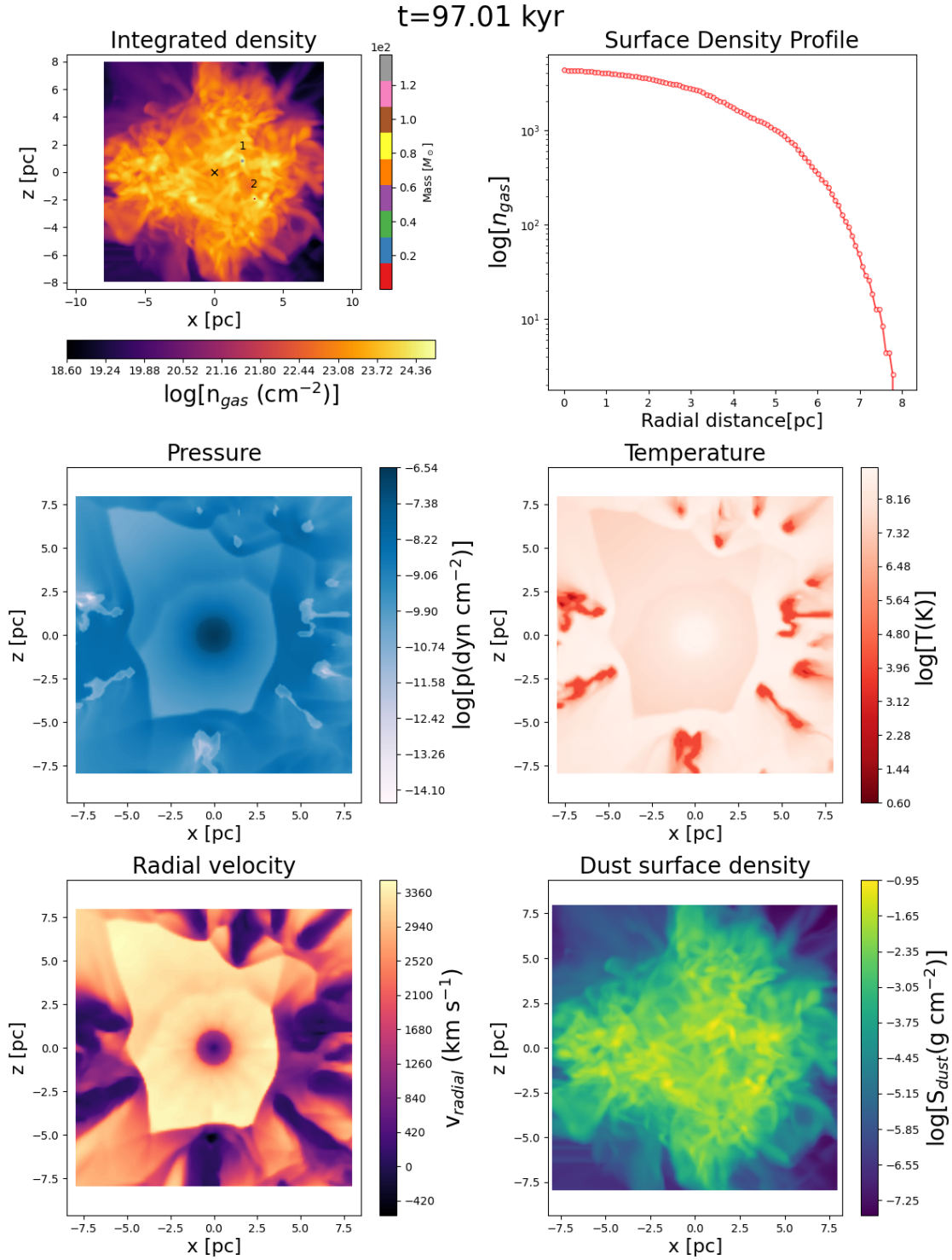


Figure 4.18: Same as Figure 4.12, but at time $t = 85 \text{ kyr}$.

Figure 4.19: Same as Figure 4.12, but at time $t = 97$ kyr.

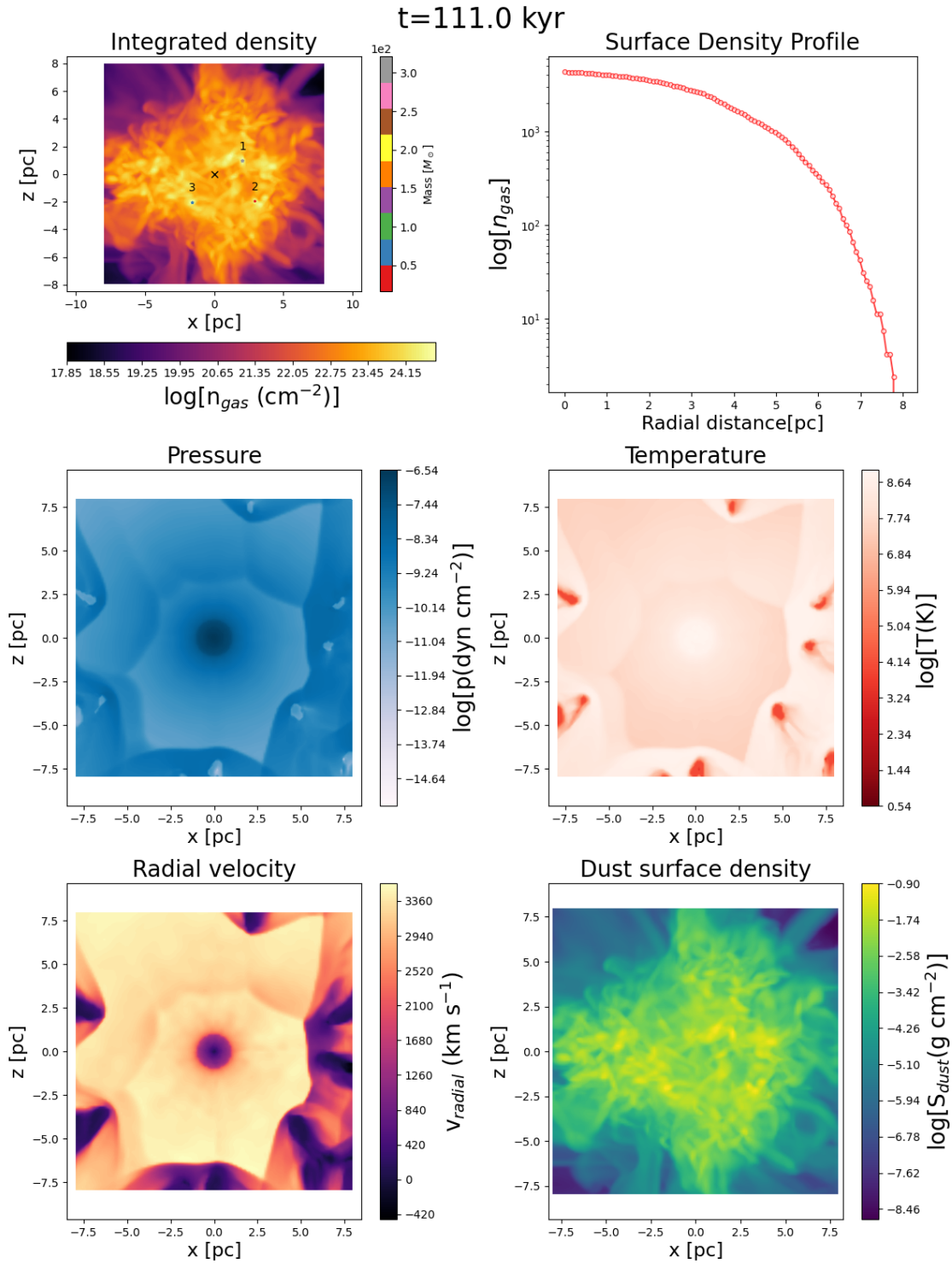
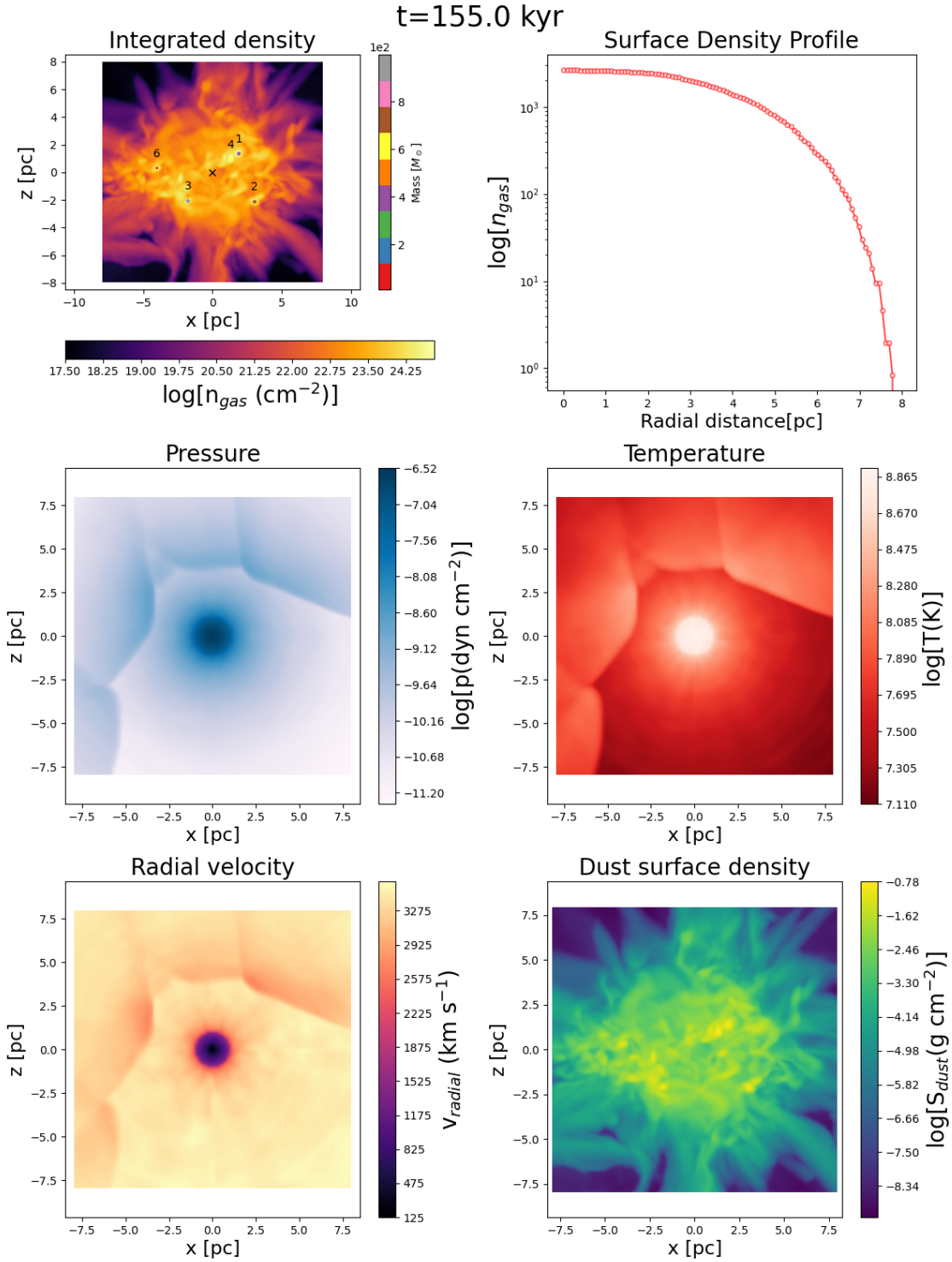


Figure 4.20: Same as Figure 4.12, but at time $t = 111$ kyr.

Figure 4.21: Same as Figure 4.12, but at time $t = 155$ kyr.

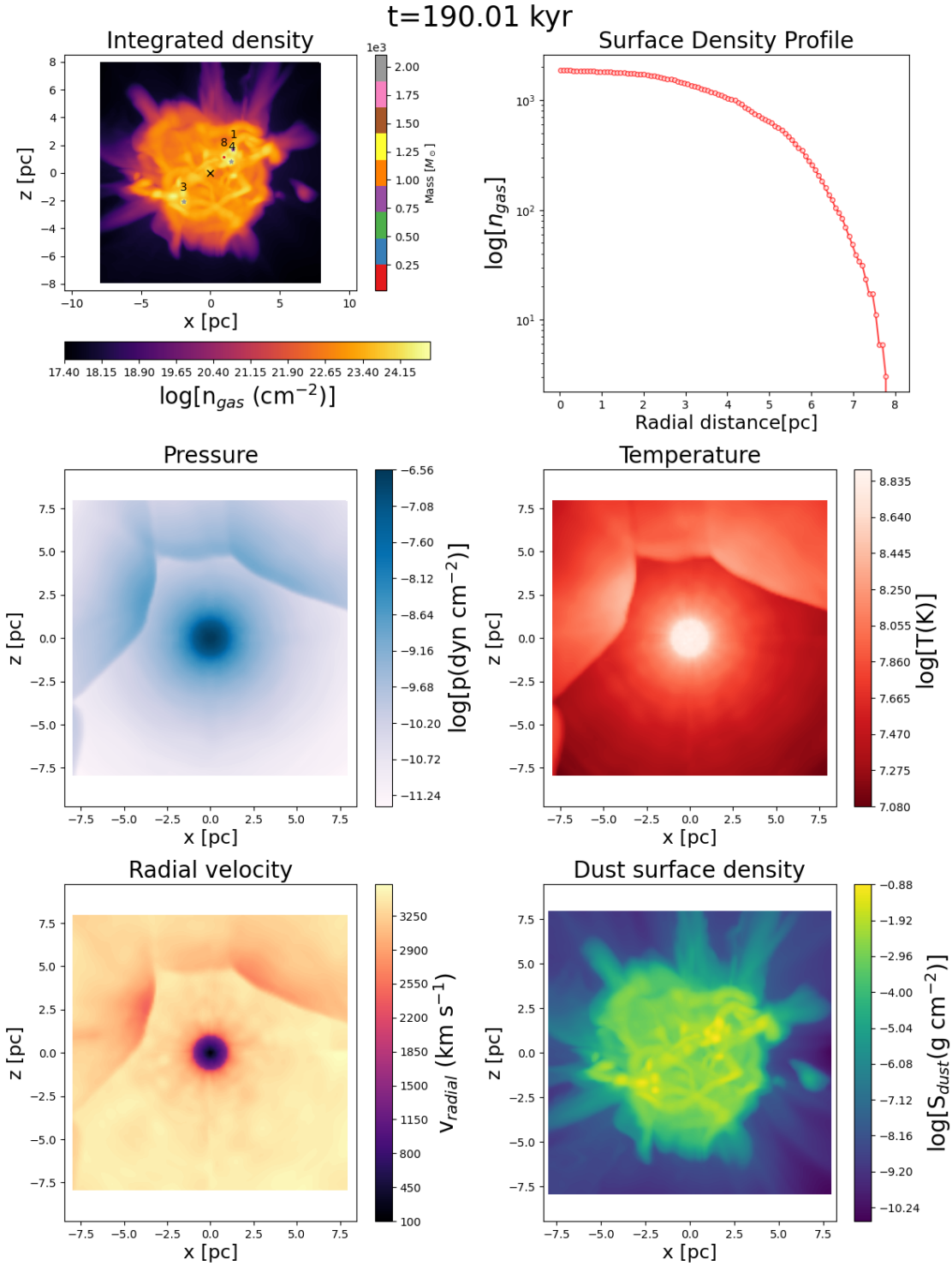


Figure 4.22: Same as Figure 4.12, but at time $t = 190$ kyr.

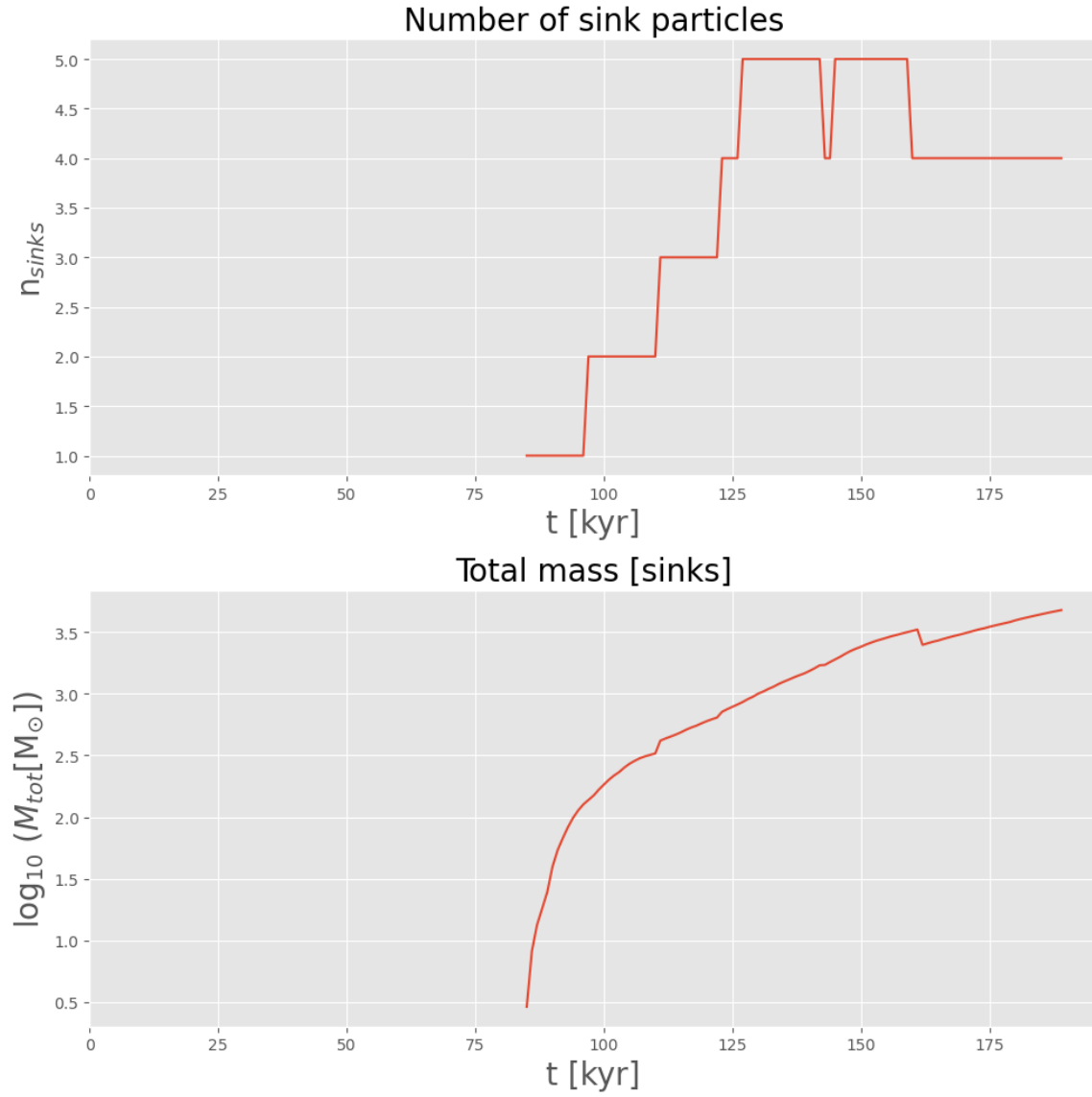


Figure 4.23: The top panel tracks the creation of sink particles over time, while the bottom panel tracks the total mass within sink particles over time.

4.3 Evolution of the Cloud-Cloud Case

The evolution in the **Cloud-Cloud Case** is here described using a similar approach to the one used in the previous section, with a focus on describing the most important aspects.

As an initial condition, we replicate the conditions as in the "clumpy-case", where a central cavity is imposed in order to prevent overcooling (see Figure 4.24). The collision of a secondary cloud with the primary cloud (at a speed $v_{coll} \sim 30 \text{ km s}^{-1}$) leads to an intricate scenario.

The SSC-B super-wind begins heating the cloud surfaces via ram pressure, inducing turbulence (most probably through Kelvin-Helmholtz instabilities) and filament formation, as seen at a time $\sim 22 \text{ kyr}$ (see Figure 4.25). The cavity encompassing the primary star cluster is now filled with hot gas from the star cluster wind, affecting significantly the dynamics of the region.

Formation of the first sink particle occurs at around $\sim 37 \text{ kyr}$ of evolution (as illustrated Figure 4.26). This time is characterized by a continuous series of collapses and the formation of compressed layers. While the super-wind's effects remain, their influence gradually weakens.

At 68 kyr (see Figure 4.27), 13 additional sink particles are formed predominantly at the collision interface. The reverse shock has formed, so the free-wind region starts to be thermalized.

Later on, at $\sim 76 \text{ kyr}$ (see Figure 4.28), the super-wind finds an escape route. Thus its very high temperature inhibits further sink particle creation, exerting negative feedback and controlling the region's dynamics.

At 90 kyr (see Figure 4.29), despite the super-winds negative feedback, high-density regions continue to produce additional sink particles within the collision zone, maintaining localized star formation.

Approximately 149 kyr into the simulation (see Figure 4.30), the super-wind fills the entire box, yet episodes star formation persist, demonstrating the paramount impact of the collision on system dynamics.

At 150 kyr, supernova explosions are introduced into the simulation in order to quantify their overall effect on further inducing or inhibiting star formation. Indeed, supernova explosions appear to inhibit the formation of additional sink particles (see the top panel of Figure 4.32). Nevertheless, the accretion of matter onto existing sink particles continues.

It is important to note that once the new stars are formed they will provide a negative feedback (via radiation and outflows) which was not taken into account in the present study. Therefore, the presented results should be interpreted as an upper limit for the total mass in secondary star cluster formation. Thus including such mechanisms will provide a better estimation of the total mass.

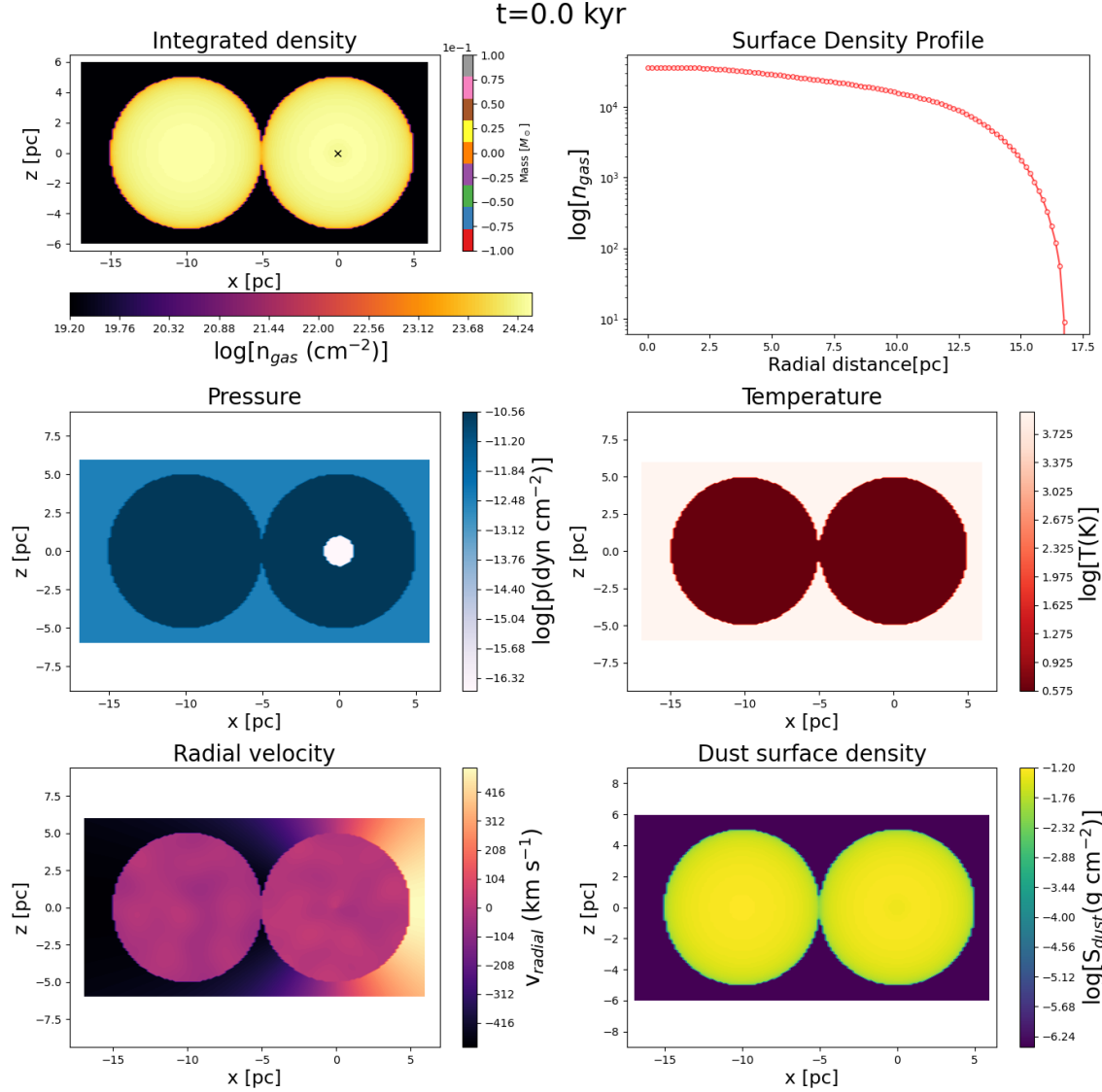


Figure 4.24: The displayed plots include the column density (top-left), surface density profile (top-right), thermal pressure (middle-left), temperature (middle-right), radial velocity (bottom-left), and dust surface density (bottom-right) at $t = 0.0$ kyr. Additionally, the center of the box, corresponding to the region of A1, is marked with a 'cross' symbol. The color of the dot symbols corresponds to the mass of the sink particle, which is indicated by the vertical colorbar.

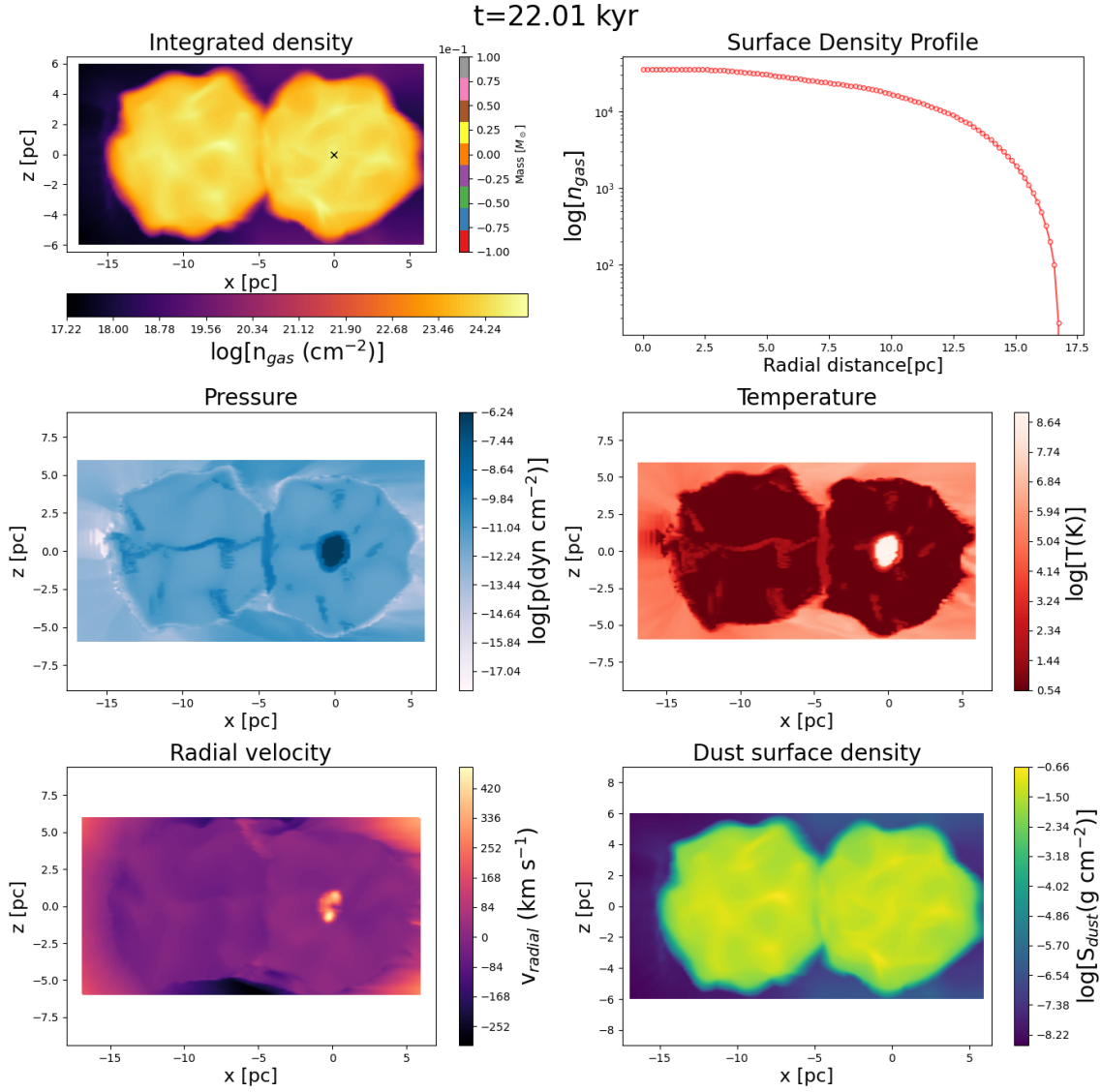


Figure 4.25: Same as in Figure 4.24, but at time $t = 22 \text{ kyr}$.

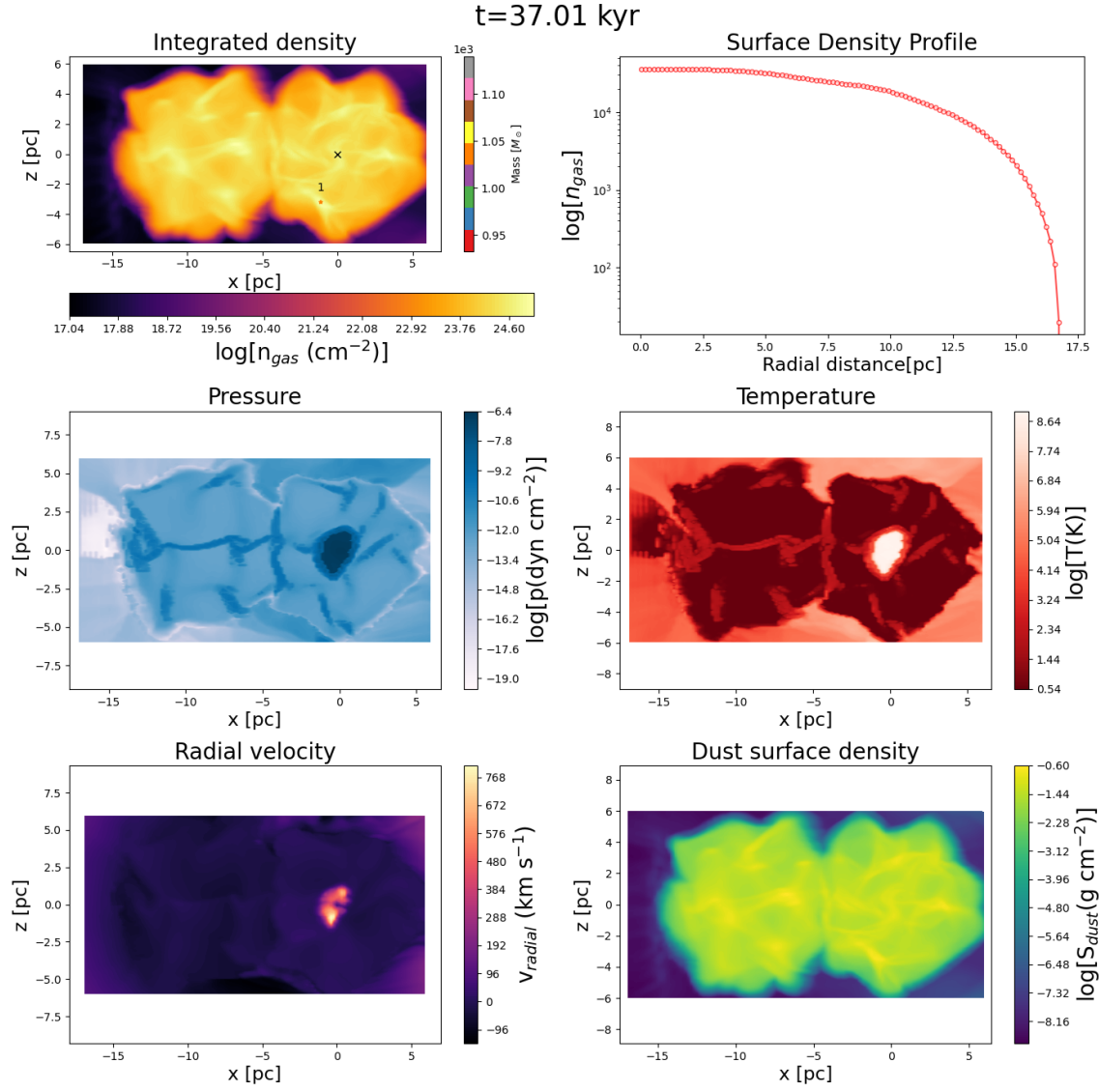


Figure 4.26: Same as in Figure 4.24, but at time $t = 37 \text{ kyr}$.

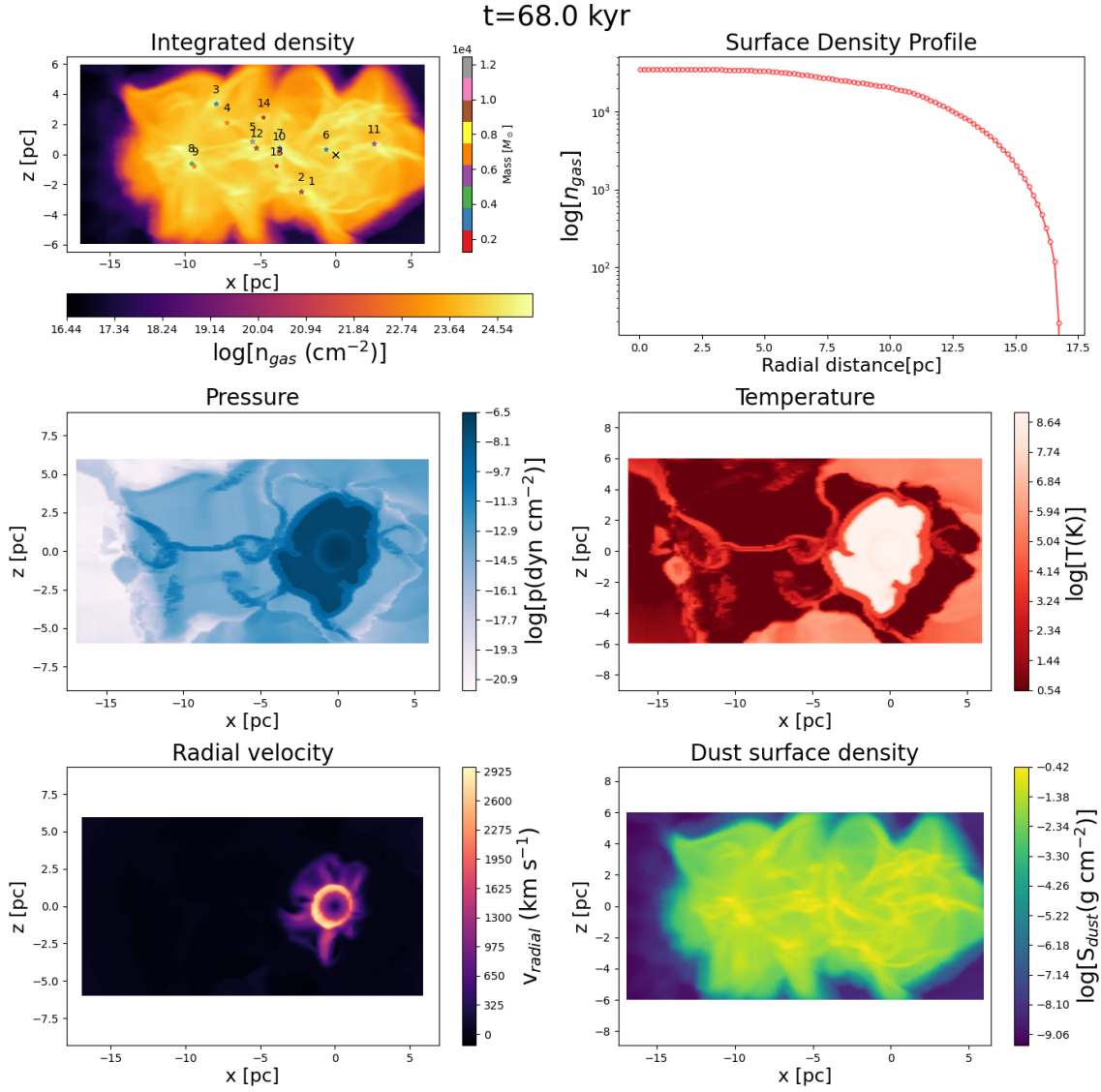


Figure 4.27: Same as in Figure 4.24, but at time $t = 68 \text{ kyr}$.

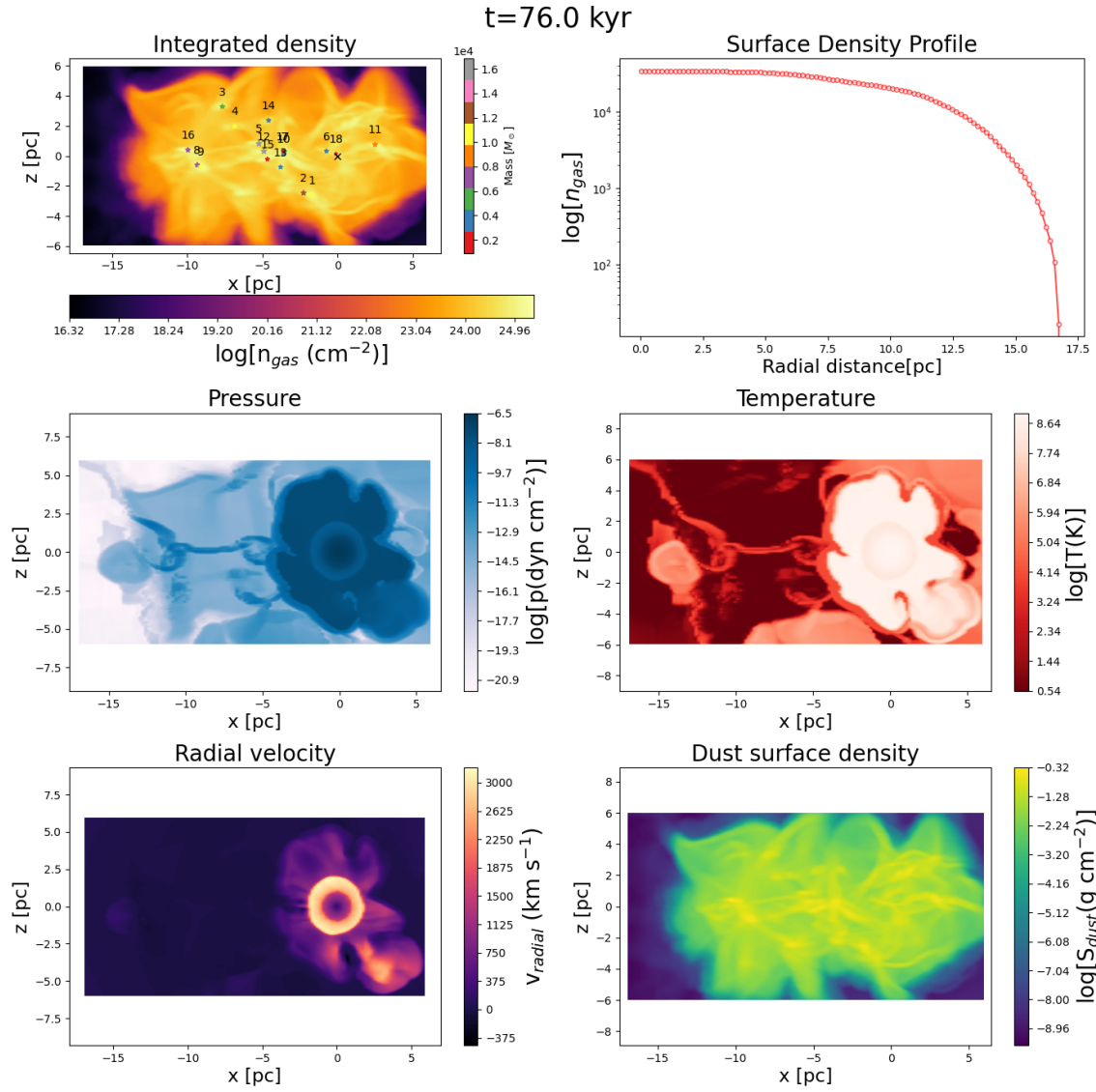
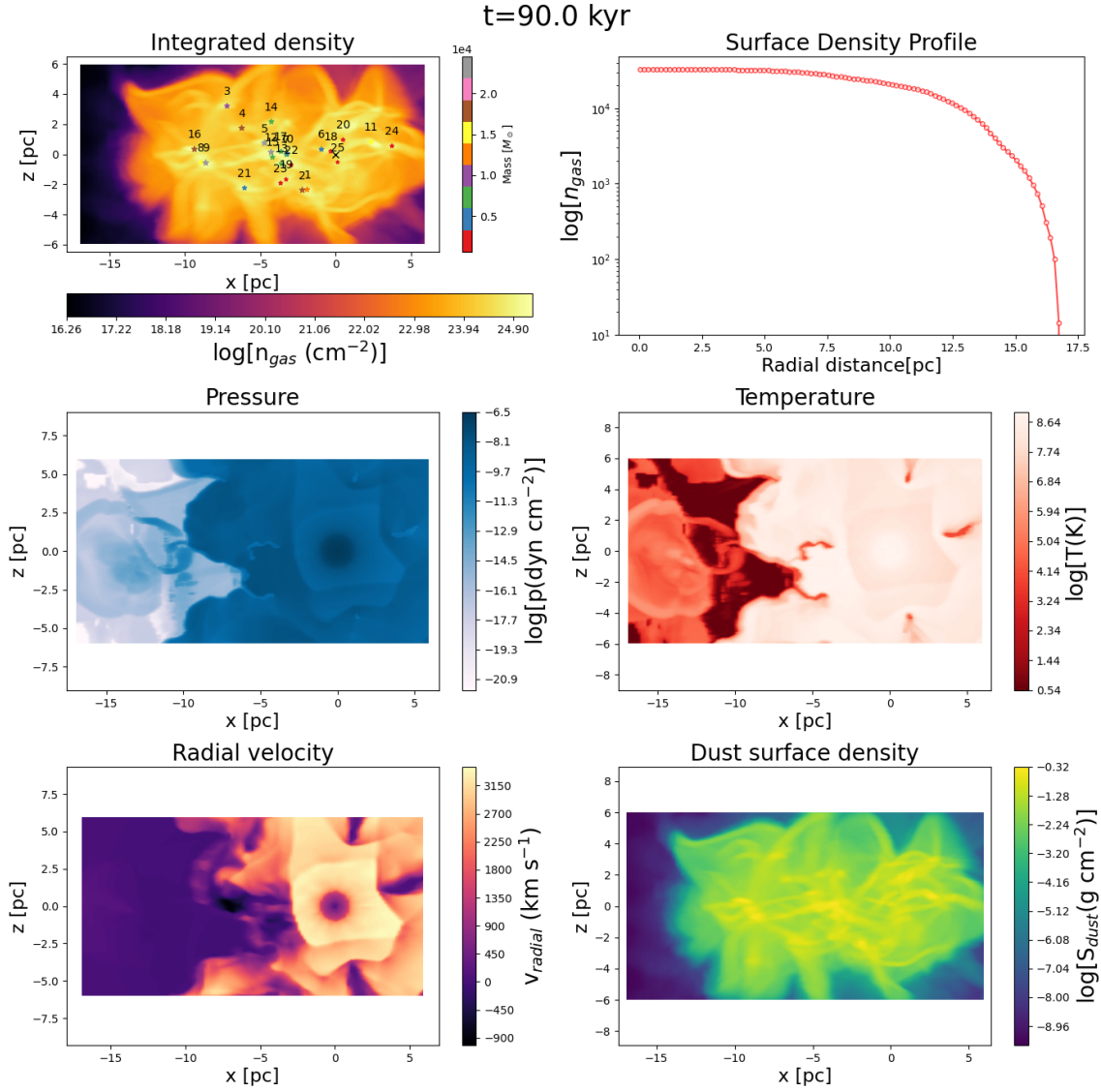


Figure 4.28: Same as in Figure 4.24, but at time $t = 76 \text{ kyr}$.

Figure 4.29: Same as in Figure 4.24, but at time $t = 91 \text{ kyr}$.

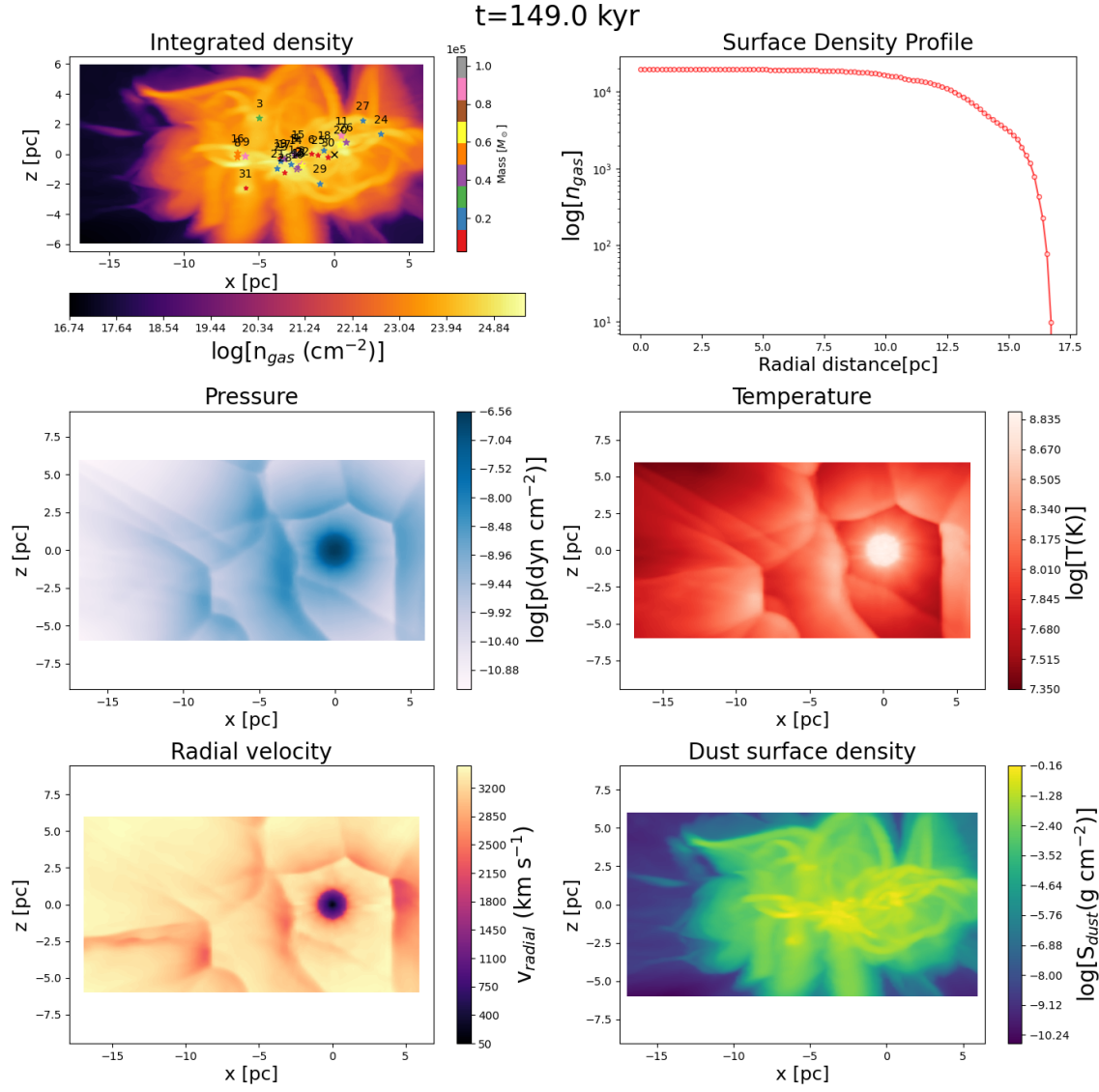
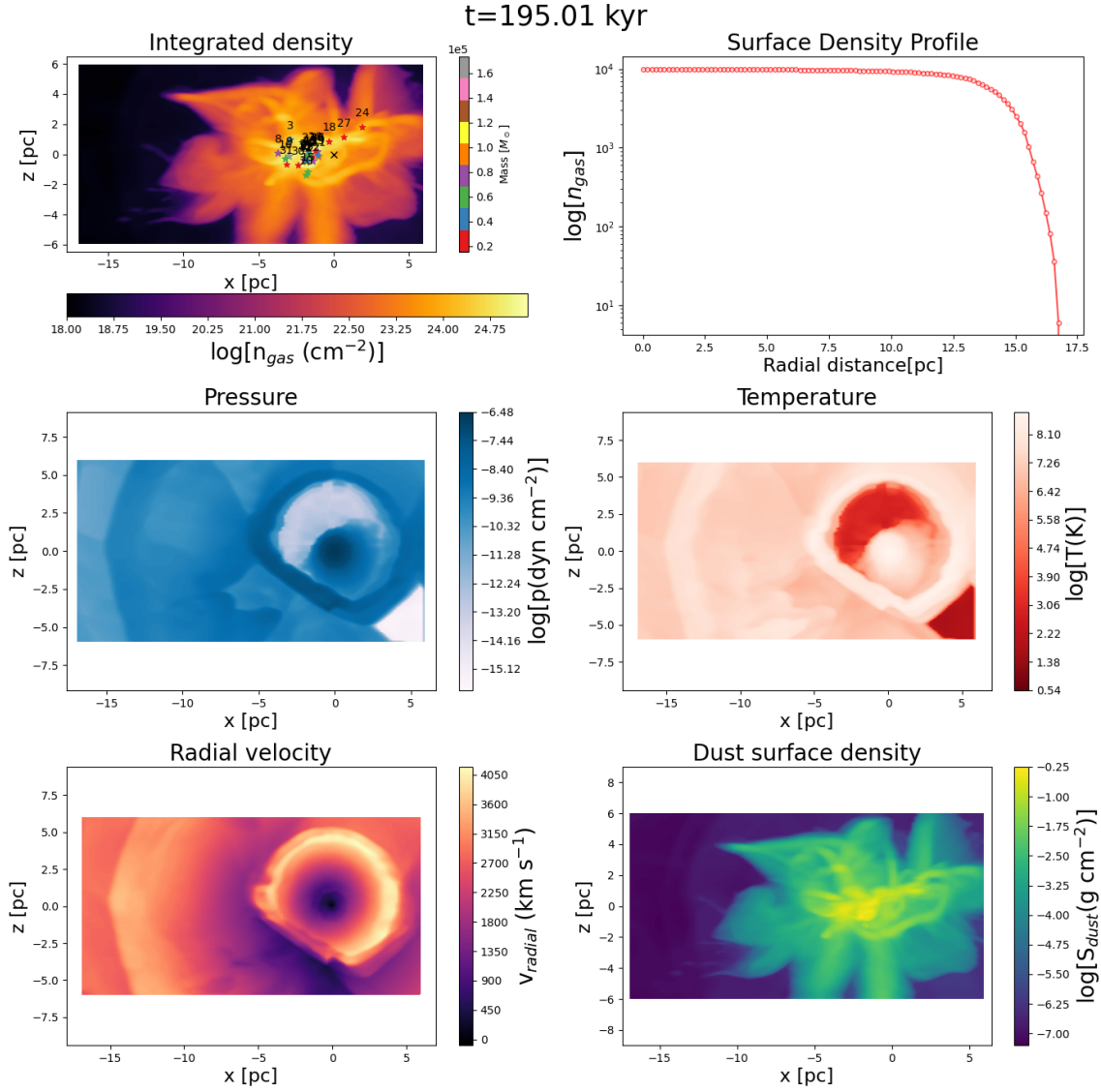


Figure 4.30: Same as in Figure 4.24, but at time $t = 150 \text{ kyr}$.

Figure 4.31: Same as in Figure 4.24, but at time $t = 196 \text{ kyr}$.

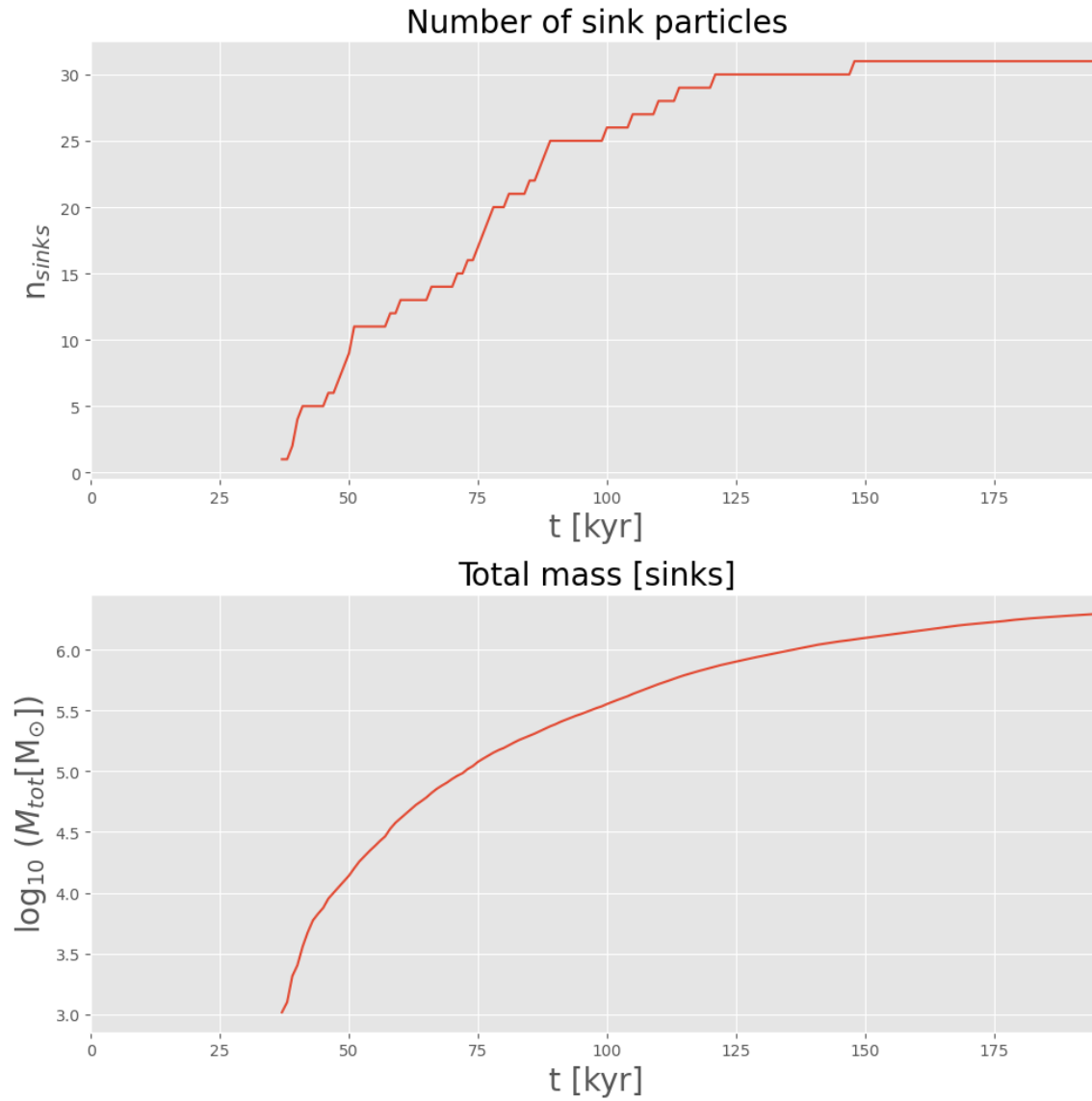


Figure 4.32: The top panel follows the creation of sink particles over time. The bottom panel shows the temporal evolution of the total mass locked up in sink particles.

Discussion and Conclusions

The dynamical ages of observed superbubbles may be significantly shorter than those of the clusters they contain (e.g. Fuller et al., 2023; Sánchez-Cruces et al., 2015), indicating that either the current star clusters are not the original source of the outflows or there exists another process depleting the gas within the superbubbles that is not accounted for in classical evolutionary models of wind bubbles. However, the work by Silich & Tenorio-Tagle (2018) and Silich et al. (2020) addresses this issue and proposes models that seem to reconcile the discrepancy in dynamical ages.

The formation of globular clusters in a high-pressure environment is believed to contribute to their compactness and high star formation efficiency, crucial for the formation of long-lived bound clusters. The compactness of the cluster is associated with the density of the central gas. In the case of massive and compact stellar clusters, the strong radiative cooling prevents the wind-driven shells around individual massive stars from merging into a global super-wind, as demonstrated by Silich & Tenorio-Tagle (2017, 2018). Instead, hot shocked winds around individual massive stars take a few millions of years to merge and form a global star cluster wind capable of expelling the residual gas.

At first glance, negative feedback from massive stars is often considered the mechanism responsible for expelling the remaining gas and terminating star formation in young clusters. However, this feedback mechanism is significantly suppressed in massive and compact star-forming regions. The efficiency of star formation, the metallicity of the star-forming cloud, and the initial mass segregation in forming clusters all play

important roles in this process.

The hot shock wind regions around massive stars continue to expand as the central stars supply mass and energy over an extended period. These hot bubbles, filled with shocked stellar wind gas, expand in a subsonic regime until they merge, after a few megayears with neighboring bubbles or reach their cooling radii.

The dominance of turbulence in the intra-cluster gas pressure in both scenarios can be attributed to the low temperature of the molecular gas, as suggested by Elmegreen et al. (1995). Turbulence is a significant factor in the model due to this characteristic.

The study of both the clumpy case and the cloud-cloud case provides valuable insights into the formation and evolution of dense filaments and subsequent stellar populations in clusters. Simulations reveal the dynamic interplay between colliding clouds, the super-wind from the central star cluster, and turbulence within the system.

In the clumpy case, the interaction of the super-wind and turbulent cloud material leads to the formation of hierarchical structures. The birth of the main cluster creates a cavity within the main cloud, while turbulence facilitates filament self-collapse and sink formation. Sequential sink creation represents important milestones, with subsequent sinks accumulating material and contributing to the overall mass of the cluster.

Similarly, in the cloud-cloud case, the collision of two clouds generates a hot compressed layer and dense gas sheet. Turbulence enhances filamentary structures and triggers cloud self-collapse. The super-wind from the central cluster expands the hot gas beyond the A1 region, extending outside the simulation box.

Throughout the evolution of both scenarios, denser regions continuously grow, and multiple sinks form via three main ways:

- Global and local collapse through a gravo-turbulent interplay (e.g. Vazquez-Semadeni, 2012)
- Compression as a result of positive mechanical feedback (collect and collapse) (e.g. Elmegreen et al., 1995).
- Formation of compressed layers after cloud-cloud collisions (e.g. Fukui et al.,

2020)

The Gravo-Turbulent scenario provides the properties on both a global and local scale. It encompasses gravitational collapse and the formation of overdensities and filament structures, respectively. The positive feedback scenario arises from the interaction of a shockwave, generating a compressed shell. As this shell rapidly cools down, it retains its density and transforms into a cold gas region, thereby inducing star formation. Lastly, the collision region emerges from the interaction between clouds, resulting in a compressed gas layer that also possesses the necessary properties for star formation.

The interplay among hot gas, turbulence, and density structures shapes the system's dynamics, yielding a complex network of filaments and sinks.

This study underscores the significance of cloud-cloud collisions in triggering high-mass stellar formation, a conclusion that aligns with the findings of Fukui et al. (2020).

Furthermore, gravitational instabilities in the cloud-cloud scenario manifest at approximately 22 kyr, in line with the predictions of Equation 4.1.3, thereby corroborating the results of this study.

In the case of SSC-A in NGC 1569, the cloud-cloud scenario demonstrates the conditions required for the emergence of a second generation of stars within 3 pc from the main cluster or the first generation of stars. This model establishes that the induction of star formation is indeed successful with the condition of separation and ages between its components.

List of Figures

- 1.1 Open cluster NGC 346 is captured in this composite image, which combines separate exposures taken by the James Webb Telescope using the NIRCам instrument. The colors in the image result from different filters: red represents the F444W filter, orange represents the F335M filter, cyan represents the F277W filter, and blue represents the F200W filter. Credit: NASA, ESA, CSA, Olivia C. Jones (UK ATC), Guido De Marchi (ESTEC), Margaret Meixner (USRA) 2

- 1.2 On the left side, we have the globular cluster M79 captured in a composite image created from various exposures using the WFPC2 instrument on the Hubble Space Telescope. The colors in the image result from different filters: blue corresponds to the F336 + F439 filters, green corresponds to the F336 + F439 + F555 filters, and red corresponds to the F555 filter. Credit: NASA and ESA. On the right side, we have the open cluster Trumpler 14, captured in a composite image made from multiple exposures using the ACS/WFC instrument on the Hubble Space Telescope. The colors in the image are the result of different filters: blue corresponds to the F435W (B) filter, green corresponds to the F550M (V) filter, red corresponds to the F658N (H_{α} + $[N\ II]$) filter, and purple corresponds to the F850LP (SDSS z) filter. Credit: NASA, ESA, and Z. Levay (STScI). 4

- 1.3 Evolution of a $60M_{\odot}$ star, panel (a) shows the mass loss rate with solar metallicity obtained by Schaller et al. (1992b) and panel (b) shows the terminal speed assuming a conversion factor between v_{∞} and v_{esc} introduced by Vink et al. (2001). Adapted from Martínez-González et al. (2019b). 8
- 1.4 The galaxy NGC 1569 is captured in a composite image created from multiple exposures using the ACS and WFPC2 instruments on the Hubble Space Telescope. The image is produced using different filters: red corresponds to the F658N filter, which captures the $H_{\alpha} + [\text{N II}]$ emission; green/cyan corresponds to the F606W filter, representing the wide V band; cyan corresponds to the F502N filter, capturing the $[\text{O III}]$ emission; and blue corresponds to the F487 filter, capturing the H_{β} emission. In the image, we can observe the core of NGC 1569, which contains three giant star clusters. These clusters are situated within a central cavity that has been shaped by the feedback from massive young stars, resulting in distinct gaseous structures. Credits for the image go to NASA, ESA, and Z. Levay (STScI) for the illustration, and to NASA, ESA, the Hubble Heritage Team (STScI/AURA), and A. Aloisi (STScI/ESA) for the scientific data 13
- 1.5 NGC 1569 (HST), both circles correspond to the super star clusters A and B (left). Close up for the SSC-A (right). Adapted from Hernández Prado (2022). 14
- 1.6 Velocity map in $H\alpha$ showing the superbubbles from the work of Sánchez-Cruces et al. (2015). 15
- 1.7 Observations from HST data show the structures that comprise SSC-A (left). A comparison is made between the HST observation and the simulation, with the upper and bottom panels representing each, respectively (middle). The surface brightness profile from the HST data and the simulation is also shown, with blue and red lines plotted, respectively (right). Adapted from Hernández Prado (2022). 18

2.1	Evolution of density of self-gravitational models. The numbers in the top left corresponds to the time in Myr. Sink particles are plotted with circles (Dinnbier et al., 2017).	25
2.2	Basic structure of a stellar wind interacting with the ISM, consisting in several regions including an emitting star or in the case of a star cluster, the collective wind of all their stars, the interaction region and finally the undisturbed ISM.	28
2.3	Integral curves depict different scenarios based on the central temperature of the wind. When the central temperature exceeds the stationary case, the integral curve extends to the sonic point located inside the cluster at R_D , where the velocity becomes supersonic, this solution, known as the "unphysical double value solution". On the other hand, if the central temperature is lower than the stationary case, the integral curve reaches its maximum velocity at R_N , after which the velocity gradually decreases. In this case, the wind remains subsonic throughout, this solution is referred to as the "breeze solution." The unique wind solution corresponds to the scenario where the integral curve passes through the sonic point at R_{sc} and the flow becomes supersonic for larger radii. This figure is adapted from Silich et al. (2011).	32
2.4	The velocity distribution (panel a), pressure distribution (panel b), density distribution (panel c), and temperature distribution (panel d) of the shocked wind zone around individual stars located at the center of a star-forming cloud are depicted. In the figure, dashed, solid, and dotted lines represent the distributions of these variables in clouds with different core radii: 2 pc, 3 pc, and 4 pc, respectively. Additionally, vertical dashed, solid, and dotted lines indicate the average half distance between neighboring massive stars in each respective case. The figure has been adopted from Silich & Tenorio-Tagle (2018).	42

2.5	The temperature distribution is shown in the top and bottom panels for two neighboring wind-driven bubbles located within a cloud. The cloud has a total mass of $M_t = 7.14 \times 10^5 M_\odot$, an efficiency parameter of $\varepsilon = 0.1$, a core radius of $r_c = 0.87$ pc, and a metallicity of $Z = 10^{-2} Z_\odot$. In the top panel, the neighboring bubbles are located at the center of the cloud, while in the bottom panel, they are positioned at a distance of $r = 2.2$ pc. The x-axis represents the distance between the stars, denoted as S1 and S2. The dashed lines indicate the positions of the reverse shocks for each star, and the vertical solid lines represent the half distance between the stars. The shaded regions illustrate the shocked wind zones. Adapted from Jiménez Villarraga (2022)	44
2.6	Cooling radius (solid line) and the half distance X (dotted line) as a function of the position within the gas cloud R for the same case as Figure 2.5, the vertical solid line shows where $R_{\text{cool}}/X = 1$. Adapted from Jiménez Villarraga (2022)	45
2.7	The cooling radius, denoted as R_{cool} , is normalized to a half-distance X between neighboring massive stars in the center of the star cluster. In the plot, the dashed and solid lines correspond to models with mass loss rates of $\dot{M}_{PMS} = 8 \times 10^{-9} M_\odot \text{ yr}$ and $\dot{M}_{PMS} = 5 \times 10^{-8} M_\odot \text{ yr}$, respectively. Figure adapted from Silich et al. (2020)	46
2.8	The hot gas filling factor f_X in the central zone of the cluster as a function of time. Figure adapted from Silich et al. (2020)	47
4.1	NGC 1569-A. The marked zones correspond to the A1 and A2 clusters, with the first in the center and the second in the outer region. Figure adopted from Hernández Prado (2022).	58
4.2	Column density, temperature and radial velocity panels are shown at $t = 0.0$ kyr for the "two-cloud" model.	60
4.3	Column density, temperature and radial velocity panels are shown at $t = 26$ kyr for the "two-cloud" model.	60
4.4	Column density, temperature and radial velocity panels are shown at $t = 60$ kyr for the "two-cloud" model.	61

4.5	Column density, temperature and radial velocity panels are shown at $t = 130$ kyr for the "two-cloud" model.	61
4.6	Contrast sequence from HST data, figure adapted from Hernández Prado (2022).	62
4.7	The density (top-left panel), temperature (top-right panel), radius (bottom-left panel), and mass (bottom-right panel) plots are presented for the clumpy case. Each cloud is shown in its respective location in the x-y plane with $z = 0$, along with its corresponding parameter values. The two star symbols indicate the location of A1 and A2 in each panel.	64
4.8	Histogram of the distribution of mass for each cloud in the clumpy case.	65
4.9	Density slice of two clouds after 5.31 Myr, for static simulations. The left panel shows the clouds with no initial turbulence while the right panel shows the outcome of adding an initial turbulent spectrum to both clouds. Figure adapted from Takahira et al. (2014)	65
4.10	Top panel: schematic picture of three evolutionary epochs of the Habe-Ohta model of a cloud-cloud collision between two spherical clouds with different sizes. As the small cloud drives into the larger, a U-shaped cavity is created in the large cloud and the small streams into the compressed layer formed in the collision interface. Bottom panel: Surface density plots of a 10 km s^{-1} collision. Figure adapted from Fukui et al. (2020).	66
4.11	The density (top-left panel), temperature (top-right panel), radius (bottom-left panel), and mass (bottom-right panel) plots are presented for the cloud-cloud case. Each cloud is shown in its respective location in the x-y plane with $z = 0$, along with its corresponding parameter values. The two star symbols indicate the location of A1 and A2 in each panel.	69
4.12	The plots display the column density (top-left), surface density profile (top-right), pressure (middle-left), temperature (middle-right), radial velocity (bottom-left), and dust surface density (bottom-right) at $t = 0$ kyr. Additionally, the center of the box, corresponding to the region of A1, is marked with a 'cross' symbol. The color of the dot symbols corresponds to the mass of the sink particle, which is indicated by the vertical qualitative colorbar.	72

4.13	Same as Figure 4.12, but at time $t = 1$ kyr.	73
4.14	Same as Figure 4.12, but at time $t = 22$ kyr.	74
4.15	Same as Figure 4.12, but at time $t = 53$ kyr.	75
4.16	Same as Figure 4.12, but at time $t = 61$ kyr.	76
4.17	Same as Figure 4.12, but at time $t = 71$ kyr.	77
4.18	Same as Figure 4.12, but at time $t = 85$ kyr.	78
4.19	Same as Figure 4.12, but at time $t = 97$ kyr.	79
4.20	Same as Figure 4.12, but at time $t = 111$ kyr.	80
4.21	Same as Figure 4.12, but at time $t = 155$ kyr.	81
4.22	Same as Figure 4.12, but at time $t = 190$ kyr.	82
4.23	The top panel tracks the creation of sink particles over time, while the bottom panel tracks the total mass within sink particles over time. . .	83
4.24	The displayed plots include the column density (top-left), surface density profile (top-right), thermal pressure (middle-left), temperature (middle-right), radial velocity (bottom-left), and dust surface density (bottom-right) at $t = 0.0$ kyr. Additionally, the center of the box, corresponding to the region of A1, is marked with a 'cross' symbol. The color of the dot symbols corresponds to the mass of the sink particle, which is indicated by the vertical colorbar.	86
4.25	Same as in Figure 4.24, but at time $t = 22$ kyr.	87
4.26	Same as in Figure 4.24, but at time $t = 37$ kyr.	88
4.27	Same as in Figure 4.24, but at time $t = 68$ kyr.	89
4.28	Same as in Figure 4.24, but at time $t = 76$ kyr.	90
4.29	Same as in Figure 4.24, but at time $t = 91$ kyr.	91
4.30	Same as in Figure 4.24, but at time $t = 150$ kyr.	92
4.31	Same as in Figure 4.24, but at time $t = 196$ kyr.	93
4.32	The top panel follows the creation of sink particles over time. The bottom panel shows the temporal evolution of the total mass locked up in sink particles.	94

List of Tables

1.1	Properties of the Super Star Cluster A in NGC 1569.	17
1.2	Structural parameters for a simulation of the composition of SSC-A using nProfit (Hernández Prado, 2022).	17
4.1	Initial Cloud Parameters for the "two-clouds" case.	59
4.2	Simulation parameters for the "two-clouds" case.	59
4.3	Initial Cloud Parameters for the clumpy case.	62
4.4	Initial Cloud Parameters for the cloud-cloud case.	68
4.5	Simulation parameters for the cloud-cloud case.	68

References

- Anders P., de Grijs R., Fritze-v. Alvensleben U., Bissantz N., 2004, Monthly Notices of the Royal Astronomical Society, 347, 17
- Bally J., 2008, Overview of the Orion Complex ([arXiv:0812.0046](#))
- Bastian N., Lardo C., 2018, Annual Review of Astronomy and Astrophysics, 56, 83
- Chevalier R. A., Clegg A. W., 1985, Nature, 317, 44
- Cuevas-Otahola B., Mayya Y. D., Puerari I., Rosa-González D., 2022, Publications of the Astronomical Society of the Pacific, 134, 024502
- De Marchi G., Clampin M., Greggio L., Leitherer C., Nota A., Tosi M., 1997, ApJ, 479, L27
- Dinnbier F., Wünsch R., Whitworth A. P., Palouš J., 2017, MNRAS, 466, 4423
- Draine B. T., 2011, Physics of the Interstellar and Intergalactic Medium
- Elmegreen B. G., Kimura T., Tosa M., 1995, ApJ, 451, 675
- Elson R. A. W., Fall S. M., Freeman K. C., 1987, ApJ, 323, 54
- Federrath C., Banerjee R., Clark P. C., Klessen R. S., 2010, ApJ, 713, 269
- Franeck A., Wünsch R., Martínez-González S., Orlitová I., Boorman P., Svoboda J., Szécsi D., Douna V., 2021, ApJ, submitted
- Fryxell B., et al., 2000, ApJS, 131, 273

- Fukui Y., Habe A., Inoue T., Enokiya R., Tachihara K., 2020, Publications of the Astronomical Society of Japan, 73, S1
- Fuller C. A., Kaaret P., Bluem J., Kuntz K. D., Hodges-Kluck E., Jahoda K. M., 2023, ApJ, 943, 61
- Galli, P. A. B. et al., 2019, A&A, 630, A137
- González Delgado R. M., Leitherer C., Heckman T., Cerviño M., 1997, ApJ, 483, 705
- Gratton R., Bragaglia A., Carretta E., D’Orazi V., Lucatello S., Sollima A., 2019, The Astronomy and Astrophysics Review, 27
- Grocholski A. J., van der Marel R. P., Aloisi A., Annibali F., Greggio L., Tosi M., 2012, The Astronomical Journal, 143, 117
- Habe A., Ohta K., 1992, , 44, 203
- Harris W. E., 1996, AJ, 112, 1487
- Heckman T. M., Dahlem M., Lehnert M. D., Fabbiano G., Gilmore D., Waller W. H., 1995, ApJ, 448, 98
- Hernández Prado J. O., 2022, Estudio fotométrico del súper cúmulo estelar A de la galaxia NGC 1569., doi:10.5281/zenodo.8076333, <https://doi.org/10.5281/zenodo.8076333>
- Hunter D. A., O’Connell R. W., Gallagher J. S., Smecker-Hane T. A., 2000, The Astronomical Journal, 120, 2383–2401
- Jedrzejewski R. I., 1987, Monthly Notices of the Royal Astronomical Society, 226, 747
- Jiménez S., Tenorio-Tagle G., Silich S., 2021, MNRAS, 505, 4669
- Jiménez Villarraga S., 2022, PhD thesis, Instituto Nacional de Astrofísica, Óptica y Electrónica
- Kharchenko N. V., Piskunov A. E., Röser S., Schilbach E., Scholz R. D., 2005, A&A, 438, 1163

- Kroupa P., 2001, *MNRAS*, 322, 231
- Lamers H. J. G. L. M., Cassinelli J. P., 1999, *Introduction to Stellar Winds*. Cambridge University Press, doi:10.1017/CBO9781139175012
- Landau L. D., Lifshitz E. M., 1987, *Fluid Mechanics*
- Markova N., Puls J., 2008, *A&A*, 478, 823
- Markova N., Puls J., Repolust T., Markov H., 2004, *A&A*, 413, 693
- Martínez-González S., Tenorio-Tagle G., Silich S., 2016, *ApJ*, 816, 39
- Martínez-González S., Wünsch R., Palouš J., 2017, *ApJ*, 843, 95
- Martínez-González S., Wünsch R., Palouš J., Muñoz-Tuñón C., Silich S., Tenorio-Tagle G., 2018, *ApJ*, 866, 40
- Martínez-González S., Wünsch R., Silich S., Tenorio-Tagle G., Palouš J., Ferrara A., 2019a, *ApJ*, 887, 198
- Martínez-González S., Wünsch R., Silich S., Tenorio-Tagle G., Palouš J., Ferrara A., 2019b, *ApJ*, 887, 198
- Martínez-González S., Wünsch R., Tenorio-Tagle G., Silich S., Szécsi D., Palouš J., 2022, *ApJ*, 934, 51
- Mayya Y. D., Romano R., Rodríguez-Merino L. H., Luna A., Carrasco L., Rosa-González D., 2008, *ApJ*, 679, 404
- Mayya Y. D., et al., 2020, *Monthly Notices of the Royal Astronomical Society*, 498, 1496–1514
- Melo V. P., Muñoz-Tuñón C., Maíz-Apellániz J., Tenorio-Tagle G., 2005, *ApJ*, 619, 270
- Mengel S., Lehnert M. D., Thatte N., Genzel R., 2002, *A&A*, 383, 137
- Milone A. P., Marino A. F., 2022, *Universe*, 8
- Ninkovic S., 1998, *Serbian Astronomical Journal*, 158, 15

- Origlia L., Leitherer C., Aloisi A., Greggio L., Tosi M., 2001, *The Astronomical Journal*, 122, 815–824
- Palouš J., Wunsch R., Martínez-González S., Hueyotl-Zahuantitla F., Silich S., Tenorio-Tagle G., 2013, *ApJ*, 772, 128
- Parker E. N., 1958, *ApJ*, 128, 664
- Parker E. N., 1960, *ApJ*, 132, 821
- Plummer H. C., 1911, *MNRAS*, 71, 460
- Portegies Zwart S. F., McMillan S. L., Gieles M., 2010, *Annual Review of Astronomy and Astrophysics*, 48, 431
- Prantzos, N. Charbonnel, C. 2006, *A&A*, 458, 135
- Rodríguez-González A., Cantó J., Esquivel A., Raga A. C., Velázquez P. F., 2007, *Monthly Notices of the Royal Astronomical Society*, 380, 1198
- Sánchez-Cruces M., Rosado M., Rodríguez-González A., Reyes-Iturbide J., 2015, *ApJ*, 799, 231
- Sarazin C. L., White Raymond E. I., 1987, *ApJ*, 320, 32
- Schaller G., Schaerer D., Meynet G., Maeder A., 1992a, , 96, 269
- Schaller G., Schaerer D., Meynet G., Maeder A., 1992b, , 96, 269
- Schure K. M., Kosenko D., Kaastra J. S., Keppens R., Vink J., 2009, *A&A*, 508, 751
- Silich S., Tenorio-Tagle G., 2017, *MNRAS*, 465, 1375
- Silich S., Tenorio-Tagle G., 2018, *MNRAS*, 478, 5112
- Silich S., Tenorio-Tagle G., Rodríguez-González A., 2004, *ApJ*, 610, 226
- Silich S., Bisnovatyi-Kogan G., Tenorio-Tagle G., Martínez-González S., 2011, *ApJ*, 743, 120
- Silich S., Tenorio-Tagle G., Martínez-González S., Turner J., 2020, *MNRAS*, 494, 97

- Szécsi D., Langer N., Yoon S.-C., Sanyal D., de Mink S., Evans C. J., Dermine T., 2015, *A&A*, 581, A15
- Szécsi D., Wünsch R., Agrawal P., Langer N., 2020, arXiv e-prints, p. arXiv:2004.08203
- Takahira K., Tasker E. J., Habe A., 2014, *ApJ*, 792, 63
- Tang X., Chevalier R. A., 2017, *MNRAS*, 465, 3793
- Tenorio-Tagle G., Bodenheimer P., 1988, *ARA&A*, 26, 145
- Vazquez-Semadeni E., 2012, Physical Processes of Interstellar Turbulence (arXiv:1202.4498)
- Vink J. S., de Koter A., Lamers H. J. G. L. M., 2001, *A&A*, 369, 574
- Weaver R., McCray R., Castor J., Shapiro P., Moore R., 1977, *ApJ*, 218, 377
- Whitworth A. P., Bhattal A. S., Chapman S. J., Disney M. J., Turner J. A., 1994, *A&A*, 290, 421
- Wolf C. J. E., Rayet G., 1867, *Academie des Sciences Paris Comptes Rendus*, 65, 292
- Wünsch R., Tenorio-Tagle G., Palouš J., Silich S., 2008a, *ApJ*, 683, 683
- Wünsch R., Tenorio-Tagle G., Palouš J., Silich S., 2008b, *ApJ*, 683, 683
- Wünsch R., Palouš J., Tenorio-Tagle G., Ehlerová S., 2017, *ApJ*, 835, 60
- Wünsch R., Walch S., Dinnbier F., Whitworth A., 2018, *MNRAS*, 475, 3393
- de Mink S. E., Pols O. R., Langer N., Izzard R. G., 2009, *A&A*, 507, L1
- Álvarez Cruz L. I., 2022, Edades y cinemática estelar de súper cúmulos estelares en NGC 1569